

IMAGE RECONSTRUCTION FROM MULTIPLE FRAMES OF SPARSE DATA

A thesis submitted
for the award of the Degree of
DOCTOR OF PHILOSOPHY
in
COMPUTER SCIENCE AND ENGINEERING
by
R. RAMASESHAN



Department of Computer Science and Engineering
Indian Institute of Technology
Madras - 600 036

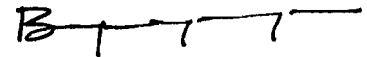
April 1994

CERTIFICATE

This is to certify that the thesis entitled ***IMAGE RECONSTRUCTION FROM MULTIPLE FRAMES OF SPARSE DATA*** submitted by *R.Ramaseshan* to the Indian Institute of Technology, Madras for the award of the degree of Doctor of Philosophy is a bonafide record of research work carried out by him under my supervision. The contents of this thesis have not been submitted and will not be submitted to any other Institute or University for the award of any degree or diploma.

Madras 600 036

Date: *April 29, 1994*


Research Guide

ACKNOWLEDGEMENTS

I consider myself very fortunate to have spent a few years among a vibrant group of researchers at the Speech and Vision laboratory.

My deepest thanks go to **Prof. B.Yegnanarayana**, my guide. He has played a vital role in my professional growth. I thank him for introducing me to the field of computer vision, and nurturing my understanding through stimulating discussions and constructive criticism. His meticulous review of the earlier drafts of this thesis has helped me refine my ideas and presentation. I thank him for providing me with excellent facilities for carrying out the work.

I thank **Prof. Kamala Kirthivasan**, the Head of the Department, for her advice, encouragement and help throughout the course of my studies.

Special thanks are owed to **Ravi** and **Arul** for their friendship and wide-ranging animated discussions. **Raghu** has proof read the earlier draft with great care. I would like to express my special thanks to him. **Sudha** helped me in several ways during the final stages of thesis writing. I gratefully acknowledge her help.

I would like to thank **Mr.R.Sundar**, **Dr.Hema A. Murthy**, **Mr.G.V.Ramana Rao**, **Mr.C.Chandrasekhar** and **Mr.N.Alwar** who have helped me in several ways. I would like to thank the members of the Speech and Vision lab, especially **Rajendran**, **Narendra Nath** and **Murthy** for their help and cooperation.

I would like to thank my friends, especially Walker and Sundar, whose help, though indirect, has been phenomenal. I have enjoyed the company of **Prabha** with whom I used to have long walks and interesting discussions.

Finally I thank my parents, Raju, Natarajan and Bhuvani, for their love, understanding, and constant support.

I thank the Department of Electronics (DoE) for partially supporting this research activity.

Table of Contents

ACKNOWLEDGEMENTS.....	ii
LIST OF FIGURES AND TABLES.....	viii
MAJOR CONTRIBUTIONS OF THE THESIS.....	xii
ABBREVIATIONS AND NOTATIONS	xiii
ABSTRACT	xv
1 INTRODUCTION.....	1
1.1 Objective of the thesis	1
1.2 Sensor array imaging.....	1
1.3 Solutions to sparse data problem.....	5
1.4 Additional knowledge about the object.....	6
1.5 Types of images	7
1.6 Quality of reconstruction.....	8
1.7 Sensor array imaging and image processing.....	10
1.8 Organization of the thesis.....	10
2 IMAGE RECONSTRUCTION METHODS.....	12
2.1 Methods of solutions from a single frame of data	12
2.2 Solutions from multiple frames of data	15
2.3 Artificial neural networks for ill-posed problems	18
3 IMAGE RECONSTRUCTION FROM SINGLE FRAME DATA	22
3.1 Tikhonov-Miller regularization.....	23
3.1.1 Formulation of the algorithm	26
3.1.2 The method of POCS	28
3.2 Convergence of the iterative regularized algorithm	33
3.3 Image reconstruction from sparse data.....	35
3.3.1 Inverse filtering.....	36
3.3.2 Image reconstruction using the method of POCS	36

3.3.3	Image reconstruction using the method of Tikhonuu-Miller regularization.....	40
3.3.4	Image reconstruction using the method of TKM-POCS	45
3.4	Image reconstruction from noisy sparse data	49
3.5	Quality of image reconstruction.....	51
3.6	Summary	52.

IMAGE RECONSTRUCTION FROM MULTIPLE FRAMES OF DATA . STATIC SITUATION.....

		5 4
4.1	Need for additional information.....	54
4.2	Sources of multiple frames of data.....	55
4.3	Multiple frame image formation model.....	56
4.4	An iterative method for image reconstruction from multiple frames of sparse data.....	58
4.5	Image reconstruction from multiple frames of data using TKM-POCS method.....	62
4.6	Sparse data collection by varying system model parameters(z and λ)	62
4.7	Experimental Studies.....	65
4.8	Results and discussions	66

5 AN ARTIFICIAL NEURAL NETWORK MODEL FOR IMAGE

	RECONSTRUCTION	73
5.1	Why ANNs for image reconstruction?.....	73
5.2	The proposed neural network model.....	75
5.3	Stability of the proposed neural network model	76
5.4	Noise suppression	78
5.5	An algorithm for image reconstruction from a single frame of sparse data.....	78
5.6	Image reconstruction using sparse and noisy data - Simulation results	81

5.7	Quality measure based on singular value decomposition	86
5.8	Algorithm for image reconstruction from multiframe data	89
5.8.1	Stability of the cascaded ANN model	91
5.8.2	Operation of the cascaded ANN model	91
5.8.3	Simulation results	95
5.9	Summary	96

6 IMAGE RECONSTRUCTION IN A DYNAMIC SCENE

SITUATION	97
6.1	Dynamic scene analysis.....9 7
6.2	Image reconstruction - known motion parameters..... 100
6.3	Image reconstruction with unknown but restricted motion parameters..... 103
6.4	image reconstruction for a general dynamic scene situation 104

7 SUMMARY AND CONCLUSIONS..... 107

7.1	Image reconstruction from single frame of data..... 107
7.2	Image reconstruction from multiple frames of data - static situation..... 109
7.3	Image reconstruction from multiple frames of data dynamic scene situation..... 109

A APPENDIX 111

A.1	Lexicographic ordering 111
A.2	Block-Toeplitz and block-circulant matrices..... 111

REFERENCES.....114

LIST OF PUBLICATIONS.....121

LIST OF FIGURES

Fig 1	A typical SAI setup.	2
Fig.1.2.	Four different types of binary images.	7
Fig.1.3.	Images of some olympic game symbols.	9
Fig.3.1.	A geometrical illustration of the unrelaxed and relaxed projection operation.	31
Fig.3.2.	Image reconstruction using inverse filtering.	37
Fig.3.3.	Illustration of the use of various constraints in the reconstruction process.	39
Fig.3.4.	Selection of optimum regularization parameter ρ	42
Fig.3.5.	Influence of regularization parameter on the quality of the reconstructed images.	44
Fig.3.6.	Image reconstruction using the method of TKM regularization.	44
Fig.3.7.	Image reconstruction using the method of TKM-POCS.	47
Fig.3.8.	The regularization error versus the iteration number for various sparsity ratios.	47
Fig.3.9.	Illustration of smooth reconstruction in 1-D. ^v	48
Fig.3.10.	Comparison of performance of three methods of image reconstruction from sparse data.	48
Fig.3.11.	Illustration of the error in the reconstructed image due to regularization.	49
Fig.3.12.	Image reconstruction from sparse and noisy data.	50

Fig.4.1.	Illustration of the movement of the receiver array along the axis	59
Fig.4.2.	Image reconstruction from multiple frames of sparse data using the method of POCS (multifrequency approach).	67
Fig.4.3.	Image reconstruction from multiple frames of data using the method of POCS (multiple distance approach).	68
Fig.4.4.	Image reconstruction from multiple frames of sparse data using the method of TKM-POCS (multiple distance approach).	69
Fig.4.5.	Image reconstruction from multiple frames of sparse data using the method of POCS (multiple distance and multifrequency approach).	71
Fig.4.6	Image reconstruction from multiple frames of sparse and noisy data using the method of TKM-POCS.	72
Fig.5.1.	A sigmoidal function.	74
Fig.5.2.	Block diagram of the proposed ANN model for image reconstruction from single frame of sparse data.	77
Fig.5.3.	Image reconstruction using five different methods (car image).	82
Fig.5.4.	Image reconstruction using sparse and noisy data ($\kappa = 16$, SNR = 0dB)	82
Fig.5.5.	Image reconstruction using sparse and noisy data. ($\kappa = 16$, SNR = -10dB)	83
Fig.5.6.	Illustration of the image reconstruction accuracy of the proposed model.	84
Fig.5.7.	Image reconstruction using five different methods (cycle image).	85
Fig.5.8	Comparison of performance of four methods of image reconstruction using SVD for the car image	87
Fig.5.9	Comparison of performance of four methods of image reconstruction using SVD for the cycle image.	89

LIST OF TABLES

Table 3.1 Optimum regularization parameter values for various sparsity ratios	43
Table 3.2 Classification accuracy of ANN	51
Table 6.1 Shift values used in the reconstruction algorithm	101

Major contributions of the thesis

Topic: *image reconstruction from multiple frames of sparse data*

(Issues addressed:

Reconstruction from (a) single frame of sparse and noisy data (b) multiple frames of sparse and noisy data in static and dynamic scene situations.

Problem: *Image reconstruction from single frame of sparse and noisy data*

Solution: (1) *Algorithms are developed to (a) incorporate knowledge about the object as constraints in the reconstruction algorithm using the method of projections onto convex sets (POCS), Tikhonov-Miller (TKM) regularization and TKM-POCS.*

*Quality of the images improves as more and more constraints are **incorporated** in the reconstruction process (Chapter 3).*

*(2) **An artificial neural network (ANN) model is proposed.***

Importance of the constraints is reduced. *Quality of the reconstructed **images** is better than the other methods (Chapter 5).*

Problem: *Image reconstruction from multiple frames of noisy sparse data - Static sensor array, imaging situation*

Solution: (1) *Algorithms are developed to combine multiple frames of sparse and noisy data: obtained from a static situation using the methods POCS and TKM -POCS.*

*Quality of the reconstructed Images improves **significantly** when compared to single frame methods (Chapter 4).*

*(2) **A cascaded ANN model is proposed for combining multiple frames of noisy: sparse data to reconstruct images***

Quality of the reconstructed images improves significantly when compared to single frame methods (Chapter 5).

Problem: ***Image reconstruction from multiple frames of sparse and noisy data - Dynamic scene, situation.***

Solution: *Algorithms are developed to combine multiple frames of data obtained from a dynamic scene situation using cascaded ANN model and the method of TKM-POCS. Both known and unknown cases of motion parameters are considered.*

Quality of the reconstructed images improves significantly when the sequence, of frames of sparse data are combined (Chapter 6).

ABBREVIATIONS AND NOTATIONS

ANN	Artificial Neural Network
BAM	Bidirectional Associative Memory
FT	Fourier Transform
IFT	Inverse Fourier Transform
POCS	Projection Onto Convex Sets
SAI	Sensor Array Imaging
SNR	Signal-to-Noise Ratio
TKM	Tikhonov-Miller
	Smoothness operator
\mathbf{C}^T	transpose of \mathbf{C}
	set of \mathbf{C}
	original image
	original image vector (lexicographically ordered)
	reconstructed image
	set of lexicographically ordered image vectors
	2-D FT of the original image
	sensor array data
	data vector (lexicographically ordered)
	sparse sensor array data
\mathbf{g}_s	sparse data vector (lexicographically ordered)
$\underline{\mathbf{g}}_s$	set of lexicographically ordered sparse data vectors
\mathbf{G}	2-D FT of the sensor array data
\mathbf{G}_s	2-D FT of the sparse sensor array data
h	impulse response function
t_i	2-D transform matrix obtained from h

\mathbf{H}^T	transpose of \mathbf{H}
H	2-D FT of the impulse response function
$\underline{\mathbf{H}}$	set of transformation matrices
$\underline{\mathbf{M}}$	multiframe static imaging model
n	noise data
\mathbf{n}	noise vector (lexicographically ordered)
$\underline{\mathbf{n}}$	set of lexicographically ordered noise vectors
N	2-D FT of noise
P	projection operator
T	relaxed projection operator
$*$	convolution operator
Γ	support region
\mathbb{X}	convex set
Ξ	Hilbert space
κ	sparsity ratio
φ	null set
ρ	regularization operator
τ	relaxation parameter
\cap	intersection operator
$ \cdot $	\mathbf{L}_1 norm

ABSTRACT

There are many situations where it is necessary to reconstruct images of objects from data collected by an array of sensors. In these sensor array imaging (SAI) situations, the collected data is sparse and noisy, and hence the images reconstructed from the data are poor in quality. This thesis addresses the issues in the reconstruction of images from sparse and noisy data. The objective of the thesis is to develop algorithms for the reconstruction of images with improved quality by using the sensor array data together with the available knowledge about the imaging situation.

Mathematically, the reconstruction of an image from sparse data is a problem of solving a set of underdetermined equations. Many solutions exist for this type of problem, as this is an ill-posed problem. However, knowledge about the imaging situation and additional data in the form of multiple frames of sensor array data, can be used to solve this problem. The additional knowledge can be used as constraints in the reconstruction process to obtain images with significantly improved resolution. Algorithms were developed for image reconstruction for the following cases: (i) single frame of data, (ii) multiple frames of data collected in a static imaging situation and (iii) multiple frames of data collected in a dynamic scene situation.

Algorithms were developed based on the methods of Projection Onto Convex Sets (POCS), Tikhonov-Miller (TKM) regularization and TKM-POCS to incorporate known constraints into the solution to extract the best possible image from a single frame of data. These methods require precise knowledge of the constraints about the object, which may not be available always. Therefore, a method based on an artificial neural network (ANN) model, using the principles of bidirectional associative memory, is proposed. This model reduces the importance of these constraints in the reconstruction process. Images reconstructed using the ANN model were found to be significantly better in quality than the images reconstructed using other methods mentioned above, even though

very little knowledge about the object is used as constraints in the reconstruction process.

In practice several frames of sparse data may be available from a given experimental setup. In such a case, the quality of the reconstructed image can be improved significantly, even when there is noise in the data. Algorithms based the methods of **POCS**, **TKM** regularization and a cascaded ANN model were proposed to combine the multiframe data. In this case too, the quality of the images reconstructed using the ANN model is significantly better the images reconstructed using other methods.

In many situations, multiple frames of sensor array data may be available as a sequence of frames as in a dynamic scene situation. In these cases each frame may contain information about the image, but with some unknown motion information superimposed. Reconstruction algorithms are developed for two situations: (a) known motion parameters and (b) unknown motion parameters, but object motion restricted to a small region in successive frames. The quality of the reconstructed image improved as more frames of data in the sequence were used for reconstruction.

Performance of these methods is measured using (a) classification accuracy of a trained neural network and (b) the method of SVD.

INTRODUCTION

1.1 Objective of the thesis

There are many situations where it is necessary to reconstruct images of objects from the data collected by a set of sensors. In these sensor array imaging (SAI) situations, the collected data is sparse and noisy, and hence the images reconstructed from the data are poor in quality. This thesis addresses the issues of sparsity and noise in the data on the resolution and quality of the reconstructed images. We develop algorithms for the reconstruction of images with improved quality by using the sensor array data together with available knowledge about the imaging situation.

1.2 Sensor array imaging

A simplified simulated SAI setup shown in Fig.1.1 is used in the present study. In this setup, the object and the receiver surfaces are assumed to be parallel planes. Each point (s,t) on the object plane is assumed to be a radiating source with appropriate intensity $f(s,t)$ contributing to the field $g(x,y)$ at each point (x,y) on the receiver plane. The data received by the receiver array is given by

$$g(x,y) = \int_{-\infty}^{+\infty} \int_{-\infty}^{+\infty} h(x,y;s,t)f(s,t)dsdt, \quad (1.1)$$

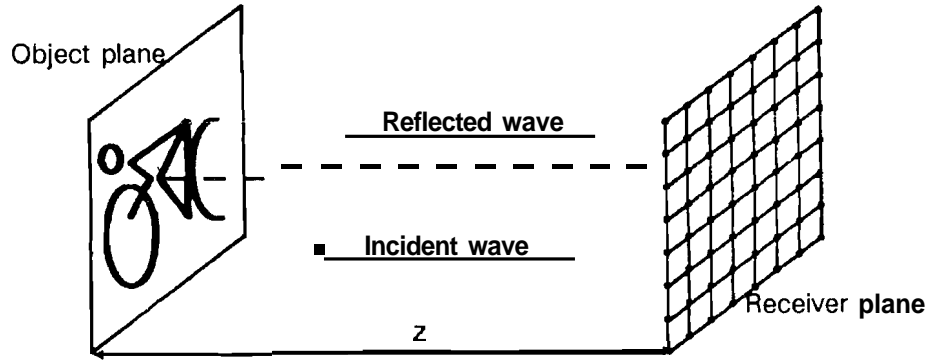


Fig.1.1. A typical SAI setup. The object and receiver planes consists of the same number of points. z is the distance between the object and the receiver. λ is the wavelength of the transmitted wave. The reflected pattern is captured at the receiver plane.

where $h(x,y;s,t)$ is the impulse response function given by

$$h(x,y) = \frac{1}{jz\lambda} e^{jk\sqrt{x^2+y^2+z^2}}, \quad z \text{ is the distance between the object and the}$$

receiver planes, $k = \frac{2\pi}{\lambda}$ is the wave number, and λ is the wavelength of the transmitted plane wave. The process of obtaining the image, given $g(x,y)$ and $h(x,y;s,t)$ is known as *image reconstruction* or *imaging*. If $g(x,y)$ and $h(x,y;s,t)$ are known at all the points and the object and receiver planes have the same number of points, then a simple inversion will generate the exact intensity values $f(s,t)$ on the object plane from the field data $g(x,y)$ on the receiver plane.

The receiver data, besides being sparse, is also noisy. Therefore the received data is modeled as

$$g(x,y) = \int_{-\infty}^{+\infty} \int_{-\infty}^{+\infty} h(x,y;s,t) f(s,t) ds dt + n(x,y) \quad (1.2)$$

where $n(x,y)$ is the Gaussian noise with zero mean. If the impulse response function is stationary, then (1.2) is identified as convolution and is rewritten as,

$$g(x,y) = h(x,y)*f(x,y) + n(x,y), \quad (1.3)$$

where $*$ is used to, denote 2-D convolution. In a simulation setup, we restrict the number of points on the object and the receiver planes to a finite number ($M \times M$) and replace the integration in (1.2) by a summation. The functions with continuous arguments $h(x,y;s,t)$, $f(x,y)$ and $g(x,y)$ are replaced by arrays of $M \times M$ samples taken on 2-D rectangular lattices at equispaced points. The discrete equivalent of SAI model is

$$g(i,j) = \sum_{k=1}^M \sum_{l=1}^M h(i,j;k,l)f(k,l) + n(i,j), \quad (1.4)$$

In a SAI situation the number of receiver elements (sensors) are much fewer than the number of points needed on the object plane for proper resolution of the object. The ratio of the required number of points ($M^o = M_x^o \times M_y^o$, M_x^o and M_y^o are the number of points along the x-axis and y-axis, respectively) on the object plane to the actual number of points ($M^r = M_x^r \times M_y^r$, M_x^r and M_y^r are the number of points along the x-axis and y-axis, respectively) on the receiver plane is defined as sparsity ($\kappa = M^o/M^r$). The ratio κ is always greater than one as $M^o > M^r$. This is because we assume a certain high value for M^o , say 128X128 to represent the image of an object clearly, whereas the number of sensor array elements, N^r , at the receiver plane will be significantly smaller, say 16x16 due to physical limitations in realizing a sensor array system. Hence the images reconstructed from the sparse data will have poor quality. The aim is therefore to appropriately fill in the missing information in $g(i,j)$ and thereby reconstruct an image with improved quality.

In SAI, the image is reconstructed using the following procedure. Using the convolution theorem, the convolution in (1.3) can be written as,

$$G(u,v) = H(u,v)F(u,v) + N(u,v), \quad (1.5)$$

where $G(u,v)$, $F(u,v)$ and $H(u,v)$ are the 2-D Fourier transforms (FT) of $g(x,y)$, $f(x,y)$ and $h(x,y)$, respectively. $N(u,v)$ is the 2-D FT of $n(x,y)$. We assume that the image and the receiver planes have the same number of points. The image $f(x,y)$ is obtained by deconvolution. Multiplying both sides of (1.5) with $H^{-1}(u,v)$ and taking inverse FT (IFT), we obtain the image $f(x,y)$.

$$f(x,y) = IFT[H^{-1}(u,v)G(u,v) - H^{-1}(u,v)N(u,v)], \quad (1.6)$$

where $H^{-1}(u,v)$ is given by [Sutton 79],

$$H^{-1}(u,v) = \begin{cases} e^{ikz\sqrt{1-(\lambda u)^2-(\lambda v)^2}} & \text{for } 1-(\lambda u)^2-(\lambda v)^2 > 0 \\ 0, & \text{otherwise} \end{cases} \quad (1.7)$$

In this study, the sparse data is collected under the following conditions: (a) The object and the receiver planes are parallel. (b) All the receiver elements are aligned in a single plane. (c) There are no disturbances in the medium. (d) The system model is stationary.

Both sparsity and noise contribute to the poor quality of the reconstructed images. But in practice, in addition to this, received data may also be corrupted due to several other reasons.

- Transmission of data over a noisy communication channel may corrupt the data. Image formation mechanism must take care of the medium characteristics [Goutsias 87].
- Receiver and the object planes may not be parallel to each other.
- All the sensors in the receiver plane may not be in the same plane.

- Failure of some receivers will further increase sparsity ($\kappa > 1$).
- Measurement and quantization errors may corrupt the data.

The image reconstructed from data corrupted by one or more of the above will have a poor quality, even when $\kappa = 1$.

1.3 Solutions to sparse data problem

Since the $\kappa > 1$ in a SAI setup, the number of equations for $g(i,j)$'s in (1.4) are less than the number of unknowns ($f(i,j)$). Therefore, this is a problem of underdetermined set of equations. Many solutions exist for such problems [Giordano 85]. This is an ill-posed problem, since the uniqueness of a solution is not satisfied.

Since many solutions exist for underdetermined set of equations, a unique solution can be obtained by selecting the one with minimum norm using pseudoinverse [Giordano 85]. Most often, all the reconstructed images including the minimum norm give images with poor resolution.

There are number of solutions for a sparse data problem satisfying the given set of equations. Ill-posed problems of this type can be solved by incorporating knowledge about the object as constraints in the reconstruction algorithm. Each piece of additional knowledge about the object reduces the solution space and the ignorance about the object being imaged. As a result, resolution of the reconstructed image increases. As more and more constraints are incorporated, the acceptable solution space will be reduced significantly, resulting in an image with improved quality.

1.4 Additional knowledge about the object

In practice, besides the sensor array data, one may have additional knowledge about the object. In this section, we describe four types of knowledge about the object which may be included in the reconstruction process as constraints.

The pixels of an image exist in some interrelated fashion rather than in a random order. Except for the pixels near the edges of an image, almost every pixel will have neighbours. This knowledge about the object is related to the smoothness of the surface of the object and this is the first type of constraint. This can be incorporated as a ***smoothness constraint*** in the reconstruction algorithm.

A second type of knowledge about the object is related to the extent of the object in the image, namely the finite support of the object. The region which encloses the object in an image is known as the support region. The region beyond the support region is assumed to be a non-object region. This knowledge about the object can be incorporated as a ***finite support*** constraint in the reconstruction algorithm.

A third type of knowledge is related to the intensity value of each of the pixel in the reconstructed image. Due to the presence of noise in the sparse data, some of the reconstructed pixels in the image may have negative values, which is not realistic. This knowledge about the image can be incorporated as a ***positivity constraint*** in the reconstruction by suppressing the negative values.

In addition to these constraints, for a given experimental setup, it may be possible to obtain sparse sensor array data for several parameter

settings, like the distance between the object and the receiver or the frequency of the radiating wave. This is called *multiple* frame data. It may also be possible to obtain multiple frames of data as a sequence of sensor array data for different positions/orientations of the object relative to the receiver, as in a dynamic scene situation. The aim of this thesis is to incorporate all known constraints and combine multiple frames of sparse and noisy data to reconstruct images for visual observation of the objects.

1.5 Types of images

The quality of the reconstructed image depends not only on the reconstruction algorithm but also on the nature of the objects being imaged. A 2-D planar object in a real world can be broadly classified into four types. Fig.1.2 shows four types of binary images illustrating different levels of complexity of the object being imaged from reconstruction point of view. Fig.1.2a is an image with several pixels together, thus representing a class of smooth images. Fig.1.2b is an image consisting of smooth regions as well as regions with single pixel width as in the letters of CYCLING. This image is definitely more complex than the image in Fig.1.2a. Fig.1.2c is an image with smooth lines of single pixel width. Here smoothness is confined

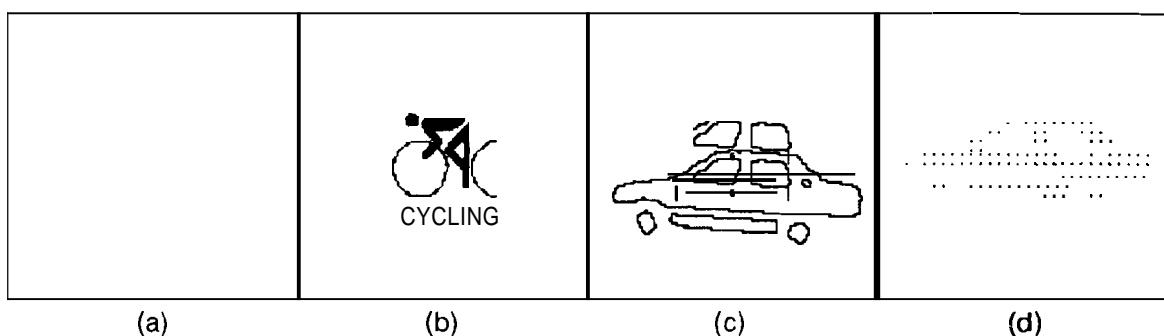


Fig.1.2. Four different types of binary images. (a) A smooth image. (b) An image with smooth regions and smooth lines. (c) An image with smooth lines. (d) An image with isolated pixels.

to only along lines. Fig.1.2d is an image with isolated pixels, and hence is the most difficult of all the four types for reconstruction from sparse data.

From the above discussion, it is clear that the quality of the reconstructed image depends not only on the sparsity ratio κ and noise: but also on the type of the object. For example, the image reconstruction is difficult when the desired image is of the type given in Fig.1.2d to generate sparse data. In our studies, image reconstruction algorithms are tested for various κ values, for two different types of images (Fig.1.2a and 1.2b), and for various SNR values.

The data corresponding to Fig.1.2a is used to study the effect of the known constraints on the quality of the reconstructed image. In order to study the effectiveness of combining multiframe data, we consider the more complex image (Fig.1.2b) for simulation of sparse data. Apart from these images, several images representing olympic symbol set shown in Fig.1.3 are also used for testing the algorithms.

1.6 Quality of reconstruction

The quality of the reconstructed image depends on the purpose for which it is intended. Any type of degradation in a TV image for example, is objectionable for normal viewing. In SAI situations the reconstructed images are poorly resolved and noisy. It may not be possible to identify visually some objects in the reconstructed images. Therefore the quality of the reconstructed images is assessed based on a different criterion. We use the classification accuracy of a trained neural network as a measure of quality of the reconstructed image. We also propose a new quality measure based on the method of singular value decomposition (SVD).

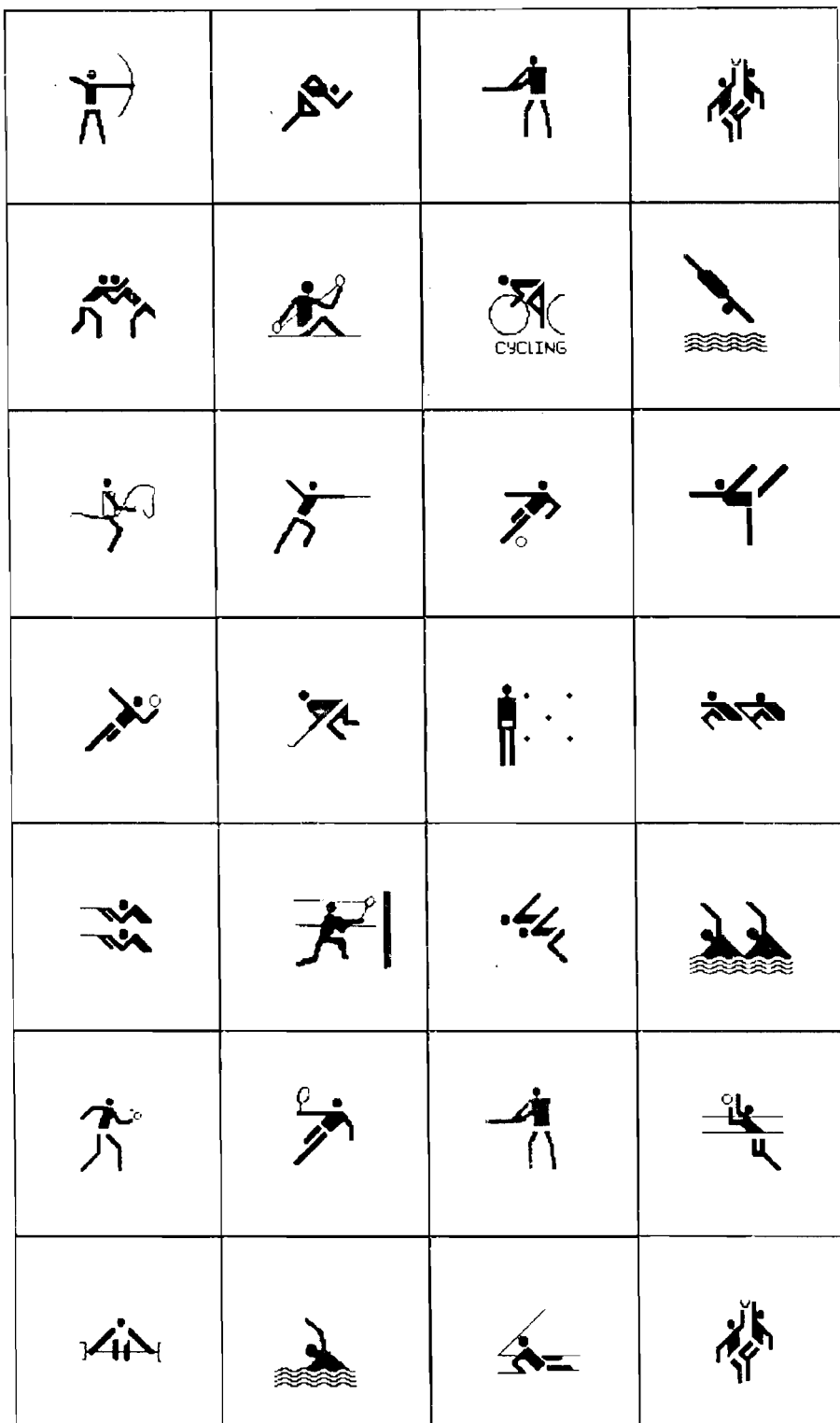


Fig.1.3. Images of some olympic game symbols.

1.7 Sensor array imaging and image processing

Let us assume that there are as many sensors as there are points on the object plane. This is a holographic imaging model where each sensor in the receiver plane receives a weighted sum of all the points on the object plane. Therefore the data is in a transformed domain. Since image reconstruction is a reverse process of data generation, contribution from every sensor is very important to obtain the image at each pixel. As $\kappa > 1$, there will be no contribution from the missing sensors. As a result all pixels in the reconstructed image are affected. Image processing techniques like histogram equalization, edge enhancement, mean/median filtering and morphological filtering [Yegnanarayana 90a] are not suitable to process the reconstructed image. Therefore, methods are proposed to incorporate constraints during reconstruction and also combine multiple frames of sparse data to improve the quality.

1.8 Organization of the thesis

The thesis is organized as follows: In Chapter 2, we review solutions to ill-posed problems, namely reconstruction with a single frame of data with known constraints and methods of combining multiple frames of data. We also review literature related to image reconstruction using artificial neural network models.

In Chapter 3, we discuss methods to incorporate various constraints into the solution and extract maximum information from a single frame of sparse and noisy data. In particular, we propose algorithms based on Tikhonov-Miller (TKM) regularization, the method of Projection Onto Convex Sets (POCS), and a method based on both TKM regularization and POCS

for image reconstruction. We discuss a quality measure for the reconstructed image based on the classification accuracy of a trained neural network.

In practice several frames of sparse data may be available from a given experimental set up. In such a case, the quality of the reconstructed image can be improved significantly by combining the multiple frames of data, even when the data is sparse and noisy data. In Chapter 4, we discuss methods of image reconstruction from multiple frames of sparse and noisy data.

Methods based on POCS and TKM regularization require precise knowledge of the constraints about the object, which may not be available always. In Chapter 5, we propose a method based on artificial neural network (ANN) model for reconstruction of an image from a single frame of sparse and noisy data. This method reduces the importance of the constraints. An ANN model is also proposed for image reconstruction from multiple frames of sparse and noisy data. We also discuss a new quality measure based on the method of SVD.

In Chapter 6, a dynamic scene situation is considered for collecting a sequence of multiple frames of sparse data. In these cases each frame may contain information about the image, but with the unknown motion information superimposed in each frame. Reconstruction algorithms are developed for two situations: (a) known motion parameters and (b) unknown motion parameters. In the latter case, methods are discussed for the case when the object motion is restricted to a small region in successive frames and for the case when the object motion is unrestricted. The last chapter gives a summary of this thesis.

A REVIEW OF IMAGE RECONSTRUCTION METHODS

In this Chapter, we review some existing solutions to ill-posed problems within the framework established in Chapter 1. Conventional image restoration is a well studied problem and large amount of literature exists on this topic. On the other hand, not many attempts have been made for image reconstruction from sparse data. Since both the problems belong to the class of ill-posed problems, we discuss methods used for restoration of images. We restrict our review to general methods and algorithms which have a direct bearing on the problem of image reconstruction from sparse data.

2.1 Methods of solutions from a single frame of data

We consider first image reconstruction using *inverse filtering*. If the imaging model is known accurately, the noiseless case with the sparsity ratio $A = 1$, inverse filtering is the best method for image reconstruction. If the model is unknown, then inverse filtering method fails to provide an acceptable result. To illustrate the effect of noise on inverse filtering, we assume that the data is corrupted by noise. From (1.5), the image f can be reconstructed as follows:

$$F = \frac{G}{H} - \frac{N}{H}, \quad f = IFT \bigcirc \left(\frac{G}{H} - \frac{N}{H} \right) \quad (2.1)$$

The indices are dropped for convenience. The term $\mathbf{N}^*\mathbf{H}$ will be quite large for low SNR data, and the reconstructed image will be dominated by noise. Undesirable results may also occur due to very small (near zero) values at certain spatial frequencies of \mathbf{H} .

In order to reduce the effect of noise, it is reasonable to define constraints and to incorporate them in the minimization of error [Phillips 62]. One way to avoid the large fluctuations in the solution is to find an image $\hat{\mathbf{f}}$ in such a way that $\|\hat{\mathbf{f}} - \mathbf{f}\|^2$ is minimized where $\|\cdot\|$ is the \mathbf{L}_2 norm. In other words, $\hat{\mathbf{f}}$ is found such that $\|\hat{\mathbf{f}} - \mathbf{f}\|^2 \leq \|\mathbf{N}\|^2$. Minimization is done based on the assumption that the total energy of the noise signal $\|\mathbf{N}\|^2$ is known. Wiener filter [Gonzalez 87, Wahl 87] is used to minimize $\|\hat{\mathbf{f}} - \mathbf{f}\|^2$. The solution to the ill-posed problem in this case is given by

$$\hat{F} = \left(\frac{H^*}{H^*H + P_N/P_f} \right) G \quad (2.2)$$

where \hat{F} is the FT of $\hat{\mathbf{f}}$, H^* is the complex conjugate of H , P_N is the power spectrum of the noise and P_f is the power spectrum of the image. This reduces to inverse filtering in the noise-free case. Pratt and Davarian [Pratt 77] presents a fast computational techniques for Wiener image restoration.

Singular value decomposition (SVD) is another noniterative reconstruction method for spatially invariant systems [Andrews 74, Huang 75b, Shim 81]. The trade off between the amount of noise and the signal quality is obtained by restricting the number of singular values used for reconstruction. Here, it is assumed that the undesirable effects in the ill-posed problem are due to the eigenvectors corresponding to smaller singular values. These vectors are not used in the image reconstruction

process. The optimum value for the number of terms is chosen manually by reducing the number of smaller singular values and it is stopped when a good quality image is reconstructed.

Another approach to overcome the ill-posed nature of the early vision problems is based on Bayesian estimation and Markov random field (MRF) models. In this approach, the *a priori* knowledge about the object is represented in terms of an appropriate probability distribution. This distribution together with a probabilistic description of the noise allows one to compute the posterior distribution $P_{\mathbf{f}|\mathbf{g}}$, which represents the likelihood of a solution $\hat{\mathbf{f}}$ given the observations \mathbf{g} . In this way, one can solve the reconstruction problem by finding the estimate that either maximizes this *a posteriori* (MAP) probability distribution or minimizes the expected value (with respect to $P_{\mathbf{f}|\mathbf{g}}$) of an appropriate error function [Marroquin 87].

A major issue in the optimization methods described above is the choice of suitable objective function. These formulations guarantee a single solution. An unrealistic objective function may lead to unacceptable solutions, as they may incorporate erroneous information about the object. As there are uncertainties surrounding these problems, it is more realistic to provide a region of acceptable solution space rather than a single solution [Combette 93]. The most straightforward approach to obtain acceptable solutions is to incorporate all available knowledge about the object in the problem formulation. In this formulation, each piece of knowledge about the object is represented by a set in the solution space and the intersection of such sets constitutes a feasible solution set. A solution is called a feasible solution, if it satisfies all the constraints imposed on the solution [Trussel 84]. If each set is a convex set, then the method

of Projection Onto Convex Sets (POCS) can be used to obtain a solution from the feasible solution set [Youla 82].

2.2 Solutions from multiple frames of data

Hunt and Kubler [Hunt 84] have formulated a multichannel image restoration filter in which the mean square error between the ideal and the restored image is minimized. Here the multichannel images refer to the red, green and blue channel (color) images. The restoration method uses both the within channel and between channels correlations. This method is based on the assumption that the covariance matrix formed by the image vector is separable into spatial and spectral components. This separability assumption enables the decorrelation of the channels based on the Karhunen-Loeve transformation. In other words, this transformation makes the information from all the channels orthogonal. They have shown that multichannel restoration of the transformed signal under this assumption is equivalent to the independent restoration of individual channels.

Galatsanos and Chin [Galatsanos 89] have proposed a Wiener based solution that utilizes the advantage of the special structure of the correlation matrix of the multichannel image. The Wiener based filter does not require the spectral and the spatial separability assumption as in [Hunt 84].

Ozkan et al [Ozkan 92] have discussed multiframe Wiener filtering algorithms which account for both spatial and temporal correlations for restoring image sequences degraded by both blur and noise. A motion compensated multiframe Wiener filter, where the motion parameters have been estimated from a motion detection algorithm, has also been suggested.

Approaches based on Wiener filtering require that all the multiframe data be present at the same time for computation. The dimensionality of the correlation matrices significantly increases when the number of frames increase. Moreover, if some of the frames of data do not correlate well with the other frames, multiframe image reconstruction scheme may not result in a good quality image. In the worst case, the reconstructed image may not be better than the image reconstructed using any of the single frame methods. In such a case, it is necessary to devise a mechanism to discard frames that do not correlate well with the existing ones.

Multiframe approaches discussed above depend critically on the accurate estimation of the cross correlation of the multiband images. Sezan and Trussel [Sezan 89] have shown that the multispectral Wiener solution that takes into account the cross correlations between image channels may be very sensitive to the estimates of the cross correlations. The use of a *priori* information and its effect on multiband image restoration was considered. A set-theoretic framework for incorporating a number of convex-type constraints was suggested for simultaneous use of a *priori* within-band and between-band properties of the images. The multiband restoration was carried out using the Projections Onto Convex Sets (POCS).

Katsaggelos and Paik [Katsaggelos 88] have proposed iterative techniques for restoring color images. The inter-channel correlation was incorporated into the restoration algorithm by using the result of the first channel restoration as the initial estimate for the other two channels. The iterative restoration algorithms were based on the regularization technique where the solution vector satisfied the smoothness constraint and was also consistent with the data.

Galatsanos et al [Galatsanos 91] have suggested a least squares filter for multichannel images. Two approaches based on constrained optimization and set theoretic methods have been used to derive restoration filters. This is an extension of the method proposed by Katsaggelos et al [Katsaggelos 91]. Knowledge about the image restricts the solution to lie in an ellipsoid. The resultant solution was found from the intersection of all such sets obtained from multiframe data along with another ellipsoid defined by the smoothness constraint.

Galatsanos and Chin [Galatsanos 91] have developed a Kalman filter for optimal restoration of multichannel images. The filter was derived using a semicausal image model that included between-channel correlation. Multichannel filters for stationary and nonstationary image models were developed.

Kim et al [Kim 90] have proposed a method to reconstruct high resolution images from multiple frames of low resolution images. Using the aliasing relationship between the undersampled frames and the reference frame, a weighted recursive least-squares algorithm was developed.

Irani and Peleg [Irani 90] have developed an iterative algorithm to improve the resolution of an image in an image sequence. The approach is similar to back-projection used in tomography. Knowledge about the imaging process and the relative displacement of images were used to reconstruct a high resolution image.

Mariadassou and Yegnanarayana [Mariadassou 90] have developed methods based on POCS and Projection Onto NonIntersection Convex Sets (PONICS) to reconstruct images from multiple frequency sparse data. They

developed a method of applying the operators in parallel and showed that, if the constraints were consistent and the convex sets had nonempty intersection, then both serial and parallel methods gave the same set of fixed points. They have shown that **PONICS** method could be used even when the intersection of the convex sets was empty.

Burl [Burl 93] has proposed an extended Kalman filter to reduce the noise in sequential images and to estimate the velocity of a moving object. A nonlinear state space model describing the evolution of a sequence of images containing a moving object has been proposed. The state of this system consists of both the image and the velocity of the moving object. Parallel extended Kalman filter algorithm has been proposed.

Integration of images from different sensing modalities can produce information that cannot be obtained by viewing the sensor output separately and consecutively. Toet et al [Toet 91] had introduced a hierarchical image merging scheme based on a multiresolution contrast decomposition. The method assumed that the images obtained from thermal and visual images could be registered exactly.

2.3 Artificial neural networks for ill-posed problems

Many attempts have been made to develop ANN models to solve inverse problems in computer vision. For most of the ANN models, their learning or restoration capabilities are expressed in terms of minimization of some cost functional. An approach based on Hopfield neural network has been proposed for restoration of gray level images distorted by a shift-invariant blur function and additive noise [Zhou 88]. The restoration procedure consists of two stages: estimation of the parameters of the neural network

and restoration of images. The parameters of the neural network are obtained by comparing the energy functions of the neural network and the imaging model. Nonlinear restoration procedure is carried out in the second stage to minimize the energy function.

A modified Hopfield network has been suggested for regularized image restoration [Paik 92]. This model was used in developing algorithms with sequential, n-simultaneous and partially asynchronous modes of updates. Convergence analysis was provided for all the cases. Faster computational times were claimed over the algorithm developed by Zhou et al [Zhou 1988].

Abiss et al [Abiss 91] have proposed a method based on Hopfield neural network model for superresolution problem. In this method also, the parameters of the ANN were established by mapping the energy function of the neural network with the imaging model.

The models proposed by Zhou et al [Zhou 88], Abiss et al [Abiss 91] and Paik [Paik 92] solve the image restoration by using the Hopfield model as an optimization tool. The interconnections strengths and the input to the network are determined in terms of the energy function of the neural network. They use the energy minimization property of the ANN and minimize the energy function using some constraints.

Poggio and Girosi [Poggio 90] have suggested networks to solve the problem of hypersurface reconstruction. They have regarded learning (an input-output mapping from a set of examples) as a problem of synthesizing an associative memory, and approached the problem of learning in the neural network from the point of view of approximation theory. A theoretical framework has been suggested based on regularization technique which

led to the class of three-layer networks. They are called **regularization networks**. These networks have feedforward, multilayer architecture. It was shown that these networks were capable of approximating any multivariate functions.

Kulkarni [Kulkarni 91] has proposed an ANN architecture based on SVD for estimation of an object function from indirect measurements. The ANN model is a feedforward network with six layers. The weights in this model encode the impulse response function. The weights were initialized based SVD of the impulse response function. The estimated autocorrelation function was compared with the known autocorrelation function to calculate the error. The weights were updated iteratively to minimize the error. The weights were learnt in such a way that the error due to small singular values were reduced.

Farhat and Bai [Farhat 89] have suggested an ANN for echo inversion and target shape estimation from incomplete frequency data. The ANN accomplished inversion and estimation of the object function by minimizing a cost functional based on the measured data. An iterative algorithm has been proposed to minimize the energy function to give the desired image as its neural state outputs.

Hurlbert [Hurlbert 88,921] has proposed approaches for the implementation of color constancy for machine vision. An algorithm for lightness problem to recover reflectance from image irradiance has been proposed. The regularization operator was synthesized by associative learning from a set of examples. They showed that the regularization operator might be synthesized if sufficient set of correct input-output pair was made available to the system.

In this chapter, we have reviewed methods for solving ill-posed problems. Most of the methods were used for restoring blurred images. In the next chapter, we develop algorithms based on the method of POCS and the method of TKM regularization method to incorporate smoothness, positivity and finite support constraints to reconstruct images with improved quality from noisy sparse data. In chapter 4, we propose new algorithms to combine multiple frames and incorporate knowledge about the object to improve the quality of the reconstructed significantly. These algorithms incorporate inter-frame correlations indirectly and do not impose any constraint on the number of multiple frames to be used for reconstruction process. In chapter 5, we propose ANN models similar to bidirectional associative memory (BAM) in which the bidirectional process of data generation and image reconstruction is simulated. The interconnection strengths are directly encoded using the impulse response function of the SAI model [Yegnanarayana 93] and not based on the estimation methods used by Zhou et al [Zhou 88], Paik et al [Paik 92], and Abbiss et al [Abiss 91].

IMAGE RECONSTRUCTION FROM SINGLE FRAME DATA

Having stated that the problem of image reconstruction from sparse data is an ill-posed problem and that it can be solved by incorporating known constraints in the reconstruction process, we now investigate the influence of constraints on the quality of the reconstructed images. We propose algorithms based on the methods of POCS and TKM regularization to incorporate knowledge about objects as constraints in the image reconstruction process. The quality of the reconstructed images is compared with the images obtained by Inverse filtering, the method of POCS and the method of TKM regularization using the classification accuracy of a trained neural network.

A shorthand notation of (1.4) is obtained by stacking the image $f(i,j)$, the data $g(i,j)$ and the noise term $n(i,j)$ in a vector form (called as lexicographic ordering, see Appendix).

$$\mathbf{g} = \mathbf{H}\mathbf{f} + \mathbf{n}. \quad (3.1)$$

Here \mathbf{g} , \mathbf{f} , and \mathbf{n} are arranged in the lexicographically ordered vectors of size $M^2 \times 1$, where $M \times M$ is the size of the image, data and the noise term. If circular convolution is assumed, the matrix \mathbf{H} (of size $M^2 \times M^2$) has a block-circulant structure (see Appendix). Here \mathbf{g} refers to the data corresponding to $\kappa = 1$. When $\kappa > 1$, the data is represented by \mathbf{g}_κ . The operator \mathbf{H} is a block-Toeplitz matrix which is constructed from the impulse

response function $h(i,j;k,l)$. The image reconstruction problem is viewed as that of obtaining an estimate of \mathbf{f} from the sparse data \mathbf{g}_s .

3.1 Tikhonov-Miller regularization

In this section, we present the method of TKM regularization. This method has been used widely in applications related to restoration of blurred images. In this chapter, we discuss its relevance to the problem of image reconstruction from sparse data.

The main idea of this method is to define a criterion to find an approximate solution from a set of solutions. The class of solutions are defined based on the model given in (3.1) and is described by

$$\psi_1(\hat{\mathbf{f}}) = ||\mathbf{g}_s - \mathbf{H}\hat{\mathbf{f}}|| \leq ||\mathbf{n}|| = \Lambda, \quad (3.2)$$

where $\hat{\mathbf{f}}$ is the reconstructed image. The bound Λ is related to sparsity and noise in the observed data. The set of solutions which satisfies the condition in (3.2) is a feasible solution set. In order to reduce this set further, knowledge about the object can be incorporated. A regularized solution is one which minimizes a stabilizing functional on the set of feasible solutions [Bertero 88, Demoment 89, Karayiannis 90, Nashed 81, Tikhonov 77, Tikhonov 87, Sarkar 81]. The stabilizing functional is written as follows:

$$\psi_2(\hat{\mathbf{f}}) = ||\mathbf{C}\hat{\mathbf{f}}||. \quad (3.3)$$

Here \mathbf{C} is a real valued matrix of size $M^2 \times M^2$ and is restricted to have a block circulant form. In general \mathbf{C} is known as the *regularization operator*. The properties and the values of \mathbf{C} will be discussed later. Equation (3.3) measures the extent to which the reconstructed image conforms to the

smoothness constraint. In another approach [Miller 70], the minimization of $\psi_2(\hat{\mathbf{f}})$ is done as follows:

$$\psi_2(\hat{\mathbf{f}}) = ||\mathbf{C}\hat{\mathbf{f}}|| \leq \lambda. \quad (3.4)$$

Here λ is a bound which is related to the smoothness of the image. Now, it is required to find a $\hat{\mathbf{f}}$ that minimizes both $\psi_1(\hat{\mathbf{f}})$ and $\psi_2(\hat{\mathbf{f}})$. In Tikhonov-Miller approach, the two constraints (3.2) and (3.3) are combined quadratically into the constraint

$$\Psi(\hat{\mathbf{f}}) = \left(\frac{1}{\Lambda^2}\right) ||\Psi_1(\hat{\mathbf{f}})||^2 + \left(\frac{1}{\lambda^2}\right) ||\Psi_2(\hat{\mathbf{f}})||^2 \leq 2$$

$$||\mathbf{g}_s - \mathbf{H}\hat{\mathbf{f}}||^2 + \left(\frac{\lambda}{\Lambda}\right)^2 ||\mathbf{C}\hat{\mathbf{f}}||^2 \leq 2\Lambda^2 \text{ (multiplying both sides by } \Lambda^2 \text{)}$$

$$||\mathbf{g}_s - \mathbf{H}\hat{\mathbf{f}}||^2 + \rho ||\mathbf{C}\hat{\mathbf{f}}||^2 \leq 2\Lambda^2$$

$$\text{or } \mathbf{E} + \rho \mathbf{S} \leq 2\Lambda^2. \quad (3.5)$$

Here $\mathbf{E} = ||\mathbf{g}_s - \mathbf{H}\hat{\mathbf{f}}||^2$, $\mathbf{S} = ||\mathbf{C}\hat{\mathbf{f}}||^2$ and $\rho = \left(\frac{\lambda}{\Lambda}\right)^2$. The parameter ρ is known as the *regularization parameter*. The regularized solution is obtained by minimising the objective function (3.5) with respect to $\hat{\mathbf{f}}$. A vector $\hat{\mathbf{f}}$ that minimizes $\Psi(\hat{\mathbf{f}})$ becomes the reconstructed image. If such a minimizing solution exists, then the first derivative of $\Psi(\hat{\mathbf{f}})$ must vanish, i.e.,

$$\frac{\partial \Psi}{\partial \hat{\mathbf{f}}} = \frac{\partial \mathbf{E}}{\partial \hat{\mathbf{f}}} + \rho \frac{\partial \mathbf{S}}{\partial \hat{\mathbf{f}}} = 0 \quad (3.6)$$

If $||\mathbf{g}_s - \mathbf{H}\hat{\mathbf{f}}|| \rightarrow 0$, the term \mathbf{S} loses its importance in minimising $\Psi(\hat{\mathbf{f}})$. The contribution from \mathbf{S} can be neglected by setting ρ to zero. As the data is sparse, the term $||\mathbf{g}_s - \mathbf{H}\hat{\mathbf{f}}||$ does not approach zero and therefore, it is required to find an optimum ρ which minimizes the function $\Psi(\hat{\mathbf{f}})$. The

regularization parameter ρ is chosen in such a way that it strikes a balance between the degree of regularization and the closeness of the estimated data to the original data. The degree of regularization depends on the amplitude of the regularization parameter ρ . If the value of the regularization parameter is too large, the reconstructed image would be a blurred one and error due to regularization dominates the reconstructed image. On the other hand, if the regularization parameter is too small, noise due to the first term would dominate. The value of the regularization parameter is often adjusted by visually inspecting the resulting image. Methods for estimating this parameter are discussed in the literature [Dinten 91, Galatsanos 92, Kay 91, Reeves 90, Titterton 91].

Selection of the operator \mathbf{C} is also crucial in obtaining an optimum solution [Katsaggelos 91, Lagendijk 88]. Properties of this operator is based on the properties of H . If H is a low-pass filter, \mathbf{C} is chosen to be a high-pass filter. In general, the regularizing operator complements the properties of H . Usually Laplacian operator of the type given below is used for constructing the regularization operator \mathbf{C} [Lagendijk 91].

$$\mathbf{L} = \begin{bmatrix} 0 & -1 & 0 \\ -1 & 4 & -1 \\ 0 & -1 & 0 \end{bmatrix} \quad (3.7)$$

If \mathbf{f} and \mathbf{g} are of size $M^2 \times 1$, then the matrix \mathbf{C} has M^2 partitions and each partition consists of $M \times M$ elements. The matrix \mathbf{C} is constructed as follows:

$$\mathbf{C} = \begin{bmatrix} \mathbf{C}_1 & \mathbf{C}_M & \mathbf{C}_{M-1} & \dots & \mathbf{C}_2 \\ \mathbf{C}_2 & \mathbf{C}_1 & \mathbf{C}_M & \dots & \mathbf{C}_3 \\ \mathbf{C}_3 & \mathbf{C}_2 & \mathbf{C}_1 & \dots & \mathbf{C}_4 \\ \dots & \dots & \dots & \dots & \dots \\ \dots & \dots & \dots & \dots & \dots \\ \mathbf{C}_M & \mathbf{C}_{M-1} & \mathbf{C}_{M-2} & \dots & \mathbf{C}_1 \end{bmatrix} \quad (3.8)$$

where each submatrix \mathbf{C}_j is a matrix of size $M \times M$ and is constructed from the j th row of the extended matrix \mathbf{L} . \mathbf{C}_j is constructed as follows:

$$\mathbf{C}_j = \begin{bmatrix} L(j,1) & L(j,M) & L(j,M-1) & \dots & L(j,2) \\ L(j,2) & L(j,1) & L(j,M) & \dots & L(j,3) \\ L(j,3) & L(j,2) & L(j,1) & \dots & L(j,4) \\ \dots & \dots & \dots & \dots & \dots \\ L(j,M) & L(j,M-1) & L(j,M-2) & \dots & L(j,1) \end{bmatrix}, \quad (3.9)$$

where $L(j,i)$ is the element (j th row and i th column) of \mathbf{L} .

3.1.1 Formulation of the algorithm

A solution to (3.5) is equivalent to the solution of the matrix equation which satisfies the conditions given in (3.2) and (3.4). Rewriting (3.6), we get

$$\frac{\partial \Psi}{\partial \hat{\mathbf{f}}} = \frac{\partial}{\partial \hat{\mathbf{f}}} \|\mathbf{g}_s - \mathbf{H} \hat{\mathbf{f}}\|^2 + \rho \frac{\partial}{\partial \hat{\mathbf{f}}} \|\mathbf{C} \hat{\mathbf{f}}\|^2 = 0 \quad (3.10)$$

$$(\mathbf{g}_s - \mathbf{H} \hat{\mathbf{f}})(-\mathbf{H}^T) + \rho \mathbf{C}^T \mathbf{C} \hat{\mathbf{f}} = 0 \quad (3.11)$$

or

$$(\mathbf{H}^T \mathbf{H} + \rho \mathbf{C}^T \mathbf{C}) \hat{\mathbf{f}} = \mathbf{H}^T \mathbf{g}_s \quad (3.12)$$

The solution is given by

$$\hat{\mathbf{f}} = (\mathbf{H}^T \mathbf{H} + \rho \mathbf{C}^T \mathbf{C})^{-1} \mathbf{H}^T \mathbf{g}_s. \quad (3.13)$$

Note that if \mathbf{C} is a null operator (i.e., no constraint is imposed on the image), then the solution reduces to the classical least squares solution [Dines 77, Pratt 91]. As the sizes of both \mathbf{C} and \mathbf{H} are large, the direct inversion is not convenient. Therefore we opt for an iterative solution [Huang 75a, Hunt 73, Katsaggelos 91, Kawata 80a, Kawata 80b]. Conjugate gradient method can

be used to minimize the function $\Psi(\hat{\mathbf{f}})$ iteratively [Angel 78, Kawata 80, Press 92, Schaffer 81]. If the solution after k iterations is denoted by $\hat{\mathbf{f}}_k$, then after $k + 1$ iterations we have [Giordano 85],

$$\hat{\mathbf{f}}_{k+1} = \hat{\mathbf{f}}_k - \frac{1}{2}\beta \left. \frac{\partial \Psi}{\partial \hat{\mathbf{f}}} \right|_{\hat{\mathbf{f}}_k} \hat{\mathbf{f}}_k \quad (3.14)$$

This equation refers to the descent direction from $\hat{\mathbf{f}}_k$ to $\hat{\mathbf{f}}_{k+1}$. The descent is achieved by minimizing along the line from $\hat{\mathbf{f}}_k$ in the direction of the downhill gradient $-\left. \frac{\partial \Psi}{\partial \hat{\mathbf{f}}} \right|_{\hat{\mathbf{f}}_k}$. The parameter β dictates how far to move in the downhill gradient direction. In other words, it controls the convergence of the iterations. The gradient $\left. \frac{\partial \Psi}{\partial \hat{\mathbf{f}}} \right|_{\hat{\mathbf{f}}_k}$ is obtained by differentiating (3.5) with respect to $\hat{\mathbf{f}}$. Now,

$$\left. \frac{\partial \Psi}{\partial \hat{\mathbf{f}}} \right|_{\hat{\mathbf{f}}_k} = 2 \left[\left(\mathbf{H}\mathbf{H}^T + \rho \mathbf{C}^T \mathbf{C} \right) \hat{\mathbf{f}}_k - \mathbf{H}^T \mathbf{g}_s \right] \quad (3.15)$$

Using (3.15), now (3.14) is written as follows:

$$\hat{\mathbf{f}}_{k+1} = \hat{\mathbf{f}}_k - \frac{1}{2}\beta \left[2 \left\{ \left(\mathbf{H}\mathbf{H}^T + \rho \mathbf{C}^T \mathbf{C} \right) \hat{\mathbf{f}}_k - \mathbf{H}^T \mathbf{g}_s \right\} \right] \quad (3.16)$$

$$\begin{aligned} &= \hat{\mathbf{f}}_k + \beta \left[\mathbf{H}^T \mathbf{g}_s - \left(\mathbf{H}^T \mathbf{H} + \rho \mathbf{C}^T \mathbf{C} \right) \hat{\mathbf{f}}_k \right] \\ &= \hat{\mathbf{f}}_k + \beta \mathfrak{R} \end{aligned} \quad (3.17)$$

where $\mathfrak{R} = \left[\mathbf{H}^T \mathbf{g}_s - \left(\mathbf{H}^T \mathbf{H} + \rho \mathbf{C}^T \mathbf{C} \right) \hat{\mathbf{f}}_k \right]$. The structure of the matrix \mathfrak{R} is same as the structures of \mathbf{H} and \mathbf{C} . As the matrices \mathbf{H} and \mathbf{C} have block-Toeplitz structure, \mathfrak{R} also has the same structure. A block-Toeplitz matrix can be approximated by a block-circulant matrix because these two types of matrices are closely related (see Appendix). Operations involving

block-circulant matrix can be efficiently evaluated using 2-D FT [Gonzalez 87]. Therefore, \mathfrak{K} can be evaluated using the 2-D FT.

Algorithms based on the TKM regularization have the following advantages: they are iterative and lead to a feasible solution. The disadvantages are due to its formulation. Reconstruction algorithms depends on the image characteristics. They need to be tuned for different types of images. The rate of convergence of these algorithms is generally slow, and there is no good criterion to terminate the iterations in the algorithms [Wolberg 90]. This algorithm is stopped by visually checking the quality of the reconstructed image after each iteration.

There are other known constraints which cannot be expressed in an analytical form as in (3.3). These constraints however can be incorporated as deterministic constraints in the reconstruction algorithm. In the next section, we discuss a method based on POCS to obtain a solution set which satisfies several deterministic constraints simultaneously. We show that the iterative method described in this section can be combined with the method of POCS [Youla 82,87].

3.1.2 The method of *POCS*

A set of functions or images $\{\hat{\mathbf{f}}_i, i = 1, 2, 3, \dots, N\}$ is a convex set if, for any two elements $\hat{\mathbf{f}}_1$ and $\hat{\mathbf{f}}_2$ in the set, all the linearly interpolated combinations

$$\hat{\mathbf{f}}_3 = \mu \hat{\mathbf{f}}_1 + (1 - \mu) \hat{\mathbf{f}}_2, \quad 0 \leq \mu \leq 1 \quad (3.18)$$

are also in the same set. Many of the deterministic constraints that one might want to impose on the solution define convex sets. Some of them

are (a) positivity, (b) finite support and (c) known bounds for a specific function (e.g., the image intensity lies between 20 and 100). To generalize, we assume that there are m such constraints and therefore there are m convex sets ($\mathcal{X}_i, i = 1, 2, 3, \dots, m$).

A solution set is obtained by the intersection of all such sets: $\mathcal{X} = \bigcap_i \mathcal{X}_i, \quad i = 1, 2, 3, \dots, m$. Let us call this set \mathcal{X} as the feasible solution set. Any point (image) in \mathcal{X} is called as the set theoretic estimate and is acceptable. This estimate is consistent provided $\mathcal{X} \neq \varphi$.

Once the solution set is defined, the next task is to compute the set theoretic estimate, i.e., the problem of finding a point in the feasible solution set. The method of POCS can be used to select a solution. This method requires that all the knowledge about the object belong to some known convex set.

Let \mathcal{X}_i denote any convex set belonging to the Hilbert space Ξ , and let $\hat{\mathbf{f}}_i \in \Xi$. The element $P_i \hat{\mathbf{f}}_i$ obtained by projecting $\hat{\mathbf{f}}$ onto \mathcal{X}_i by the projection operator P_i is the element in \mathcal{X}_i closest to $\hat{\mathbf{f}}_i$. Since \mathcal{X}_i is a convex set, $P_i \hat{\mathbf{f}}_i$ exists and is uniquely determined by

$$|| \hat{\mathbf{f}}_i - P_i \hat{\mathbf{f}}_i || = \min_{y \in \mathcal{X}_i} || \hat{\mathbf{f}}_i - y || \quad (3.19)$$

The rule which assigns to every $\hat{\mathbf{f}}_i \in \Xi$ its nearest neighbour in \mathcal{X}_i defines the nonlinear projection operator $P_i : \Xi \rightarrow \mathcal{X}_i$ without ambiguity. If the projection of $\hat{\mathbf{f}}$ onto \mathcal{X}_i leaves $\hat{\mathbf{f}}$ unaltered, i.e., $P_i \hat{\mathbf{f}} = \hat{\mathbf{f}}$, then $\hat{\mathbf{f}}$ is a fixed point belonging to \mathcal{X}_i .

As mentioned earlier, in this method a set of solutions is obtained rather than a single solution. Therefore, the problem here is to find at least one member belonging to feasible set K . If a projection operator P onto the convex set \mathfrak{K} is available, then a direct application of this operator will result in the required solution. Realizing P in practice is very difficult. Therefore, this is solved by applying recursively the individual projection operators P_i onto K . Every point of K , is a fixed point for each of projection operator P_i . Also every point in K is a fixed point for the operator $P = P_m P_{m-1} P_{m-2} P_{m-3} \dots P_1$ such that $P \hat{\mathbf{f}}_i = \hat{\mathbf{f}}_i$. A solution is obtained by the following recursive procedure:

$$\begin{aligned}
 \hat{\mathbf{f}}_1 &= P_m P_{m-1} P_{m-2} P_{m-3} \dots P_1 \hat{\mathbf{f}}_0 = P^1 \hat{\mathbf{f}}_0 \\
 \hat{\mathbf{f}}_2 &= P_m P_{m-1} P_{m-2} P_{m-3} \dots P_1 \hat{\mathbf{f}}_1 = (P_m P_{m-1} P_{m-2} P_{m-3} \dots P_1)^2 \hat{\mathbf{f}}_0 = P^2 \hat{\mathbf{f}}_0 \\
 &\dots \dots \dots \\
 &\dots \dots \dots \\
 \hat{\mathbf{f}}_k &= P_m P_{m-1} P_{m-2} P_{m-3} \dots P_1 \hat{\mathbf{f}}_{k-1} = P^k \hat{\mathbf{f}}_0 \quad k = 1, 2, 3, \dots, \infty. \quad (3.20)
 \end{aligned}$$

where $\hat{\mathbf{f}}_0$ is any arbitrary point belonging to 5. It has been shown that $\hat{\mathbf{f}}_k$ converges towards a point in K [Twomey 63].

The iterations converge to a solution in \mathfrak{K} for any initial estimate $\hat{\mathbf{f}}_0$, provided $\mathfrak{K} \neq \varphi$. If \mathfrak{K} is empty, then the iterations do not converge. Properties of the limiting solution $\hat{\mathbf{f}}_\infty$ depend on the initial estimate [Trussel 83, Trussel 84]. Convergence of the iterations is slow near the intersection region of the convex sets. This is illustrated geometrically in Fig.3.1a. In order to speedup the iterative procedure, the projection is extended beyond the boundaries as follows:

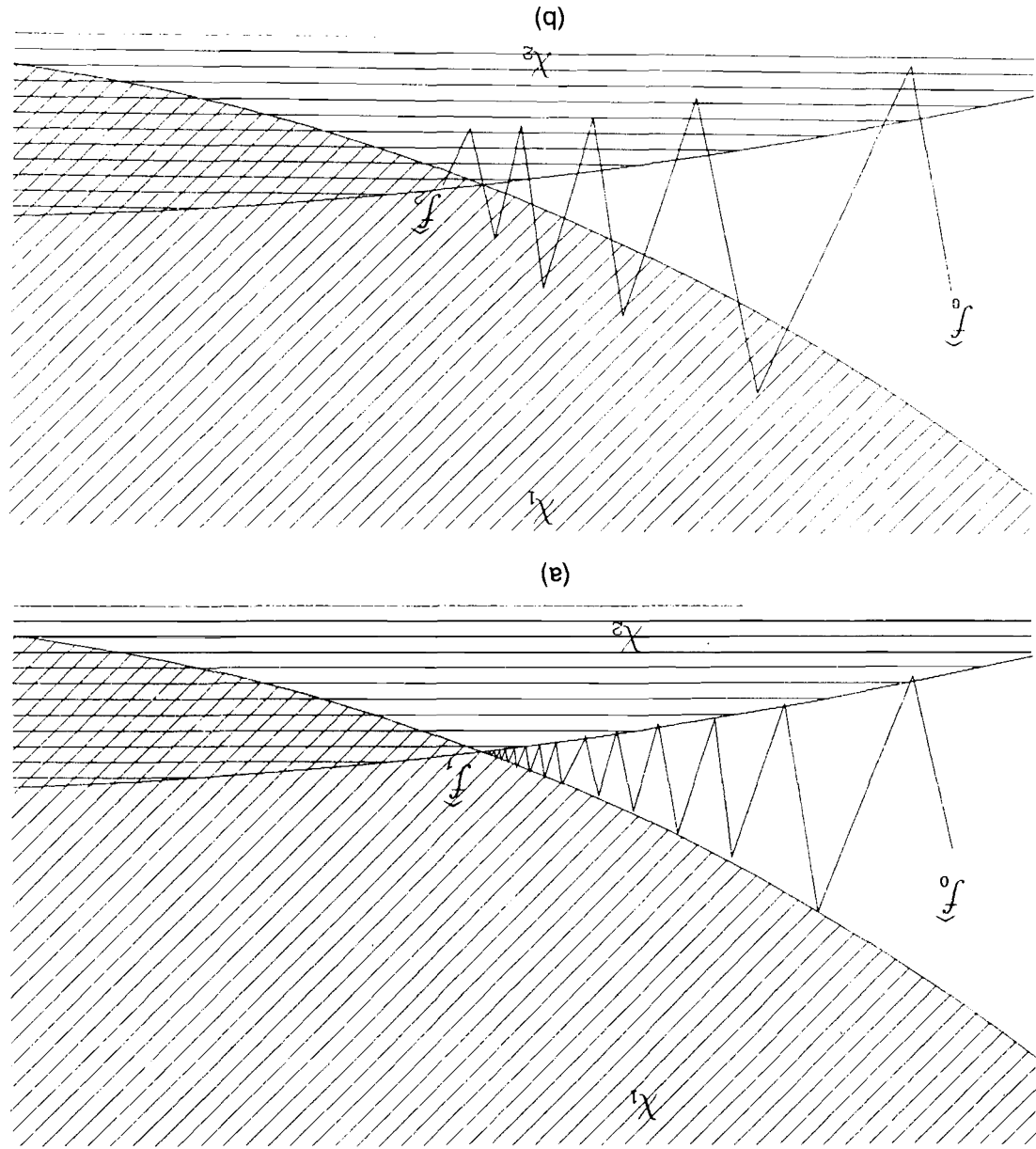


Fig.3.1. A geometrical illustration of the unrelaxed and relaxed projection operation. Initial estimate is same for both the illustrations. P_1 and P_2 are the projection operators. X_1 and X_2 are the convex sets.

(a) This figure illustrates the use of unrelaxed projection operators P_1 and P_2 . \hat{x} is the solution obtained. Note the slow convergence near the intersection of the two convex sets.

(b) This figure illustrates the use of relaxed projection operators P_1 and P_2 . Initial estimate and the convex sets are the same as in Fig.3.1a. \hat{x} is the solution obtained. Note the fast convergence near the intersection of the two convex sets.

$$\hat{\mathbf{f}}_k = T^k \hat{\mathbf{f}}_0, \quad k = 1, 2, 3, \dots \infty. \quad (3.21)$$

where $T (= T_m T_{m-1} T_{m-2} \dots T_1)$ is a composite operator composed of relaxed operators $\{T_i\}$. T_i 's are given by,

$$T_i = \mathbf{I} + \tau_i(P_i - \mathbf{I}), \quad i = 1, 2, 3, \dots, m \quad (3.22)$$

where τ_i 's are the relaxation parameters that control the rate of convergence, P_i 's are the projection operators and \mathbf{I} is the identity operator. The value of each relaxation parameter τ_i is set between 0 and 2 [Youla 82]. This relaxation extends the projection beyond the contour of the convex sets. τ_i 's can be adjusted for rapid convergence. This is illustrated geometrically in Fig.3.1b for a relaxed projection operator. If τ_i is set to unity, then (3.22) reduces to (3.21). It is shown that T_i 's are generally not projection operators but have the same fixed points as the P_i 's. Every fixed point of T_i is a feasible solution, i.e., a point in the intersection of the closed convex sets as shown in Fig.3.1.

Knowledge about the finite support of the object in the image plane and positivity are used as constraints in this thesis. Application of these constraints is equivalent to indirectly projecting the initial estimate onto the convex sets formed by these constraints. Though this method of POCS appears to be complicated, it is easy to implement it in practice. On application of positivity and finite support constraints, (3.17) becomes,

$$T \hat{\mathbf{f}}_k(x, y) = \begin{cases} \hat{\mathbf{f}}_k(x, y), & \text{for } x, y \in \Gamma \text{ and } \hat{\mathbf{f}}_k(x, y) \geq 0 \\ 0, & \text{otherwise} \end{cases} \quad (3.23)$$

where Γ is the support region, and

$$\hat{\mathbf{f}}_{k+1} = T \hat{\mathbf{f}}_k. \quad (3.24)$$

An image reconstructed using this method would have satisfied the requirement of smoothness, finite support and positivity constraints. Hereafter, we call the iteration in (3.24) as the method of TKM-POCS.

3.2 Convergence of the iterative regularized algorithm

In order to prove the convergence of this algorithm, properties of contraction and nonexpansive mappings can be used [Tom 81, Trussel 83]. We define some basic notations and terminology related to these mappings. The distance measure used in the following sections refer to the following metric:

$$d(x,y) = \|x - y\|. \quad (3.25)$$

Let us now define the concept of fixed points. Let a mapping Z from a subset of a metric space X onto X be represented as $Z : A \subset X \rightarrow X$. A fixed point of this mapping is a point $x^* \in A$ which is invariant under the mapping Z i.e., $Zx^* = x^*$. This fixed point is iteratively obtained as follows:

$$x_{k+1} = Zx_k = Z^k x_0, \quad (3.26)$$

where x_k is the k th approximation to x^* and x_0 is some initial estimate. This iteration converges to a fixed point only if the mapping Z is a contraction mapping.

Let A be a subset of a metric space X , and let Z be a mapping which maps A onto itself. Then Z is said to be a contraction mapping if there is a constant α ($0 \leq \alpha < 1$), such that for all $x, y \in A$, $d(Zx, Zy) \leq \alpha d(x, y)$.

If Z is a contraction mapping on a closed subset A of a complete metric space, then there is a unique fixed point for any initial estimate

$x \in A$. In many cases Z is not a contraction mapping but a nonexpansive mapping.

A mapping $Z: A \subset X \rightarrow X$ is said to be nonexpansive if $d(Zx, Zy) \leq d(x, y)$, for all $x, y \in A$ i.e., $\alpha = 1$. Unlike contraction, these mappings do not have a unique fixed point. The projection operator described in Section 3.1.2 is a nonexpansive mapping [Youla 82].

In order to show that the iteration (3.24) converges to a fixed point, it is necessary to show that $\mathfrak{S}(\hat{\mathbf{f}})$ is a contraction [Lagendijk 91], where,

$$\begin{aligned}\mathfrak{S}(\hat{\mathbf{f}}) &= \hat{\mathbf{f}} + \beta \left[(\mathbf{H}^T \mathbf{g}_s - (\mathbf{H}^T \mathbf{H} + \rho \mathbf{C}^T \mathbf{C}) \hat{\mathbf{f}}) \right] \\ &= \left[\mathbf{I} - \beta (\mathbf{H}^T \mathbf{H} + \rho \mathbf{C}^T \mathbf{C}) \right] \hat{\mathbf{f}} + \beta \mathbf{H}^T \mathbf{g}_s.\end{aligned}\quad (3.27)$$

We now find the distance measure between two images $\hat{\mathbf{f}}_1$ and $\hat{\mathbf{f}}_2$ using the metric defined in (3.25).

$$\begin{aligned}d(\mathfrak{S}(\hat{\mathbf{f}}_1), \mathfrak{S}(\hat{\mathbf{f}}_2)) &= || \left[\mathbf{I} - \beta (\mathbf{H}^T \mathbf{H} + \rho \mathbf{C}^T \mathbf{C}) \right] \hat{\mathbf{f}}_1 - \left[\mathbf{I} - \beta (\mathbf{H}^T \mathbf{H} + \rho \mathbf{C}^T \mathbf{C}) \right] \hat{\mathbf{f}}_2 || \\ &\leq || \mathbf{I} - \beta (\mathbf{H}^T \mathbf{H} + \rho \mathbf{C}^T \mathbf{C}) || || \hat{\mathbf{f}}_1 - \hat{\mathbf{f}}_2 || \leq \nu || \hat{\mathbf{f}}_1 - \hat{\mathbf{f}}_2 ||.\end{aligned}\quad (3.28)$$

where $\nu = || \mathbf{I} - \beta (\mathbf{H}^T \mathbf{H} + \rho \mathbf{C}^T \mathbf{C}) ||$. In order to prove that \mathfrak{S} is a contraction mapping, it is required to show that $0 \leq \nu < 1$. Since $(\mathbf{H}^T \mathbf{H} + \rho \mathbf{C}^T \mathbf{C})$ is a symmetric positive definite matrix, its eigenvalues ω_{ij} 's are real positive valued. Therefore, the following inequality holds good, if $\beta < 1$:

$$0 \leq || \mathbf{I} - \beta (\mathbf{H}^T \mathbf{H} + \rho \mathbf{C}^T \mathbf{C}) || < 1 \quad (3.29)$$

$$\text{or } 0 \leq \max_{ij} \{ |1 - \beta \omega_{ij}| \} < 1. \quad (3.30)$$

This method converges when β is small, in particular satisfying

$$0 < \beta < \frac{2}{\text{maximum eigenvalue of } ||\mathbf{I} - \beta(\mathbf{H}^T \mathbf{H} + \rho \mathbf{C}^T \mathbf{C})||}. \quad (3.31)$$

There exists schemes for finding optimal values for β [Biernacki 88]. Hence $\mathfrak{A}(\hat{\mathbf{f}})$ is a contraction mapping. Therefore the iteration (3.24) converges. In the following sections, we explore the suitability of this algorithm for image reconstruction from sparse data.

3.3 Image reconstruction from sparse data

The SAI setup used for simulation studies consists of an object plane of 128x128 points and a receiver plane of 128x128 points. Throughout the studies the frequency used for imaging operation corresponds to a wavelength λ of 0.25 units. The spacing between adjacent receiver elements is fixed at 0.5 units. The distance between the object and the receiver plane is kept at 2000 units. The receiver size in terms of the number of sensor elements is varied by selecting the points appropriately on the receiver array.

The sparse data is generated for different array sizes. The sparse data corresponding to $\kappa = 4, 16, \text{ and } 64$ are considered. The field data corresponding to the initial estimate of the image is generated. In order to improve the accuracy of the estimate, a method similar to the one described in the literature [Gerchberg 75] is used, where the known receiver data samples replace the corresponding estimated receiver data samples repeatedly in each iteration. The results obtained using the inverse filter,

the method of POCS, the method of TKM and the method of TKM-POCS are presented in the following sections. All the experiments assume that the original image function f is known

3.3.1 Inverse filtering

In this experiment, we use the inverse filtering for image reconstruction from sparse data. In inverse filtering, an image is reconstructed as follows:

$$\hat{F}(u,v) = \frac{G_s(u,v)}{H(u,v)} . \quad (3.32)$$

where $\hat{F}(\cdot)$, $G_s(\cdot)$ and $H(\cdot)$ are the 2-D FTs of the reconstructed image, the sparse data and the point spread function, respectively. \hat{f} is obtained by

$$\hat{f}(x,y) = IFT \left[\frac{G_s(u,v)}{H(u,v)} \right] . \quad (3.33)$$

Throughout this chapter we consider the smooth image shown in Fig.1.2a for simulation studies. Fig.3.2 shows the reconstructed images using inverse filtering. Figs.3.2a, 3.2b and 3.2c show, respectively, the reconstructed images when sparse data corresponding to $\kappa = 4, 16$, and 64 are used. Reconstructed images using this method are poorly resolved and noisy. Note that as the sparsity ratio increases, the quality of the reconstructed images become poorer.

3.3.2 Image reconstruction using the method of POCS

In order to improve the quality of the reconstructed image, knowledge about the finite support and positivity is incorporated in the reconstruction process using the method of POCS. Imposing these constraints onto the solution is equivalent to projecting an initial estimate \hat{f}_0 alternatively onto the convex

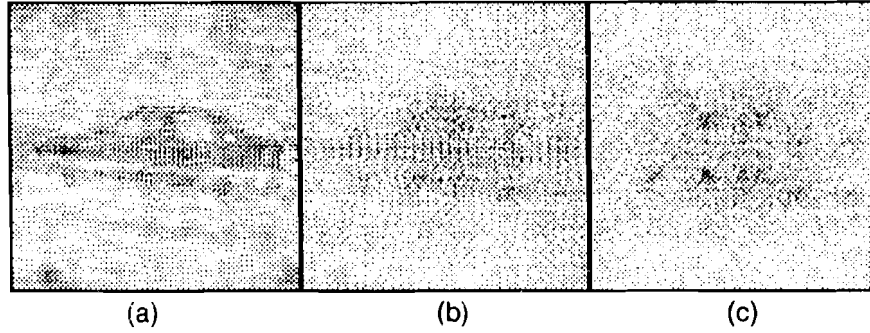


Fig.3.2. Image reconstruction using inverse filtering. This figure shows the images reconstructed using sparse data corresponding to (a) $\kappa = 4$, (b) $\kappa = 16$, and (c) $\kappa = 64$. Note the degradations in the reconstructed images as κ increases.

sets formed by them. At each iteration known values of the sparse data (g_i) replace the corresponding estimated receiver data values. The algorithm for image reconstruction from single frame of data using the method of POCS is given in Algorithm 3.1.

We now demonstrate the influence of these constraints on the quality of the reconstructed image. For sparse data corresponding to $\kappa = 4$, Figs.3.3a, 3.3b, and 3.3c represent images reconstructed using positivity constraint, finite support constraint, and both positivity and finite support constraints, respectively. It is interesting to note that incorporation of any one of the constraints has not improved the quality of the reconstructed image (see Figs.3.3a and 3.3b). But when both finite and positivity constraints were incorporated into the reconstruction algorithm, the quality of the reconstructed image has improved significantly. This is illustrated by the plot in Fig.3.3d. It is evident from the plot that error decreases rapidly as more constraints are incorporated into the reconstruction algorithm. This clearly indicates that knowledge about the object is essential in solving ill-posed problems. Fig.3.3e represents the image reconstructed using sparse data ($\kappa = 16$) by incorporating finite support and positivity

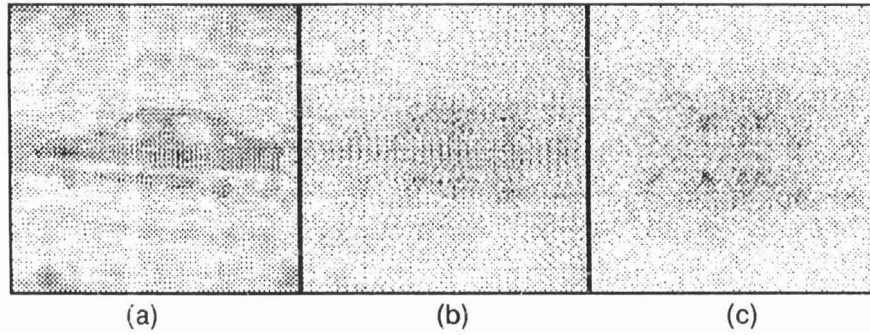


Fig.3.2. Image reconstruction using inverse filtering. This figure shows the images reconstructed using sparse data corresponding to (a) $\kappa = 4$, (b) $\kappa = 16$, and (c) $\kappa = 64$. Note the degradations in the reconstructed images as κ increases.

sets formed by them. At each iteration known values of the sparse data (g_i) replace the corresponding estimated receiver data values. The algorithm for image reconstruction from single frame of data using the method of POCS is given in Algorithm 3.1.

We now demonstrate the influence of these constraints on the quality of the reconstructed image. For sparse data corresponding to $\kappa = 4$, Figs.3.3a, 3.3b, and 3.3c represent images reconstructed using positivity constraint, finite support constraint, and both positivity and finite support constraints, respectively. It is interesting to note that incorporation of any one of the constraints has not improved the quality of the reconstructed image (see Figs.3.3a and 3.3b). But when both finite and positivity constraints were incorporated into the reconstruction algorithm, the quality of the reconstructed image has improved significantly. This is illustrated by the plot in Fig.3.3d. It is evident from the plot that error decreases rapidly as more constraints are incorporated into the reconstruction algorithm. This clearly indicates that knowledge about the object is essential in solving ill-posed problems. Fig.3.3e represents the image reconstructed using sparse data ($\kappa = 16$) by incorporating finite support and positivity

ALGORITHM 3.1 Image reconstruction from a single frame of data using the method of POCS.

1. Set $i = 1$. Let g_i be the measured sparse data. Let \hat{f}_i be the initial image.
2. Generate the field data corresponding to \hat{f}_i . $g = IFT[HF_i]$, where H and F_i are the FTs of h and \hat{f}_i , respectively.
3. Replace the calculated g with the measured field data g_i at known points to obtain the new g_{new} .
4. Reconstruct the image using deconvolution followed by the method of POCS.
 - (a) $G = FT[g_{\text{new}}]$
 - (b) $\hat{f}_i = IFT[H^{-1}G]$. This image has **728x728** points.
 - (c) $\hat{f}_{i+1} = I + \tau[P\hat{f}_i - I]$, where P is the projection onto the convex set formed by the finite support and positivity constraints, I is the identity operator and $\tau = 0.8$.

Here, $P\hat{f}_i = \begin{cases} \hat{f}_i, & \text{for } \hat{f}_i \in \Gamma \text{ and } \hat{f}_i > 0 \\ 0, & \text{otherwise} \end{cases}$
5. $i = i + 1$
6. Repeat step 2 through step 5 until an acceptable image is reconstructed.

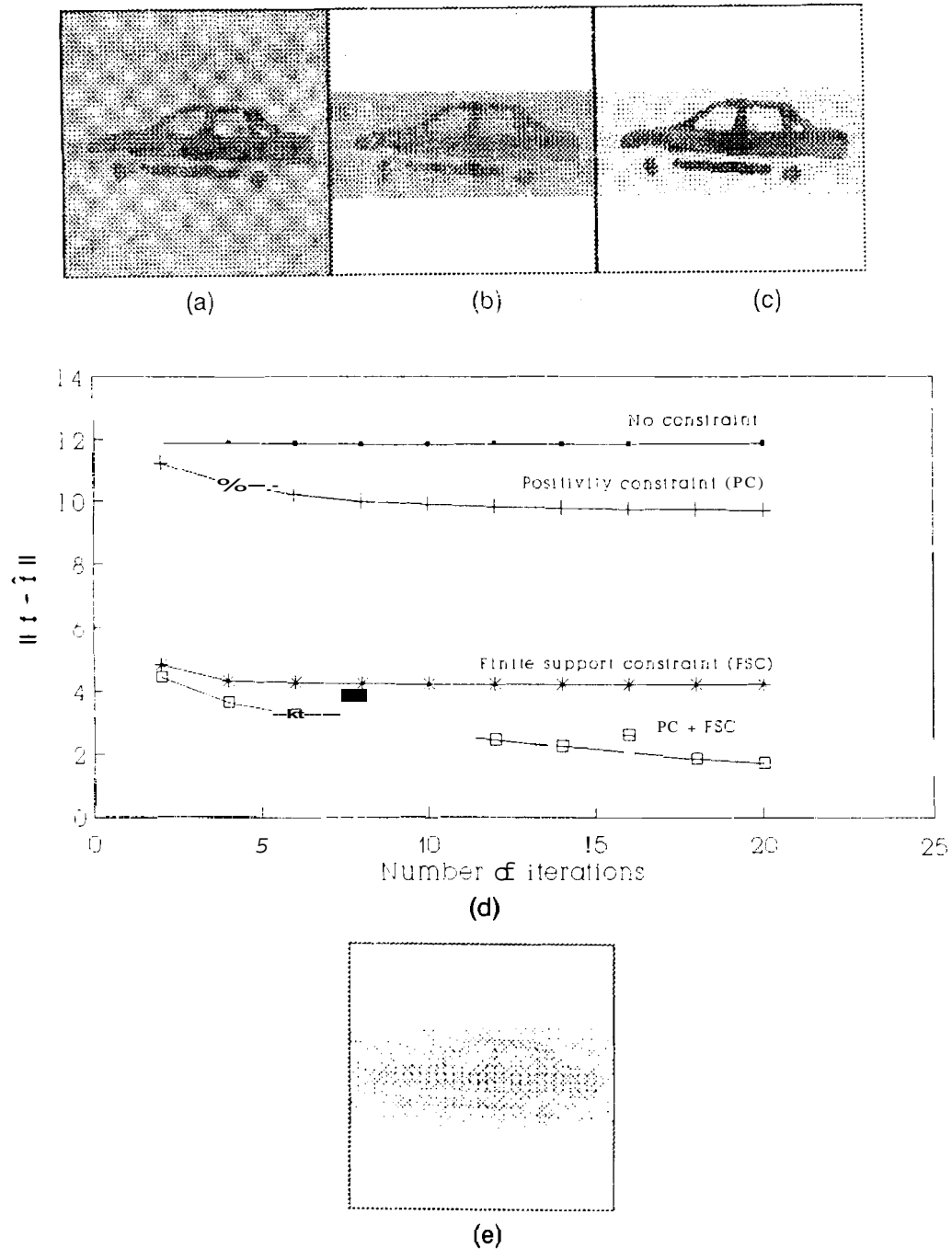


Fig.3.3. Illustration of the use of various constraints in the reconstruction process. This figure shows the images reconstructed using (a) positivity constraint, (b) finite support constraint, and (c) both finite support and positivity constraints. Sparse data corresponding to $a = 4$ was used for image reconstruction. Note the improvement in the quality when finite support and positivity constraints are incorporated into the reconstruction algorithm. (d) Illustration of the importance of constraints in improving the quality of the reconstructed image. (e) Image reconstruction using positivity and finite support constraint for $a = 16$.

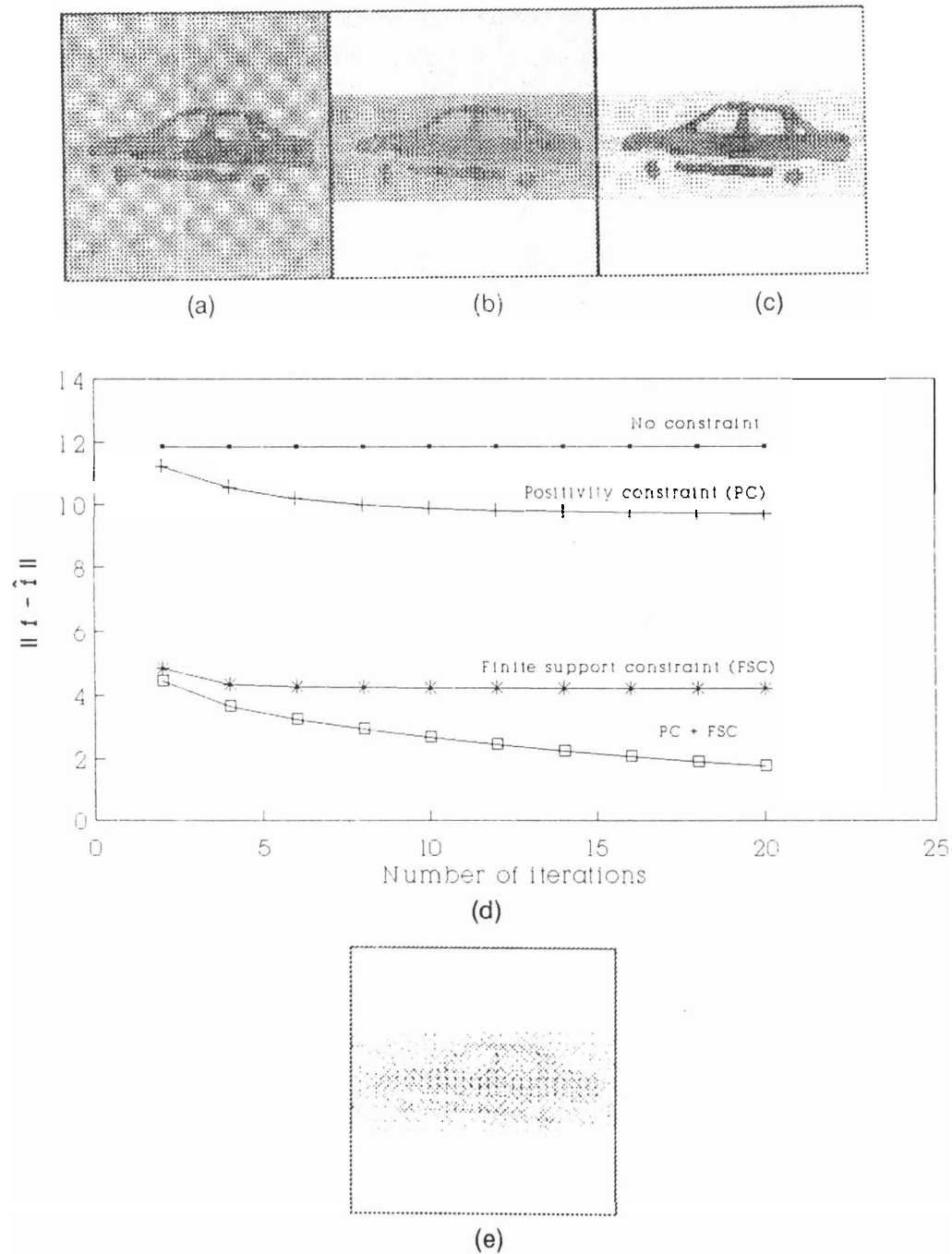


Fig.3.3. Illustration of the use of various constraints in the reconstruction process. This figure shows the images reconstructed using (a) positivity constraint, (b) finite support constraint, and (c) both finite support and positivity constraints. Sparse data corresponding to $\kappa = 4$ was used for image reconstruction. Note the improvement in the quality when finite support and positivity constraints are incorporated into the reconstruction algorithm. (d) Illustration of the importance of constraints in improving the quality of the reconstructed image. (e) Image reconstruction using positivity and finite support constraint for $\kappa = 16$.

constraints. The quality of the image is poor in spite of incorporating knowledge about the object. It demonstrates that as the sparsity ratio increases, positivity and finite support constraints are not sufficient to improve the quality of the reconstructed image. In the following section, we develop an algorithm based on the method of TKM regularization to demonstrate the importance of smoothness constraint in improving the quality of the reconstructed image.

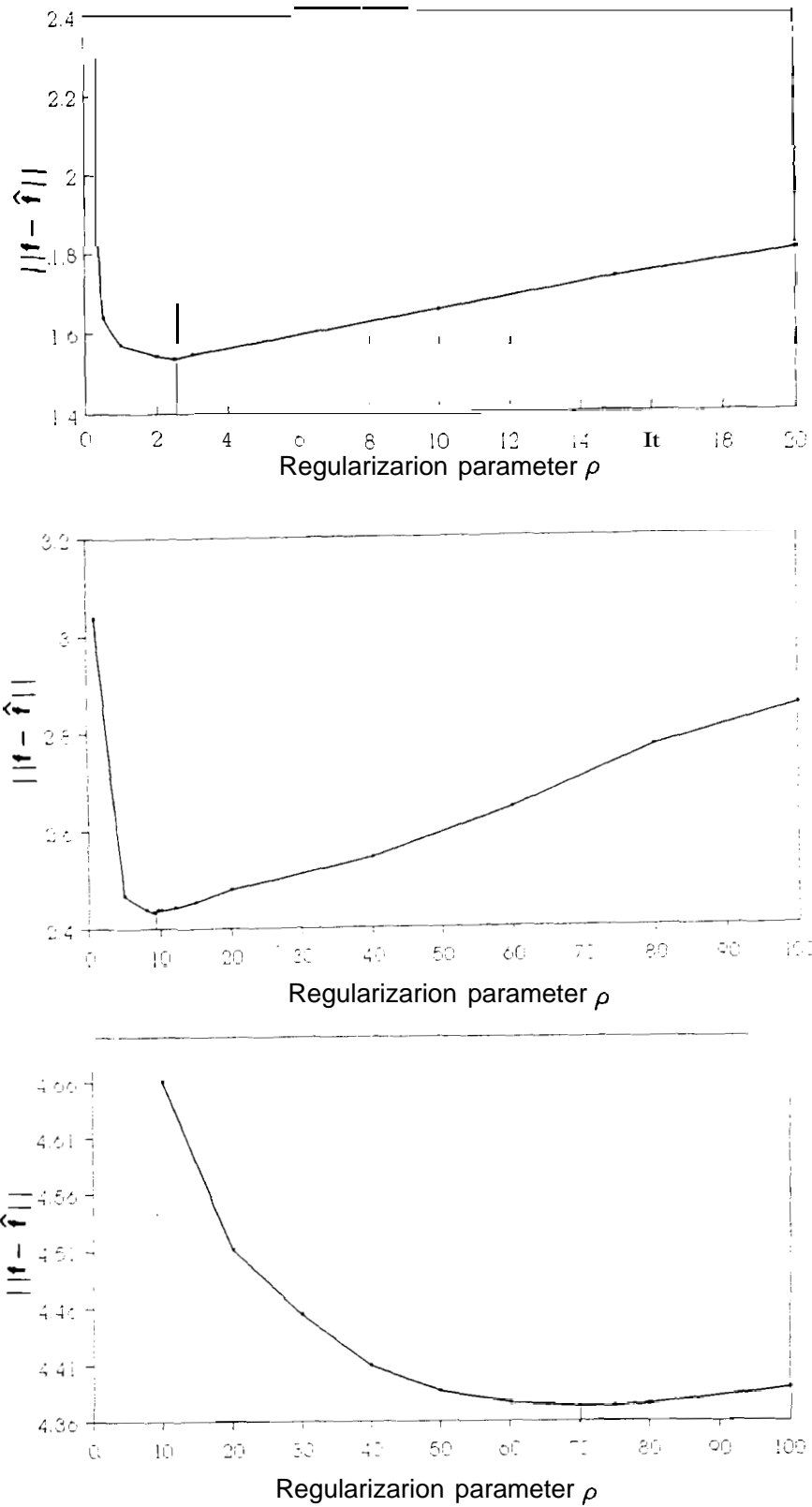
3.3.3 Image reconstruction using the method of Tikhonov-Miller regularization

The knowledge of smoothness of the image is incorporated into the reconstruction algorithm as a constraint. An image is reconstructed iteratively using (3.17). Image reconstruction procedure is terminated when an acceptable quality image is obtained. The algorithm for image reconstruction using the method of TKM regularization is given in Algorithm 3.2.

It has been stated earlier that the regularization parameter ρ controls the smoothness of the reconstructed image. We now study the effect of p on the reconstructed image. In all the experiments $\beta < 1$. Sparse data corresponding to $\kappa = 4, 16$ and 64 are generated. Regularization parameter is varied from 0.0001 to 100 . For every p value, the error $||f - \hat{f}||$ is calculated. The error as a function of the regularization parameter is plotted and is shown in Fig.3.4. The plots in Figs.3.4a, 3.4b, and 3.4c represent the influence of p on the reconstructed image for sparse data corresponding to $\kappa = 4, \kappa = 16$, and $\kappa = 64$, respectively. Note that in each of the plots the error decreases initially, reaches a minimum and then increases. It indicates that minimization of (3.5) depends on the value of p . Minimum of the function in (3.5) is obtained only for one value of p . Optimum value of the

Algorithm 3.2 **Image reconstruction from sparse data using TKM regularization method**

1. Set $i = 1$. Let g , be the measured sparse data. Let $\hat{\mathbf{f}}_i$ be the initial image.
2. Generate the field data g corresponding to $\hat{\mathbf{f}}_i$. $g = IFT[HF_i]$, where H and F_i are the FTs of h and $\hat{\mathbf{f}}_i$ respectively.
3. Replace the calculated g with the measured field data g , at known points to obtain the new g_{new} .
4. Reconstruct the image using TKM regularization
$$\hat{\mathbf{f}}_{i+1} = \hat{\mathbf{f}}_i + \beta \left[\mathbf{H}^T \mathbf{g}_{\text{new}} - (\mathbf{H}^T \mathbf{H} + \rho \mathbf{C}^T \mathbf{C}) \hat{\mathbf{f}}_i \right], \quad \beta = 0.1.$$
5. $i = i + 1$
6. Repeat step 2 through step 5 until an acceptable image is reconstructed.



• **Fig.3.4.** Selection of optimum regularization parameter ρ . These plots show the error $\|f - \hat{f}\|$ in the reconstruction as a function of the regularization parameter ρ for various sparsity ratios (a) $\kappa = 4$ and $\rho_{\text{opt}} = 2.5$, (b) $a = 16$ and $\rho_{\text{opt}} = 9.0$ and (c) $a = 64$ and $\rho_{\text{opt}} = 70.0$.

regularization parameter is selected when $\| \mathbf{f} - \hat{\mathbf{f}} \|$ is minimum. Optimum regularization parameter values for various sparsity ratios are given in Table 3.1. The value of the optimum ρ (ρ_{opt}) increases as the sparsity increases.

Table 3.1. Optimum regularization parameter values for various sparsity ratios

Sparsity ratio κ	ρ (optimum)
4	2.5
16	9.0
64	70.0

Now we demonstrate the influence of the regularization parameter on the quality of the reconstructed image. Sparse data corresponding to $\kappa = 16$ is used. The image in Fig.3.5a is reconstructed using $\rho = 0.0001$. The reconstructed image is dominated by noise and is similar to the reconstructed image using inverse filtering (Fig.3.2b). This is due to negligible smoothing. The image in Fig.3.5b is reconstructed using $\rho = 100$. Blurring in the reconstructed image indicates that the image is over smoothed. This clearly indicates that the value of ρ dictates the size of the smoothing window. The smoothing window used for reconstructing the image in Fig.3.5a is small whereas it is large for the reconstructed image shown in Fig.3.5b. Though the noise in Fig.3.5b is suppressed, the quality of the image is poor. The edges of the image are blurred. In order to strike a compromise, an optimum value ($\rho = 9.0$) is used for image reconstruction. Fig.3.5c represents the image reconstructed using the optimum ρ value. In this case the noise in the reconstructed image is reduced significantly and at the same time error due to regularization is also reduced.

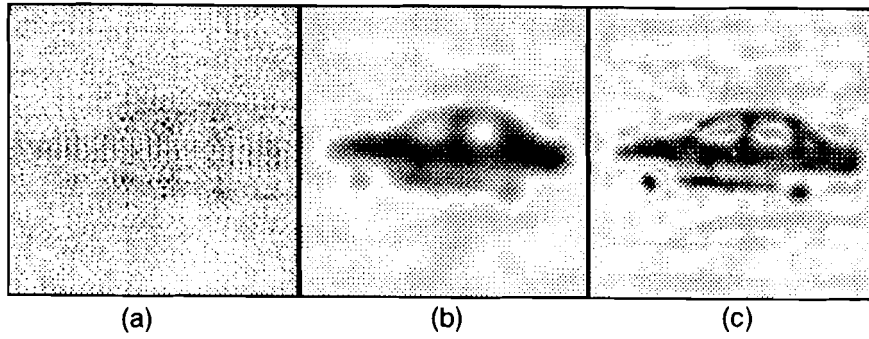


Fig.3.5. Influence of regularization parameter on the quality of the reconstructed images. Images are reconstructed using the method of TKM regularization. Sparse data corresponding to $a = 16$ is used for image reconstruction.

(a) This figure corresponds to negligible regularization ($\rho = 0.0001$). This image is similar to the image reconstructed using inverse filtering (See Fig. 3.2b).

(b) This figure shows the influence of the regularization parameter on the quality of the reconstructed image when $\rho = 100$. Noise is almost removed but the regularization error dominates the reconstructed image. Note the distortions near the edges of the image.

(c) This figure corresponds to the image reconstructed using the optimum regularization parameter ($\rho = 9.0$).

We now study the performance of this method for sparse data corresponding to various values of sparsity ratio. Figs.3.6a, 3.6b, and 3.6c represent the images reconstructed for sparse data corresponding to $\kappa = 4, 16$ and 64 , respectively. Optimum regularization values from Fig.3.4 were used for image reconstruction. The quality of the reconstructed image

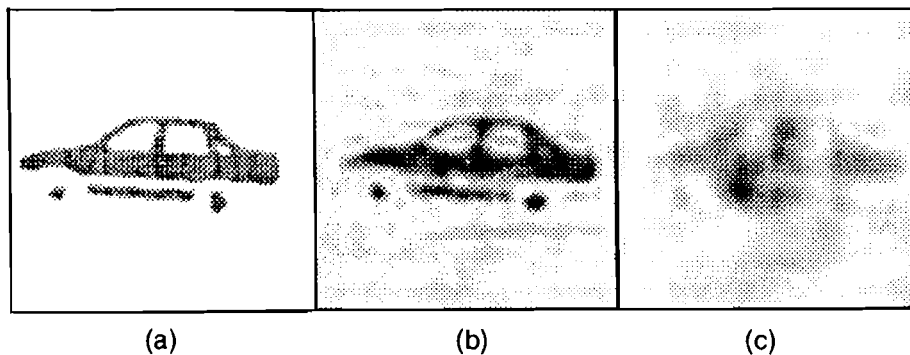


Fig.3.6. Image reconstruction using the method of TKM regularization. Optimum regularization parameters from plots in Fig. 3.4 were used for image reconstruction. This figure shows the images reconstructed using the sparse data corresponding to (a) $\kappa = 4$, (b) $\kappa = 16$, and (c) $\kappa = 64$.

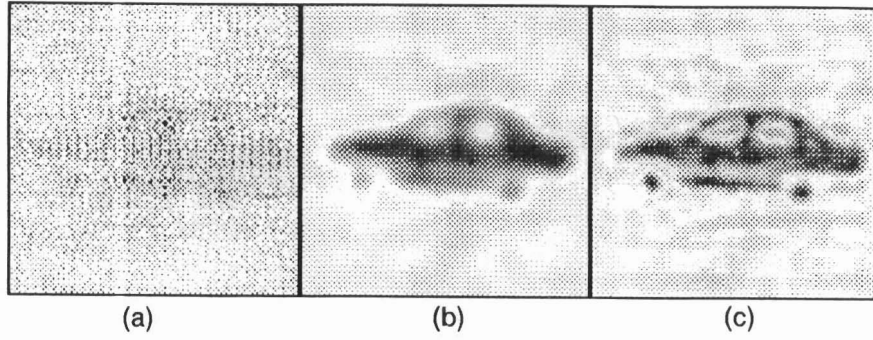


Fig.3.5. Influence of regularization parameter on the quality of the reconstructed images. Images are reconstructed using the method of TKM regularization. Sparse data corresponding to $\kappa = 16$ is used for image reconstruction.

(a) This figure corresponds to negligible regularization ($\rho = 0.0001$). This image is similar to the image reconstructed using inverse filtering (See Fig. 3.2b).

(b) This figure shows the influence of the regularization parameter on the quality of the reconstructed image when $\rho = 100$. Noise is almost removed but the regularization error dominates the reconstructed image. Note the distortions near the edges of the image.

(c) This figure corresponds to the image reconstructed using the optimum regularization parameter ($\rho = 9.0$).

We now study the performance of this method for sparse data corresponding to various values of sparsity ratio. Figs.3.6a, 3.6b, and 3.6c represent the images reconstructed for sparse data corresponding to $\kappa = 4, 16$ and 64 , respectively. Optimum regularization values from Fig.3.4 were used for image reconstruction. The quality of the reconstructed image

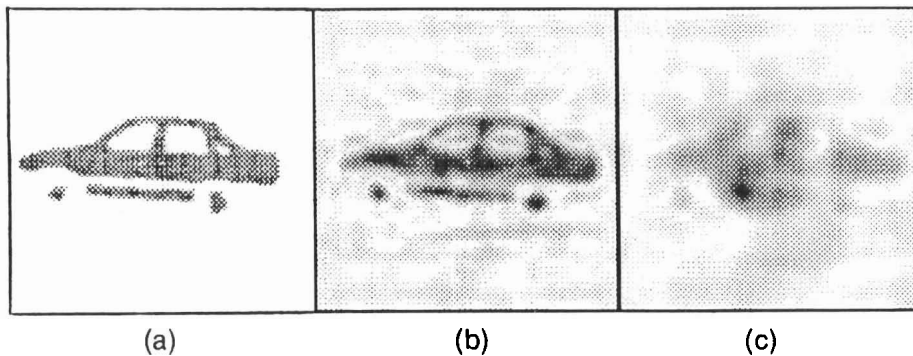


Fig.3.6. Image reconstruction using the method of TKM regularization. Optimum regularization parameters from plots in Fig. 3.4 were used for image reconstruction. This figure shows the images reconstructed using the sparse data corresponding to (a) $\kappa = 4$, (b) $\kappa = 16$, and (c) $\kappa = 64$.

is poor for $\kappa = 64$ (Fig.3.6c). Though the noise is reduced significantly there is also loss of information in the reconstructed image. This is due to the missing information in the receiver data.

3.3.4 *Image reconstruction* using the method of TKM-POCS

In order to incorporate the smoothness, finite support and positivity constraints, we develop an algorithm based on (3.24). Optimum regularization parameters obtained from Fig.3.4 were used for image reconstruction. This algorithm is terminated after obtaining an image with improved quality. The algorithm for image reconstruction using the method of TKM-POCS is given in Algorithm 3.3.

We now study the performance of this method for sparse data corresponding to various values of sparsity ratio. Figs.3.7a, 3.7b, and 3.7c show the images reconstructed from sparse data corresponding to $\kappa = 4, 16$ and 64 respectively. There is a significant improvement in the quality of the images over the corresponding images shown in Fig.3.6. It is evident from the images shown in Fig.3.7 that the quality of the images is improved when more number of constraints are incorporated in the reconstruction algorithm. The reconstruction error is plotted as a function of number of iterations in Fig.3.8. Note that in all the cases, the reconstruction error decreases.

In order to demonstrate the effectiveness of this method in obtaining a smooth solution, the intensity plot corresponding to the 61st scan line of the images in Figs.1.1a, 3.3e and 3.7b are shown in Fig.3.9. It can be seen from the plot that the image reconstructed using the iterative method of POCS is noisy and not smooth. On the other hand, the image obtained

Algorithm 3.3 Image reconstruction using the the method of TKM-POCS.

1. Set $i = 1$. Let g_i be the measured sparse data. Let $\hat{\mathbf{f}}_i$ be the initial image.
2. Compute the field data corresponding to $\hat{\mathbf{f}}_i$. $g = IFT[\mathbf{H}\mathbf{F}_i]$, where H and \mathbf{F}_i are the FT of h and $\hat{\mathbf{f}}_i$, respectively.
3. Replace the calculated g with the measured field data g_i at known points to obtain the new \mathbf{g}_{new} .

4. Reconstruct the image using TKM regularization

$$\hat{\mathbf{f}}_{i+1} = P \left\{ \hat{\mathbf{f}}_i + \beta \left[\mathbf{H}^T \mathbf{g}_{\text{new}} - (\mathbf{H}^T \mathbf{H} + \rho \mathbf{C}^T \mathbf{C}) \hat{\mathbf{f}}_i \right] \right\} \quad \beta = 0.1.$$

where P is the relaxed projection operator projecting onto the convex set formed by the finite support constraint and positivity constraint, I is the identity operator and $\tau = 0.8$

$$\text{Here } P \hat{\mathbf{f}}_i = \begin{cases} \hat{\mathbf{f}}_i & \text{for } \hat{\mathbf{f}}_i \in \Gamma \text{ and } \hat{\mathbf{f}}_i > 0 \\ 0 & \text{otherwise} \end{cases}$$

5. $i = i + 1$
6. Repeat step 2 through step 5 until an acceptable quality image is reconstructed.

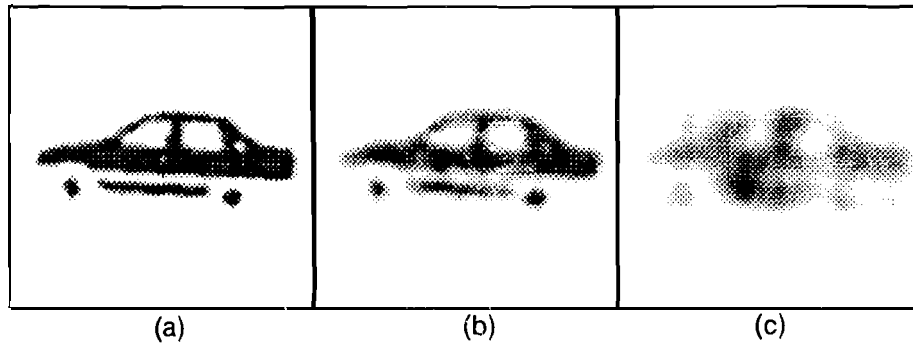


Fig.3.7. Image reconstruction using the method of TKM-POCS. The optimum regularization parameters found using plots in Fig. 3.5 were used for image reconstruction. This figure shows the images reconstructed using sparse data corresponding to (a) $\kappa = 4$, (b) $\kappa = 16$, and (c) $\kappa = 64$. Note the improvement in the reconstructed images over the corresponding images reconstructed using inverse filtering, the method of POCS and TKM regularization.

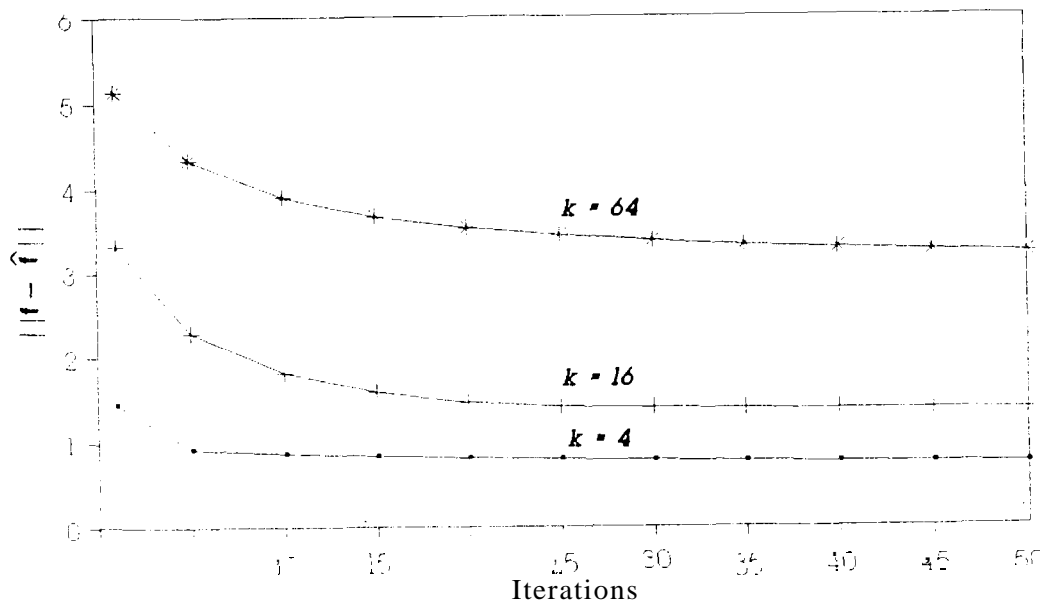


Fig.3.8. The regularization error versus the iteration number for various sparsity ratios. The quantitative improvement in the reconstructed images in terms of the error $\|f - \hat{f}\|$ as a function of number of iterations for the images in Fig.3.7 is shown.

from the method of TKM-POCS is smoother than the images reconstructed using inverse filtering and the method of POCS. The resultant I-D signal is closer to the original. Fig.3.10 shows the relative performance of the three methods. For all sparsity ratios, TKM-POCS method has the smallest error. In order to illustrate the error in the reconstruction, an error image is obtained by considering the difference between the original image shown

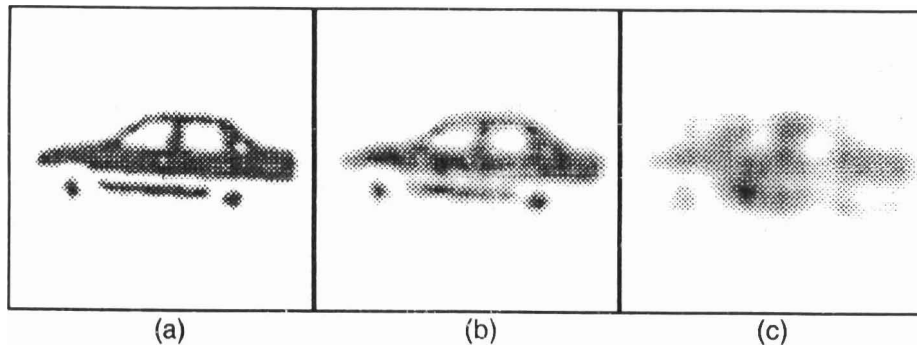


Fig.3.7. Image reconstruction using the method of TKM-POCS. The optimum regularization parameters found using plots in Fig. 3.5 were used for image reconstruction. This figure shows the images reconstructed using sparse data corresponding to (a) $\kappa = 4$, (b) $\kappa = 16$, and (c) $\kappa = 64$. Note the improvement in the reconstructed images over the corresponding images reconstructed using inverse filtering, the method of POCS and TKM regularization.

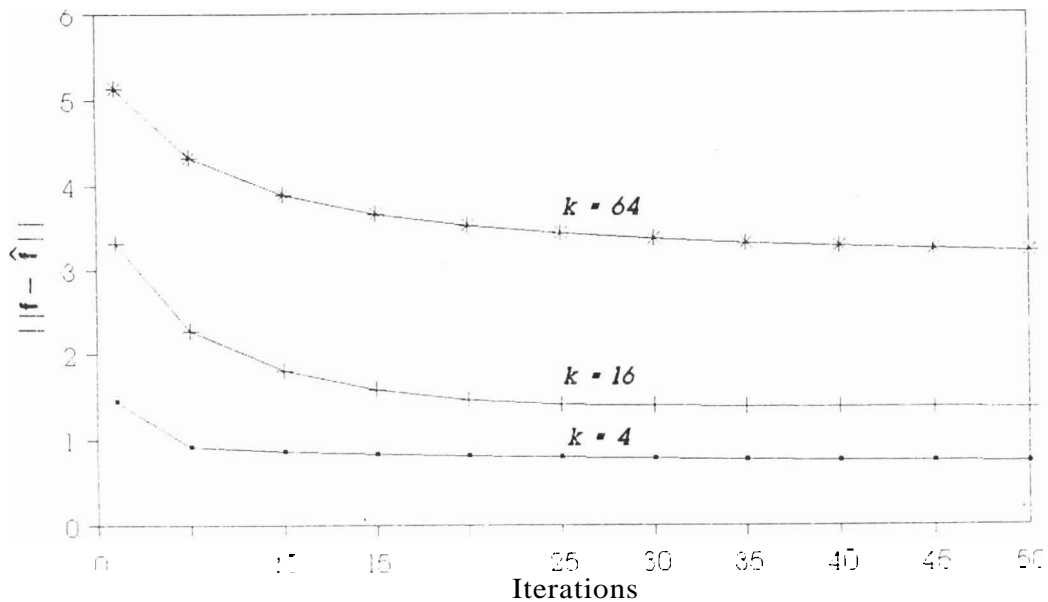


Fig.3.8. The regularization error versus the iteration number for various sparsity ratios. The quantitative improvement in the reconstructed images in terms of the error $\|f - \hat{f}\|$ as a function of number of iterations for the images in Fig.3.7 is shown.

from the method of TKM-POCS is smoother than the images reconstructed using inverse filtering and the method of POCS. The resultant 1-D signal is closer to the original. Fig.3.10 shows the relative performance of the three methods. For all sparsity ratios, TKM-POCS method has the smallest error. In order to illustrate the error in the reconstruction, an error image is obtained by considering the difference between the original image shown

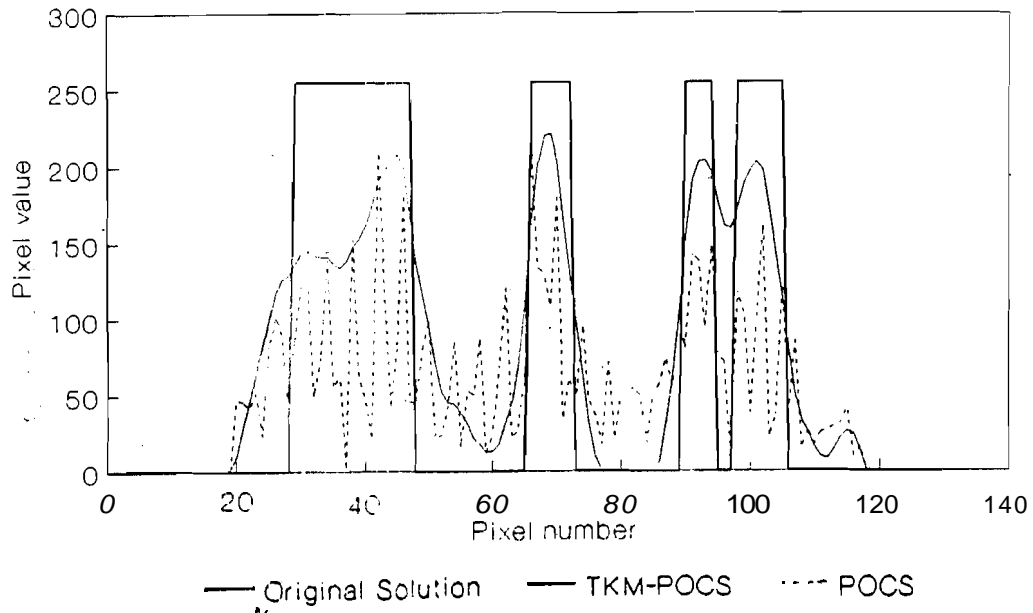


Fig.3.9. Illustration of smooth reconstruction in 1-D. This figure shows the effectiveness of the TKM-POCS in obtaining a smooth solution. 128 values corresponding to the Gist scan line from images in Figs.1.2a, 3.4e and 3.7b are plotted.

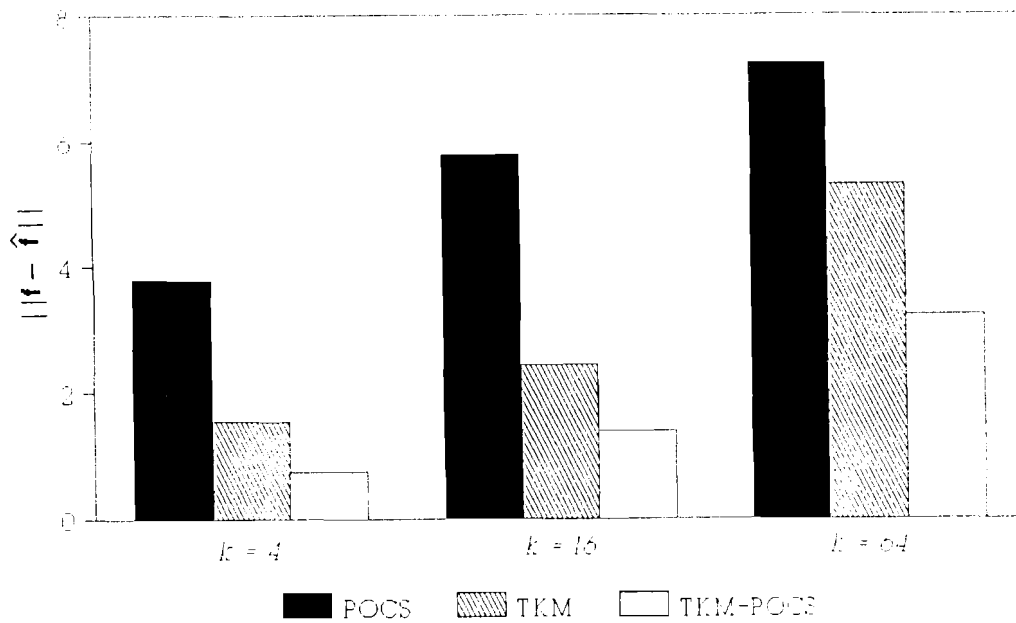


Fig.3.10. Comparison of performance of three methods of image reconstruction from sparse data.

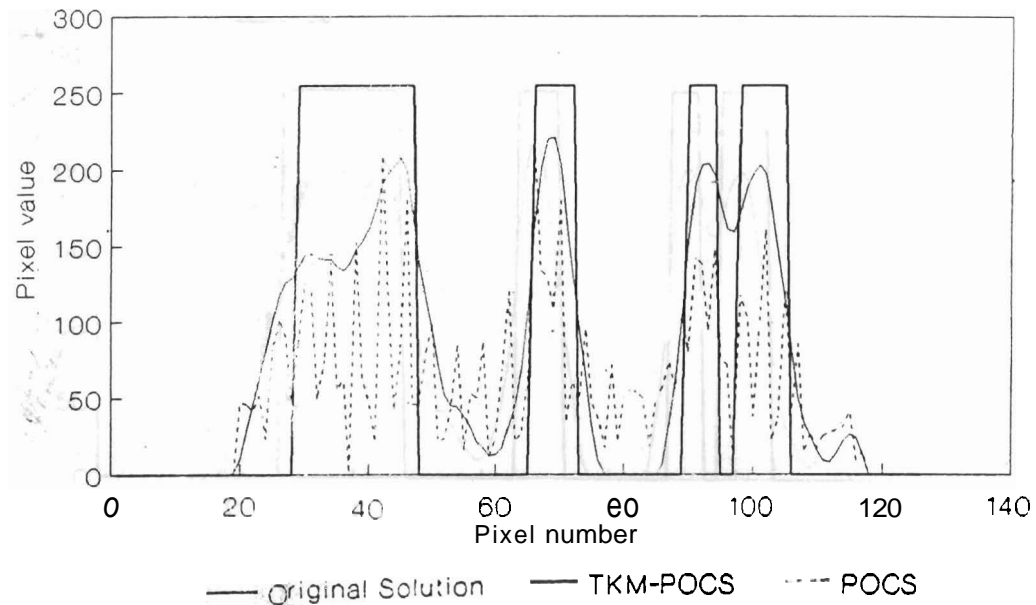


Fig.3.9. Illustration of smooth reconsriution in 1-D. This figure shows the effectiveness of the TKM-POCS in obtaining a smooth solution. 128 values corresponding to the 61st scan line from images in Figs.1.2a, 3.4e and 3.7b are plotted.

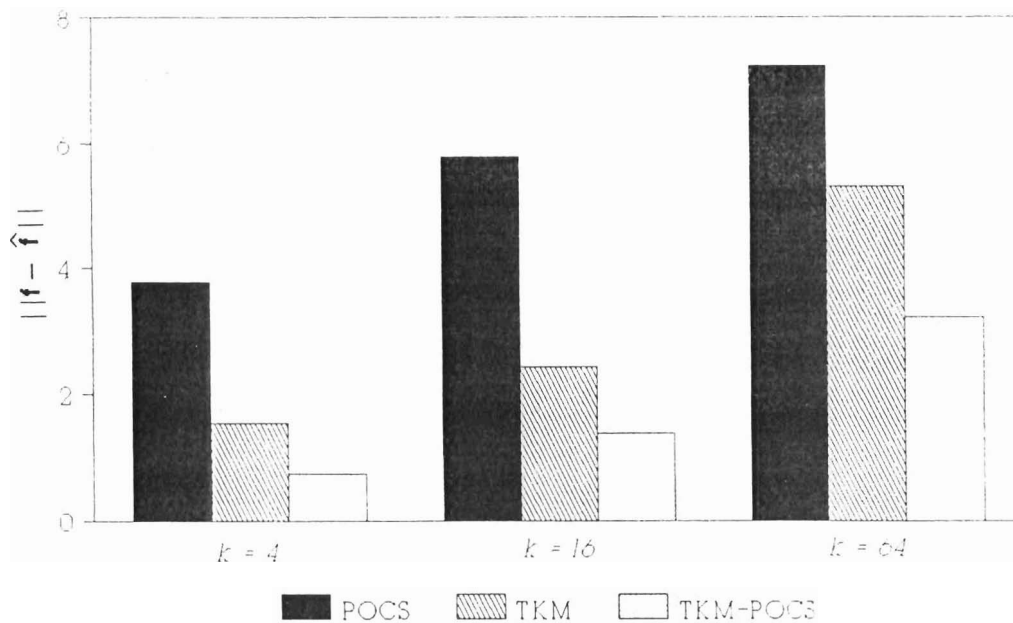


Fig.3.10. Comparison of performance of three methods of image reconstruction from sparse data.

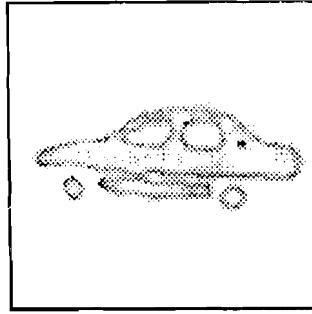


Fig.3.11. Illustration of the error in the reconstructed image .due to regularization. This figure shows the difference image between the original image shown in Fig.1.2a and the image shown in Fig.3.7. This figure shows clearly that the error due to regularization is present near the edges and not in the smooth region of the image.

in Fig.1.2a and the reconstructed image shown in Fig.3.7b. The error image in Fig.3.11 shows that the regularization error is dominant only near the edges of the image, while the error in the smooth region is negligible. The results demonstrate the importance of constraints in obtaining an improved quality image.

3.4 Image reconstruction from noisy sparse data

We have so far demonstrated the use of three methods of image reconstruction from noise free sparse data. Degradation in the reconstructed images is mainly due to the missing information in the receiver data. We now study the influence of noise in the sparse data, and compare the performance of these methods. Gaussian noise with zero mean is added to the sparse data. Sparse data corresponding to $\kappa = 16$ is generated. Three frames of sensor data are obtained by adding noise with SNRs 5 dB, 0dB and -5dB to the sparse data. Fig.3.12 shows the images reconstructed using inverse filtering, the method of POCS and the method of TKM-POCS. Inverse filtering and the method of POCS do not use any

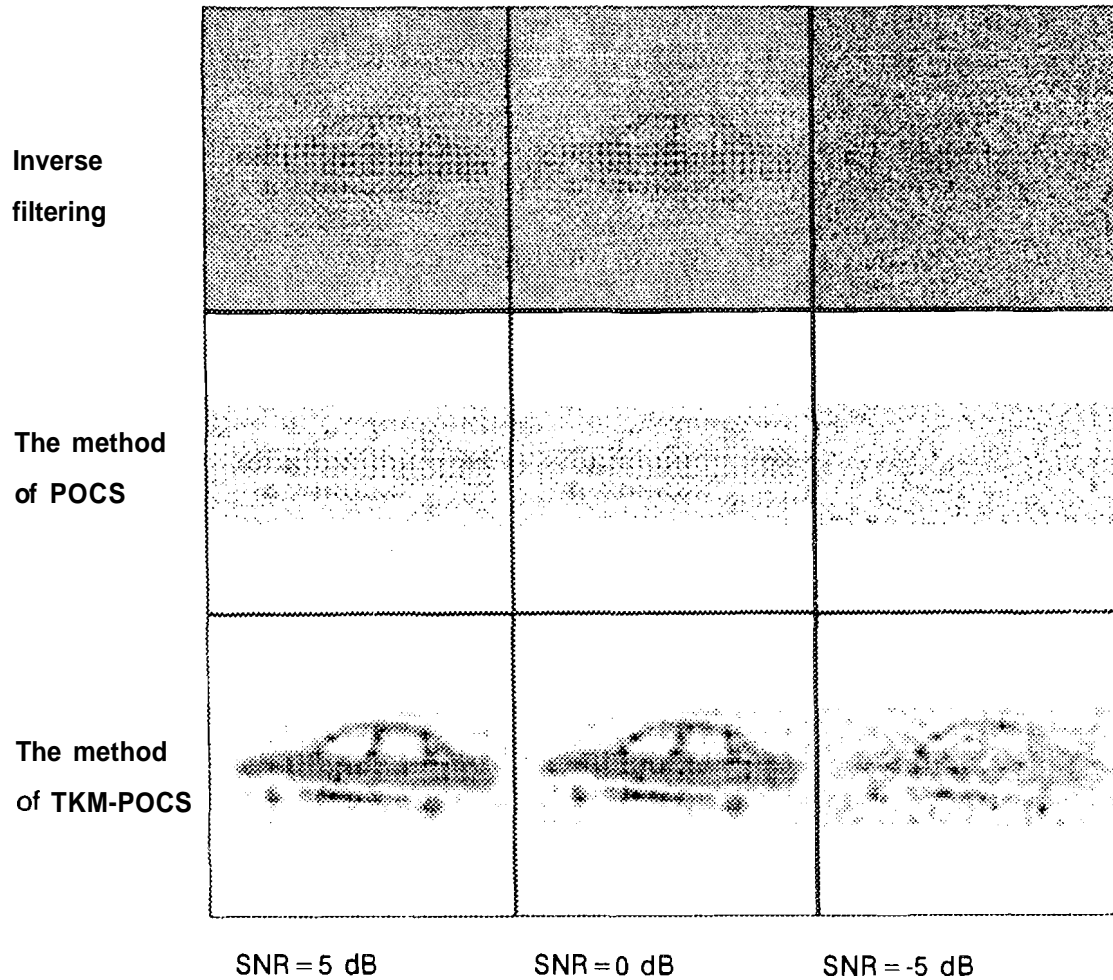


Fig.3.12. Image reconstruction from sparse and noisy data. Sparse data ($\kappa = 16$) is corrupted with Gaussian noise with zero mean. This figure shows the images reconstructed using inverse filtering, the method of POCS and the method of TKM-POCS.

knowledge about the noise statistics. As expected the quality of the reconstructed images is poor for low SNRs (first two rows of Fig.3.12). On the other hand, the quality of the reconstructed images from TKM-POCS (third row) is better. This is due to the well known noise removal property of the TKM regularization method. We have demonstrated that TKM-POCS method can be used for sparse and noisy data cases as well.

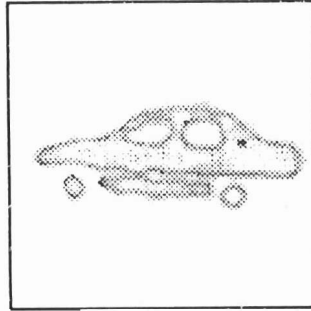


Fig.3.11. Illustration of the error in the reconstructed image due to regularization. This figure shows the difference image between the original image shown in Fig.1.2a and the image shown in Fig.3.7. This figure shows clearly that the error due to regularization is present near the edges and not in the smooth region of the image.

in Fig.1.2a and the reconstructed image shown in Fig.3.7b. The error image in Fig.3.11 shows that the regularization error is dominant only near the edges of the image, while the error in the smooth region is negligible. The results demonstrate the importance of constraints in obtaining an improved quality image.

3.4 Image reconstruction from noisy sparse data

We have so far demonstrated the use of three methods of image reconstruction from noise free sparse data. Degradation in the reconstructed images is mainly due to the missing information in the receiver data. We now study the influence of noise in the sparse data, and compare the performance of these methods. Gaussian noise with zero mean is added to the sparse data. Sparse data corresponding to $\kappa = 16$ is generated. Three frames of sensor data are obtained by adding noise with SNRs 5 dB, 0dB and -5dB to the sparse data. Fig.3.12 shows the images reconstructed using inverse filtering, the method of POCS and the method of TKM-POCS. Inverse filtering and the method of POCS do not use any

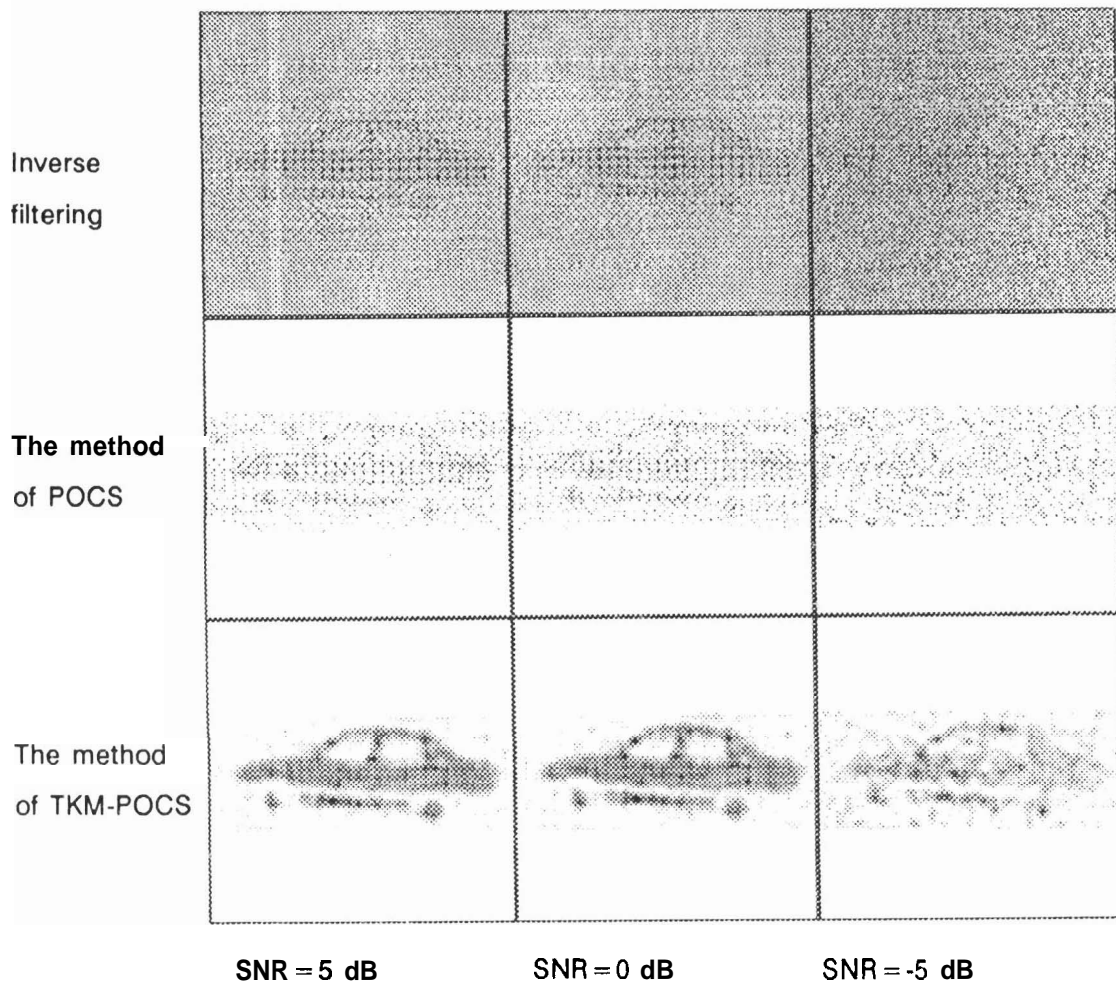


Fig.3.12. Image reconstruction from sparse and noisy data. Sparse data ($\kappa = 16$) is corrupted with Gaussian noise with zero mean. This figure shows the images reconstructed using inverse filtering, the method of POCS and the method of TKM-POCS.

knowledge about the noise statistics. As expected the quality of the reconstructed images is poor for low SNRs (first two rows of Fig.3.12). On the other hand, the quality of the reconstructed images from TKM-POCS (third row) is better. This is due to the well known noise removal property of the TKM regularization method. We have demonstrated that TKM-POCS method can be used for sparse and noisy data cases as well.

3.5 Quality of image reconstruction

The performance of the reconstruction algorithm is usually measured using mean squared error (MSE) criterion. MSE criterion may give an improved SNR value for the resultant image, but the image may not be good visually [Zhou 88]. In other words, the human visual system does not use MSE criterion for quality measurement. Methods using the properties of the human visual system have been reported [Anderson 76, Katsaggelos 91]. The properties of the human visual system has been included into the restoration algorithm to obtain visually optimum results [Katsaggelos 91].

In this section, we propose a quality measure using the recognition accuracy of a trained artificial neural network (ANN). A feedforward network trained using the backpropagation algorithm [Lippmann 87] for a given set of images shown in Fig.1.3 is used for object recognition. The reconstructed noisy images are converted to binary images and presented to the neural network. Table 3.2 lists the classification accuracy for various reconstruction algorithms. In this table recognition accuracy of the neural network is listed for various sparsity ratios and for various methods. The number of images

Table 3.2 Classification accuracy of the ANN

Sparsity ratio κ	Classification accuracy					
	Total number of images = 28					
	Inverse Filtering		Method of POCS		TKM-POCS	
	noise-free data	noisy data	noise-free data	noisy data	noise-free data	noisy data
4	28	28	28	28	28	28
16	20	17	23	20	28	27
64	12	10	19	16	22	18

trained using the network is **28**. For $\kappa = 4$, all the reconstructed images have been recognized accurately, for both noise free and noisy cases. The number in each column gives indirectly the measure of the quality of images reconstructed. As the sparsity increases, the classification accuracy of the network decreases. From the table it is clear that the classification accuracy is higher for the method of TKM-POCS than the other two methods. This indirectly indicates that the images reconstructed using TKM-POCS are better in quality.

3.6 Summary

In this chapter we have demonstrated the use of the well known method of TKM regularization for image reconstruction from sparse and noisy data. We have demonstrated through simulation studies the effect of the regularization parameter on the quality of the reconstructed images. Optimum regularization parameter values have been found for various sparsity ratios. It was found that regularization parameter was proportional to the sparsity ratio.

We have proposed an iterative method (TKM-POCS) based on the methods of TKM regularization and POCS. In this iterative method smoothness, finite support and positivity constraints are incorporated into the reconstruction algorithm. The repeated inclusion of known data and the knowledge about the object have improved the quality of the reconstructed image at each iteration. The results of the TKM- POCS method have shown that the quality of the reconstructed images is significantly better than the quality of the images reconstructed using inverse filtering, the iterative

method of POCS, and TKM regularization. The quality of the reconstructed images are measured using a trained neural network.

Though the proposed iterative method is useful in reducing the effect of noise and in extracting available information, it cannot provide new information if it is not originally present. The reconstructed images have errors near the edges of the images. The performance of this algorithm is poor when noise is also present in the data. In the following chapter, we discuss image reconstruction methods from multiple frames of sparse and noisy data together with the knowledge in the form of constraints on the object in the image.

IMAGE RECONSTRUCTION FROM MULTIPLE FRAMES OF DATA - STATIC SITUATION

In Chapter 3, we have investigated the effects of various types of constraints on the quality of the reconstructed image. We have developed algorithms to reconstruct images from a single frame of data by incorporating finite support, smoothness and positivity constraints in the reconstruction process. As the complexity of the problem increases in terms of sparsity, noise and complexity of object shapes, quality of the reconstructed image becomes poor. The purpose of this chapter is to demonstrate that images with improved quality can be obtained when multiple frames of sparse data are available. Multiple frames of data may be obtained in a static or dynamic SAI situation. Throughout this chapter multiple frames of data refer to the data collection in a static SAI situation. In a static SAI situation, object remains stationary during the imaging process.

4.1 **Need** for additional information

As we have mentioned in the introductory chapter that image reconstruction from sparse data is an ill-posed problem because the available information is not sufficient to reconstruct images of acceptable quality. In this context, we have shown in Chapter 3 that regularization theory is a tool to extract available information. However, it can provide only an effective solution to

reduce the effects of sparsity and noise, but it cannot provide new information if it is not available.

In practice, one may be able to obtain several frames of sparse data for a given SAI setup. This additional data may be combined appropriately to improve the quality of the reconstructed image further [Yegnanarayana 89]. The redundant information available from multiple frames of sparse data may reduce the effects of errors in the measured data. It is important to note that in multiple frames of sparse data, each frame of data must provide some additional information about the object. In the following sections, we discuss various approaches to collect multiple frames of data, and discuss methods to combine them to obtain an image with improved quality.

4.2 Sources of multiple frames of data

In many practical applications, such as multispectral satellite imagery, medical imaging, dynamic scene situation, color imaging, etc., multiple frames of data of the object being imaged can be collected. Color images are the common source for most of the multiframe methods discussed in the literature. The imaging system measures the same scene using three different wavelengths. In multispectral satellite imagery, same scene is imaged using multiple spectral window. For example, LANDSAT imagery consists of four digital images of the same scene, two images in the visible region of the spectrum and the other two in the infrared region. Additional frames, multiples of four, can be obtained if the same scene is imaged on a different day.

In SAI situations multiple frames of data can be collected by several ways: (a) varying the frequency of the incident radiation and collecting sparse data at each frequency, (b) varying the distance between the object and the receiver and collecting sparse data at each distance, and (c) varying the distance between the object and the receiver and collecting multiple frequency data at each location of the receiver. In multiple frequency approach [Mariadossou 90], a set of sensor array data collected at several frequencies is used for image reconstruction. In this situation, data is collected by transmitting the incident wave at each frequency separately and then measuring the reflected field at the receiver.

In this study, we propose two other approaches to collect multiple frames of sparse data. In the first approach, we generate multiple frames of sparse data by altering the distance between the object and the receiver. The receiver array is moved along the axis perpendicular to the object and the receiver planes, and the sparse data is collected at each location of the receiver array. In the second approach, sparse data from multiple frequencies and multiple locations are combined. In this method, the distance between the object and the receiver is varied and for each case a set of multiple frequency data is collected. Our objective is to develop algorithms to combine all the frames of sparse data, and thus to overcome the limitations of sparsity and noise.

4.3 Multiple frame image formation model

In this section, we describe a multiframe image formation model. Let $\underline{\mathbf{M}} = \{ \underline{\mathbf{H}}, \underline{\mathbf{g}}, \underline{\mathbf{f}}, \underline{\mathbf{n}} \}$ represent the multiframe static imaging model with K frames, $K \geq 1$. Here $\underline{\mathbf{H}} \{ \mathbf{H}_1, \mathbf{H}_2, \mathbf{H}_3, \dots, \mathbf{H}_K \}$ represents a set of transformation

matrices, $\underline{\mathbf{g}}_s = \{\mathbf{g}_{s1}, \mathbf{g}_{s2}, \mathbf{g}_{s3}, \dots, \mathbf{g}_{sK}\}$ represents a set of sparse sensor array data vectors, $\underline{\mathbf{f}} = \{\mathbf{f}_1, \mathbf{f}_2, \mathbf{f}_3, \dots, \mathbf{f}_K\}$ represents a set of original image vectors and $\underline{\mathbf{n}} = \{\mathbf{n}_1, \mathbf{n}_2, \mathbf{n}_3, \dots, \mathbf{n}_K\}$ represents a set of statistically independent noise vectors. in a static imaging situation, all the elements in the set $\underline{\mathbf{f}}$ will have the same value, as the object remains stationary in its position during imaging. Each element in the sets $\underline{\mathbf{g}}_s$, $\underline{\mathbf{f}}$ and $\underline{\mathbf{n}}$ is a vector and is of size $M^2 \times 1$. Each element of $\underline{\mathbf{H}}$ is a matrix of size $M^2 \times M^2$. The multiframe imaging system model is similar to the single frame imaging model and is given by

$$\underline{\mathbf{g}}_s = \underline{\mathbf{H}} \underline{\mathbf{f}} + \underline{\mathbf{n}}, \quad (4.1)$$

where $\underline{\mathbf{g}}_s$, $\underline{\mathbf{f}}$ and $\underline{\mathbf{n}}$ are obtained by stacking K frames of data \mathbf{g}_{sk} , K images \mathbf{f}_k , and K noise vectors \mathbf{n}_k as follows:

$$\underline{\mathbf{g}}_s = \begin{bmatrix} \mathbf{g}_{s1} \\ \mathbf{g}_{s2} \\ \vdots \\ \mathbf{g}_{sK} \end{bmatrix} \quad \underline{\mathbf{f}} = \begin{bmatrix} \mathbf{f}_1 \\ \mathbf{f}_2 \\ \vdots \\ \mathbf{f}_K \end{bmatrix} \quad \underline{\mathbf{n}} = \begin{bmatrix} \mathbf{n}_1 \\ \mathbf{n}_2 \\ \vdots \\ \mathbf{n}_K \end{bmatrix}. \quad (4.2)$$

The matrix $\underline{\mathbf{H}}$ in this model is written as

$$\underline{\mathbf{H}} = \begin{bmatrix} \mathbf{H}_1 & \mathbf{0} & \mathbf{0} & \dots & \mathbf{0} \\ \mathbf{0} & \mathbf{H}_2 & \mathbf{0} & \dots & \mathbf{0} \\ \mathbf{0} & \mathbf{0} & \mathbf{H}_3 & \dots & \mathbf{0} \\ \vdots & \vdots & \vdots & \ddots & \vdots \\ \mathbf{0} & \mathbf{0} & \mathbf{0} & \dots & \mathbf{H}_K \end{bmatrix} \quad (4.3)$$

Here $\mathbf{0}$ is a matrix of size $M^2 \times M^2$ with all elements 0. \mathbf{H}_k is a matrix of size $M^2 \times M^2$, elements of which are generated from impulse response of the

imaging model. The size of \mathbf{H} is $KM^2 \times KM^2$. As each element of \mathbf{H} is considered to be different, all the elements in the set \mathbf{g}_s are different.

A solution to (4.1) is similar to the solution obtained for (3.1) and it is given by

$$\hat{\mathbf{f}} = \left(\mathbf{H}^T \mathbf{H} + \rho \mathbf{C}^T \mathbf{C} \right)^{-1} \mathbf{H}^T \mathbf{g}_s \quad (4.4)$$

where $\hat{\mathbf{f}}$ is the set of solution vectors and \mathbf{C} is the set of regularization operators $(\mathbf{C}_1, \mathbf{C}_2, \mathbf{C}_3, \dots, \mathbf{C}_K)$. All the elements of \mathbf{C} are chosen to be the same $(\mathbf{C} = \mathbf{C}_1 = \mathbf{C}_2 = \mathbf{C}_3 = \dots = \mathbf{C}_K)$, as all the frames of sparse data represent the same object. The inversion in (4.4) can be solved iteratively using the method of steepest descent as shown in Chapter 3. The iterative method will be similar to the one obtained for single frame imaging model and is given by

$$\hat{\mathbf{f}}_{j+1} = \hat{\mathbf{f}}_j + \beta \left[\mathbf{H}^T \mathbf{g}_s - \left(\mathbf{H}^T \mathbf{H} + \rho \mathbf{C}^T \mathbf{C} \right) \hat{\mathbf{f}}_j \right] \quad j = 1, 2, 3, \dots, \infty \quad (4.5)$$

The sizes of the matrices involved in this iterative method are large $(KM^2 \times KM^2)$. For example if the number of frames is 10, and the size of the image is 128x128, then the dimension of each term in the square bracket is 163840x163840. In the next section, we propose another method for combining multiple frames of sparse data, where stacking the multiple frames one below the other is avoided.

4.4 An iterative method for image reconstruction from multiple frames of sparse data

The method described in the previous section is not suitable when large number of frames are needed to reconstruct an image. Therefore we follow

an alternate approach in which the dimensions of the matrices do not increase with the increase in the number of frames used for image reconstruction.

We collect multiple frames of sparse data by altering the distance between the object and the receiver by a known amount. The imaging setup for collecting multiple frames of data is shown in Fig.4.1. We first describe a general method for combining multiple frames of sparse data and later develop specific algorithms based on the methods of POCS and TUFA-POCS.

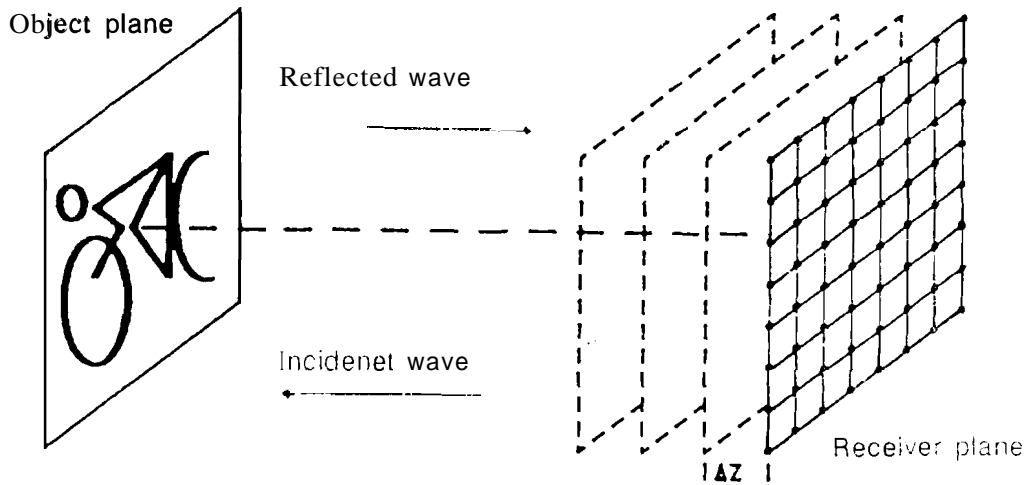


Fig.4.1. Illustration of the movement of the receiver array along the axis

Let us denote the sparse data measured at distance z_i by $g_s(z_i)$. Now the imaging model can be written as

$$g_s(z_i) = h(z_i) * f, \quad (4.6)$$

where $g_s(z_i)$ is the sparse data, $h(z_i)$ is the impulse response of the system when the distance between the object and receiver is z_i , and f is the image of the stationary object. Taking FT on both sides,

$$G_s(z_i) = H(z_i)F, \quad (4.7)$$

where $G_s(z_i)$, $H(z_i)$, and F are the FTs of $g_s(z_i)$, $h(z_i)$ and f , respectively. We can reconstruct the image \hat{f} by

$$\hat{f} = IFT \left[H^{-1}(z_i)G_s(z_i) \right]. \quad (4.8)$$

So far, steps (4.6 to 4.8) for image reconstruction are same as for the single frame image reconstruction methods. Now we compute the receiver data $g_c(z_{i+1})$ of the $(i+1)th$ frame from \hat{f} , as $H(z_{i+1})$ is known.

$$g_c(z_{i+1}) = IFT \left[\left(H(z_{i+1})\hat{F} \right) \right], \quad (4.9)$$

where \hat{F} is the FT of \hat{f} . The dimension of $g_c(z_{i+1})$ is same as the dimension of \hat{f} . Measured values $g_s(z_{i+1})$ replace the values of $g_c(z_{i+1})$ at the known points on the receiver.

$$g_n(z_{i+1}) = g_c(z_{i+1}) \downarrow g_s(z_{i+1}) \quad (4.10)$$

where \downarrow is the replacement operation. The new data $g_n(z_{i+1})$ contains information not only about the i th frame but also about the $(i+1)th$ frame. Receiver data in (4.10) can now be used to reconstruct a better estimate of the image. This process may be continued until all the frames are combined. It can be iterated until an image with acceptable quality is reconstructed. The advantage of this method is that the size of the matrices used for computation remains the same irrespective of the number of frames used for image reconstruction. Therefore the complexity in terms of the

computation and memory requirement does not increase as in (4.5). The complexity of computation increases only by K times the single frame case.

In Chapter 3, we have shown that the method of POCS can be used to find a solution from a feasible solution set. In single frame model, initial estimate is sequentially projected onto the convex sets which are formed by the constraints, and this process is iterated until an acceptable solution is obtained. In image reconstruction from multiple frames of sparse data, additional K convex sets are formed apart from the convex sets formed by the known constraints for every iteration.

Let \mathcal{X}_k be the solution set obtained for the k th frame by the intersection of all convex sets formed by the known constraints. \mathcal{X}_k is also a convex set. Let \mathcal{X} be the feasible solution set obtained by intersection of all \mathcal{X}_k ($\mathcal{X} = \bigcap_k \mathcal{X}_k$). Any solution in this set is acceptable provided $\mathcal{X} \neq \varphi$. Every reconstructed image in this feasible solution set has not only satisfied the constraints posed on it but also has obtained information from all the other frames, and hence it will have an improved quality.

A set theoretic estimate can be found by the following iterative process:

$$\hat{\mathbf{f}}_{i+1} = P_m P_{m-1} P_{m-2} \dots \hat{\mathbf{f}}_0 = P^i \hat{\mathbf{f}}_0, \quad j = 0, 1, 2, \dots, \infty \quad (4.11)$$

where m is the number of convex sets, P^i is the projection onto the convex set \mathcal{X}_k , and $\hat{\mathbf{f}}_0$ is the initial estimate. Information content in the reconstructed image will be improved by combining multiple frames of data through this sequential projection method. An iterative algorithm based on the method of POCS for image reconstruction from multiple frames of sparse data is given in Algorithm 4.1.

4.5 Image reconstruction from multiple frames of data using TKM-POCS method

If a priori knowledge about smoothness of the object is available, then it can also be incorporated along with the finite support and positivity constraints using the method of TKM-POCS discussed in Chapter 3. Let $\hat{\mathbf{f}}_{j+1}^i$ be the reconstructed image at $(j+1)$ th iteration from the sparse data \mathbf{g}_{j+1} using the method of TKM-POCS. From (3.24), one can write,

$$\hat{\mathbf{f}}_{j+1}^i = T \left\{ \hat{\mathbf{f}}_j^i + \beta \left[\mathbf{H}^T(\eta_i) \mathbf{g}_s - (\mathbf{H}^T(\eta_i) \mathbf{H}(\eta_i) + \rho \mathbf{C}^T \mathbf{C}) \hat{\mathbf{f}}_j^i \right] \right\} \quad j = 1, 2, 3, \dots, \infty. \quad (4.12)$$

Here η represents either z or λ . Using this reconstructed image, receiver data for the frame corresponding to the next frame can be computed. The data generation and image reconstruction process can be iterated until an image with acceptable quality is reconstructed. In this way, one can incorporate all the three constraints (positivity, finite support and smoothness constraints) and combine all the frames of data. An algorithm based on TKM-POCS method is given in Algorithm 4.2.

4.6 Sparse data collection by varying system model parameters(z and A)

In this section, we discuss another method to collect multiple frames of sparse data by varying both the object-receiver distance (z) and the wavelength (A) of the incident radiation. The receiver array is moved away from or towards the object and at each distance multiple frequency data is collected. The imaging model is written as:

$$\mathbf{g}(z_j, \lambda_i) = \mathbf{h}(z_j, \lambda_i) * \mathbf{f}, \quad i = 1, N \text{ and } j = 1, M. \quad (4.13)$$

Algorithm 4.1. *Image reconstruction from multiple frames of sparse data using the method of POCS*

1. K = Number of frames, $i = 0$. z_i is the distance between the object and the receiver. $g_s(z_i)$ is the sparse data of the i th frame measured at z_i . For multifrequency approach, $g_s(\lambda_i)$ is the sparse data of the i th frame measured at frequency corresponding to λ_i . In order to generalize this algorithm, we use a symbol η to represent either z or λ . Let \hat{f}_i be the initial estimate of the image.
2. Compute $(i+1)$ th receiver data

$$g_c(\eta_{i+1}) = IFT \left[\left(H(\eta_{i+1}) \hat{F}_i \right) \right]$$
3. Replace $g_c(\eta_{i+1})$ with known values of $g_s(\eta_{i+1})$

$$g_{new}(\eta_{i+1}) = g_c(\eta_{i+1}) \downarrow g_s(\eta_{i+1})$$
4. Compute the image as follows:
 Take FT of $g_{new}(\eta_{i+1})$.

$$G_{new}(\eta_{i+1}) = H(\eta_{i+1}) \hat{F}_i$$

$$\hat{f}_{i+1} = IFT \left[H^{-1}(\eta_{i+1}) G_{new}(\eta_{i+1}) \right]$$
5. Project this estimate onto the convex sets formed by the finite support and positivity constraints.

$$P \hat{f}_{i+1} = \begin{cases} \hat{f}_{i+1}, & \text{for } (x,y) \in \Gamma, \text{ where } \Gamma \text{ is the support region} \\ 0, & \text{otherwise} \end{cases}$$
6. $i = i + 1$. If $i > K$, $i = 1$.
7. Repeat step 2 through 6 until an acceptable quality image is reconstructed.

Algorithm 4.2. Image reconstruction from multiple frames of sparse data using the method of TKM-POCS.

1. $K =$ Number of frames, $i = 0$. z_i is the distance between the object and the receiver. $g_s(z_i)$ is the sparse data of the i th frame measured at z_i . For multifrequency approach, $g_s(\lambda_i)$ is the sparse data of the i th frame measured at frequency corresponding to λ_i . In order to generalize this algorithm, we use a symbol η to represent either z or λ . Let $\hat{\mathbf{f}}_i$ be the initial estimate of the image.
2. Compute the receiver data

$$\mathbf{g}_c(\eta_{i+1}) = \text{IFT} \left[\left(H(\eta_{i+1}) \hat{\mathbf{f}}_i \right) \right]$$
3. Replace $\mathbf{g}_c(\eta_{i+1})$ with known values of $\mathbf{g}_s(\eta_{i+1})$

$$\mathbf{g}_{\text{new}}(\eta_{i+1}) = \mathbf{g}_c(\eta_{i+1}) \downarrow \mathbf{g}_s(\eta_{i+1})$$
4. Reconstruct the image using TKM-POCS method .

$$\hat{\mathbf{f}}_{j+1}^i = T \left\{ \hat{\mathbf{f}}_{j+1}^i + \beta \left[H^T(\eta_{i+1}) \mathbf{g}_{\text{new}} - (H^T(\eta_{i+1}) H(\eta_{i+1}) + \rho C^T C) \hat{\mathbf{f}}_{j+1}^i \right] \right\}$$

$$j = 1, 2, 3, \dots, \infty$$

where T is the relaxed projection operator projecting onto the convex set formed by the finite support constraint and positivity constraint, $\beta = 0.8$ and $\rho = 0.6$.

$$T \hat{\mathbf{f}}_{j+1}^i = \begin{cases} \hat{\mathbf{f}}_{j+1}^i, & \text{for } (x, y) \in \Gamma, \text{ where } \Gamma \text{ is the support region} \\ 0, & \text{otherwise} \end{cases}$$
5. $i = i + 1$. If $i > K$, $i = 1$.
6. Repeat step 2 through 5 until an acceptable quality image is reconstructed.

Here N is the number of frequencies used to collect multiple frames of data at each location of the receiver array. M is the number of positions where the receiver array is placed to collect multiple frequency data. $g_s(z_j, \lambda_i)$ is the sparse data collected at z_j using wavelength λ_i . Algorithms based on the methods of POCS and TKM-POCS can be developed for this case also.

4.7 Experimental Studies

The SAI simulation setup used for experimental studies consists of an object plane with 128×128 points and a receiver plane of 128×128 points. The spacing between receiver points is fixed at 0.5 units. The frequency of the transmitted wave and the distance between the object and the receiver are varied. The receiver size in terms of the number of sensor elements is varied by selecting the points appropriately on the receiver array. Sparse data corresponding to $\kappa = 4, 16$ and 64 are generated for simulation studies. We consider here three approaches for collecting multiple frames of sparse data.

In the first approach, multiple frames of data are collected by varying the frequency of the transmitted wave. In this case the value of λ is varied within the range from 0.25 units to 0.32 units. For each receiver array size, the data is collected using 1, 2, 4, and 8 frequencies. The distance between the receiver and the object plane is kept at 2000 units.

In the second approach, multiple frames of data are collected by varying the distance between the receiver and the object plane. The value of A is 0.25 units. The data is collected using different locations (1, 2, 4, and 8) of the receiver array. The variation of the distance of the receiver array is varied between two limits ($z = 2000$ units and $z = 1900$ units). For each

receiver array size, multiple frames of data are collected by varying the location of the receiver array.

In the third approach, multiple frames of data are collected by varying both the frequency and the location of the receiver array. The variation of z is fixed between two limits as in the second case. The data at each location is collected for two frequencies ($\lambda = 0.25$ units, and $\lambda = 0.32$ units). This is repeated for several receiver array sizes and locations.

4.8 Results and discussions

Algorithms 4.1 and 4.2 are used for image reconstruction from multiple frames of sparse data. For a given computational complexity (fixed number of iterations), the quality of the reconstructed image improves with the increase in number of frequencies as seen column wise (top to bottom) in Fig.4.2. We also notice that as the number of receiving elements is decreased, the quality degrades as seen row wise (left to right). As the number of frames used for reconstruction is increased, there is an improvement in the reconstructed image (along the column). These results suggest that whenever it is possible to collect multiple frequency data, the receiver complexity in terms of the number of receiver elements can be significantly reduced.

When there is a possibility of collecting data at different known locations by the same array, the quality of the reconstructed image can be improved by using the multiple frames of data. The methods of POCS and TKM-POCS are used to combine multiple frames of sparse data. The results are shown in Figs.4.3 and 4.4 for a single frequency. Here also as the number of frames increases, the quality of the reconstructed image

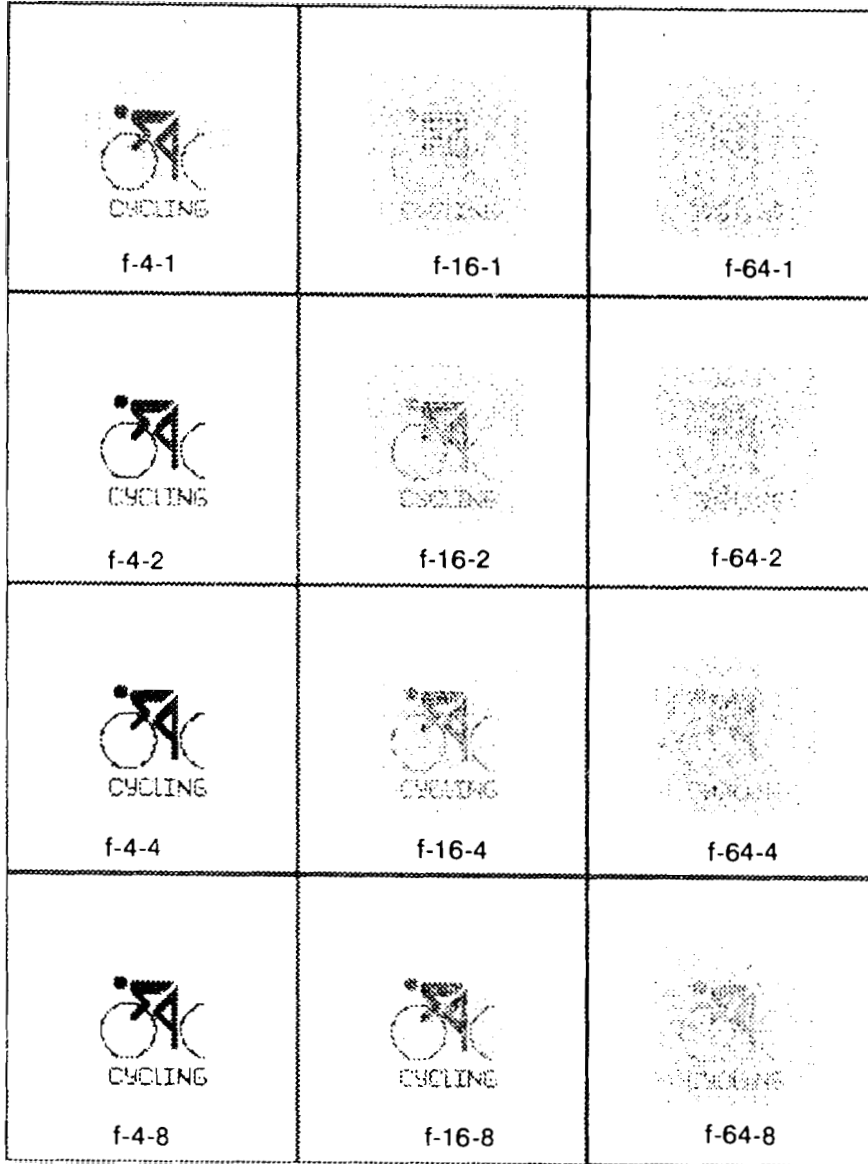


Fig.4.2. Image reconstruction from multiple frames of sparse data using the method of POCS. This figure represents the images reconstructed from multiple frames of sparse data collected at various frequencies.

The label f-4-2 corresponds to $\kappa = 4$ and data collection at two frequencies.

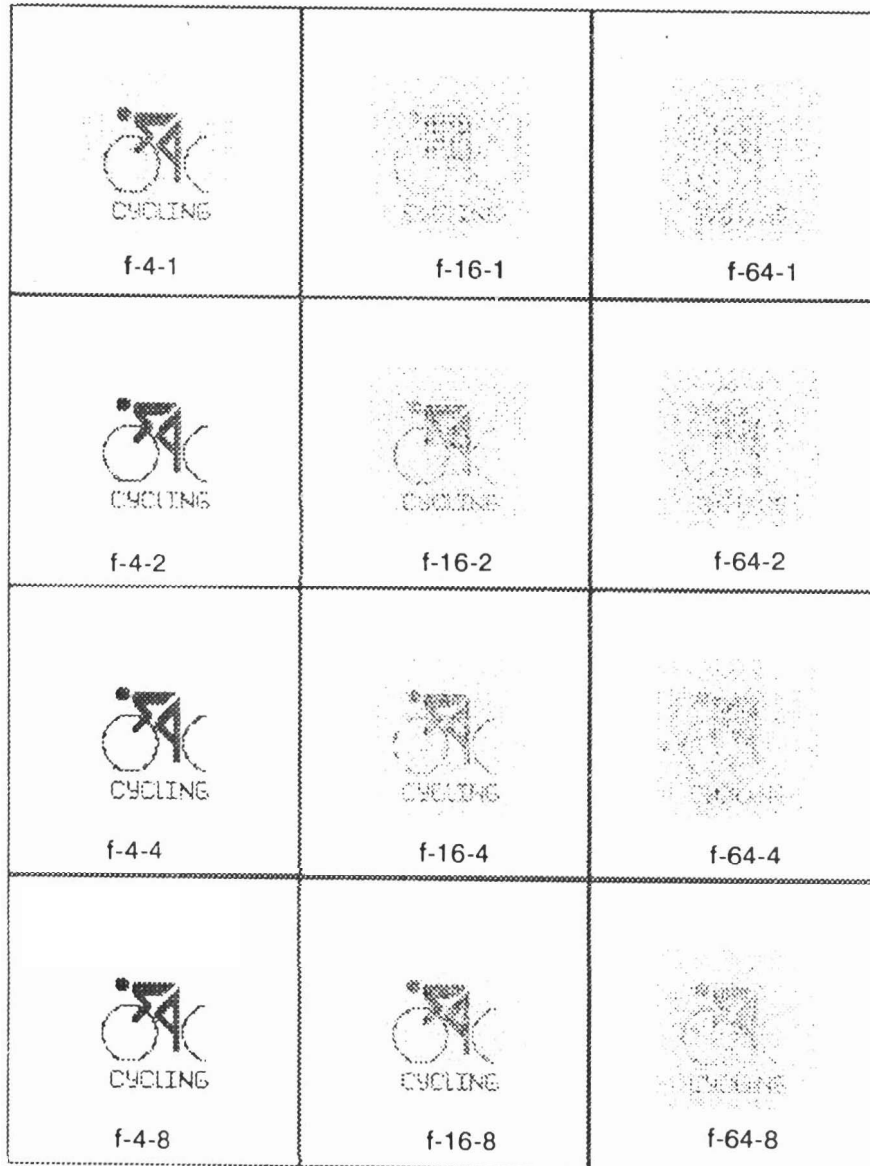


Fig.4.2. Image reconstruction from multiple frames of sparse data using the method of POCS. This figure represents the images reconstructed from multiple frames of sparse data collected at various frequencies.

The label f-4-2 corresponds to $\kappa = 4$ and data collection at two frequencies.

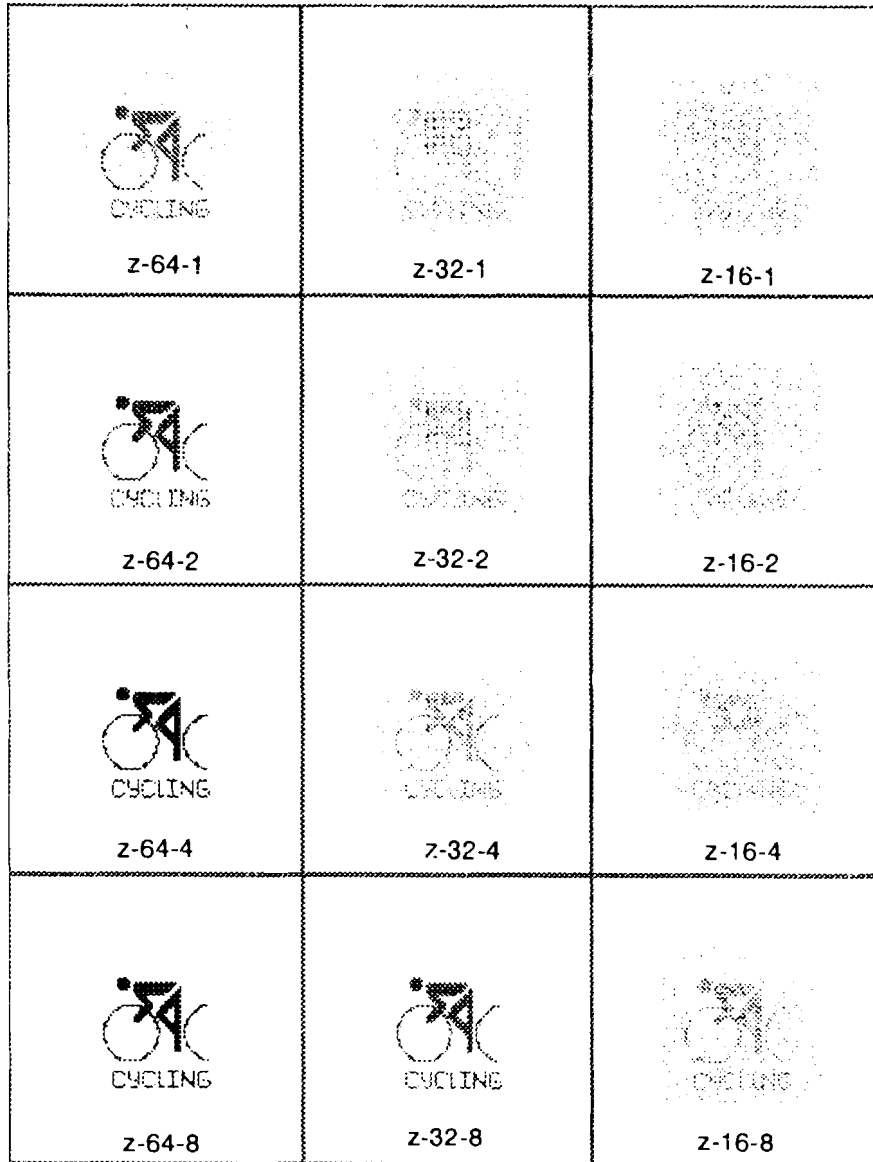


Fig.4.3. Image reconstruction from multiple frames of data using the method of POCS. This figure represents the images reconstructed from multiple frames of sparse data collected at various locations of the receiver array.

The label z-4-2 corresponds to $\kappa = 4$ and data collection at two locations of the receiver array.

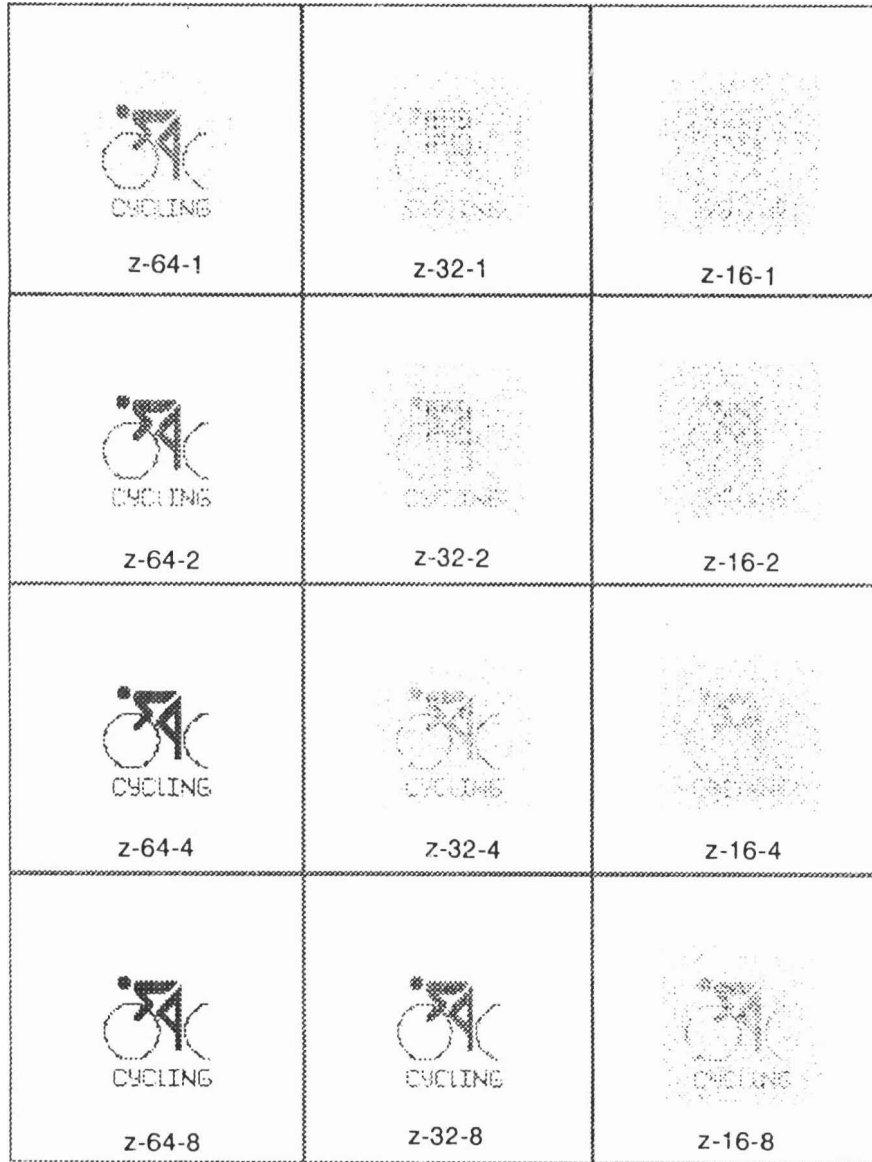


Fig.4.3. Image reconstruction from multiple frames of data using the method of POCS. This figure represents the images reconstructed from multiple frames of sparse data collected at various locations of the receiver array.

The label z-4-2 corresponds to $\kappa = 4$ and data collection at two locations of the receiver array.

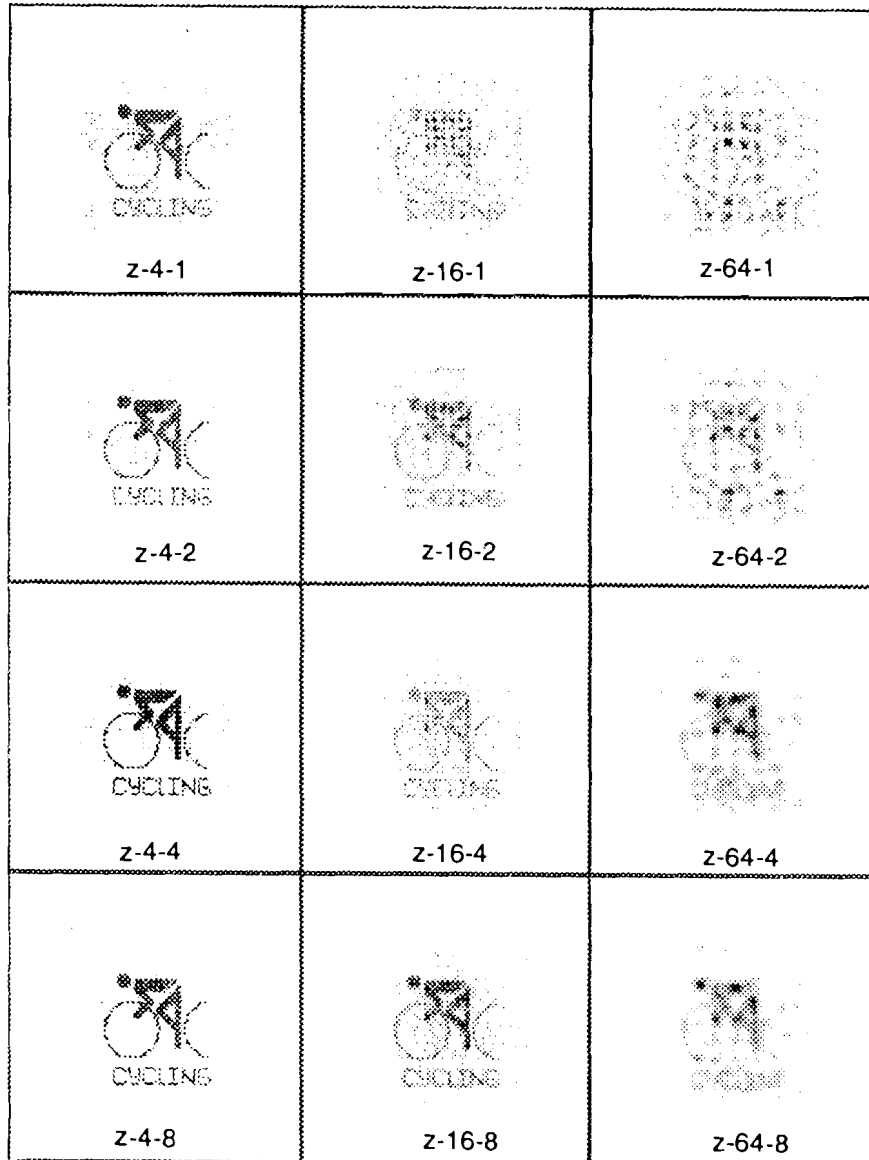


Fig.4.4. Image reconstruction from multiple frames of sparse data using the method of TKM-POCS. This figure represents the images reconstructed from multiple frames of sparse data collected at various locations of the receiver array.

The label z-4-2 corresponds to $\kappa = 4$ and data collection at two locations of the receiver array.

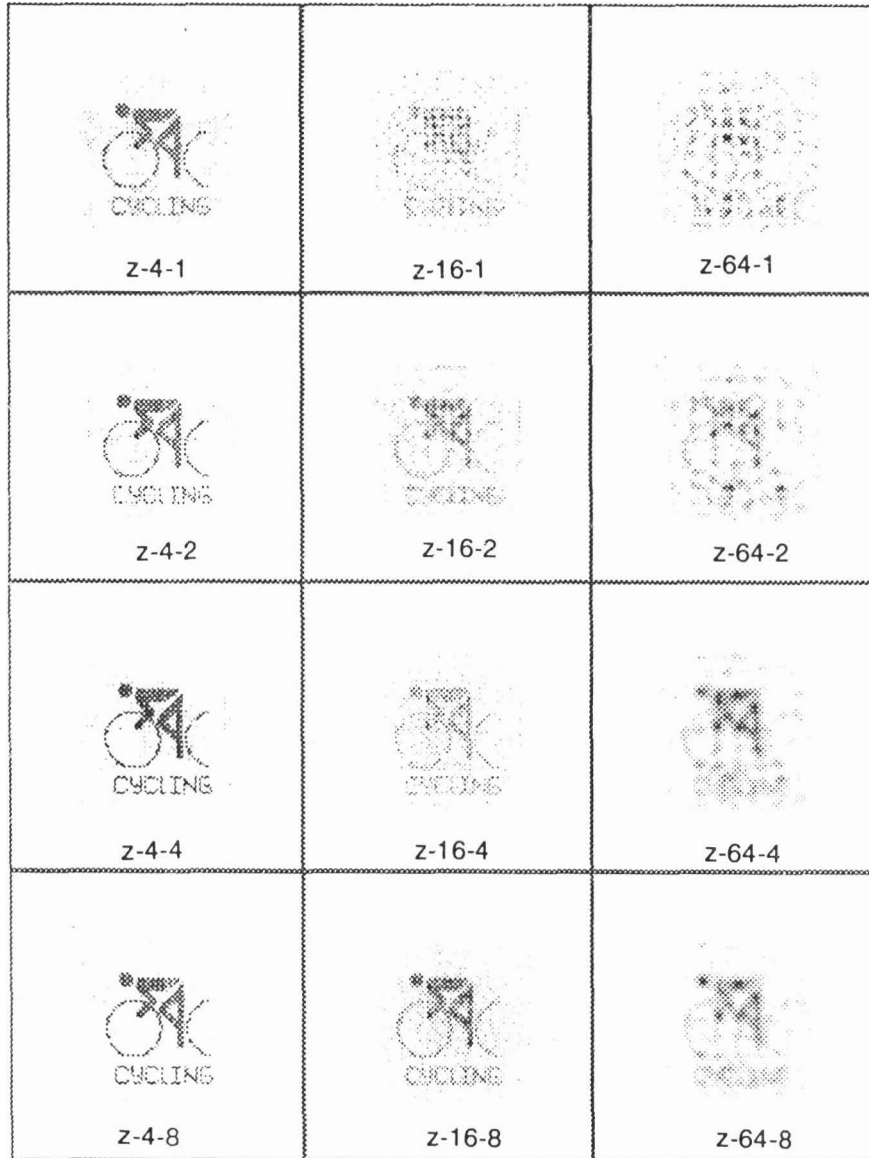


Fig.4.4. Image reconstruction from multiple frames of sparse data using the method of TKM-POCS. This figure represents the images reconstructed from multiple frames of sparse data collected at various locations of the receiver array.

The label z-4-2 corresponds to $\kappa = 4$ and data collection at two locations of the receiver array.

improves (column wise, top to bottom in Figs.4.3 and 4.4). As expected the quality of the image. degrades as the size of the array is decreased (row wise, left to right in Figs.4.3 and 4.4). These results show that the quality of the reconstructed image improves as the number of frames of data is increased irrespective of how the data is collected (either by varying the frequency or by varying the distance).

Fig.4.5 shows the images reconstructed from multiple frames of data collected by varying both frequency and distance. The conclusions are similar to the earlier cases. Note that for each image in Fig.4.5, twice the number of frames are used compared to the corresponding images in Figs.4.2, 4.3, and 4.4. In general, there is an improvement in quality of the reconstructed image when multiple frames of data are combined. This is significant in view of the fact that it is desirable to have a smaller receiver array to reduce complexity and increase maneuverability.

In order to test the performance of these algorithms under noisy conditions, multiple frames of sparse data corresponding to $\kappa = 16$ are generated and Gaussian noise is added to all the frames of sparse data. The method of TKM-POCS is used to combine multiple frames of sparse and noisy data. Fig.4.6a, 4.6b, 4.6c, and 4.6d represent, respectively, the images reconstructed using 10dB, 0dB, -5dB, and -10dB noisy data. It is evident from Fig.4.6 that it is possible to reconstruct images with improved quality even in the presence of noise, when multiple frames of data are combined.

In this Chapter, we have addressed the problem of reconstruction of images from multiple frames of sparse data. The methods of POCS and TKM-POCS have been used to combine multiple frames of sparse data and

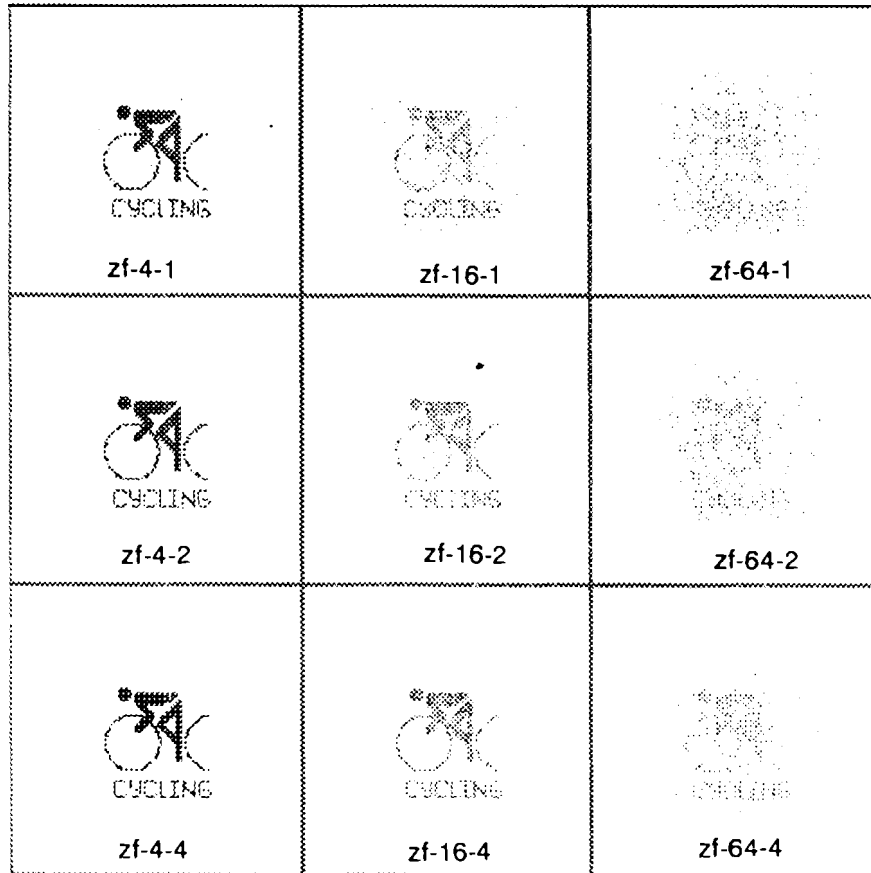


Fig.4.5. Image reconstruction from multiple frames of sparse data using the method of POCS. This figure represents the images reconstructed from multiple frames of sparse data collected at various locations of the receiver and using multiple frequencies.

The label zf-4-2 corresponds to $\kappa = 4$ and data collection at two locations of the receiver array. The number of frequencies used is two in all cases.

incorporate various constraints. It has been shown that images with improved quality can be obtained even when a cycle image (Fig.1.2b), which is more complex image from the reconstruction point of view than the car image (Fig.1.2a), is used to generate sparse data. These algorithms are robust against noise. The results demonstrate that redundant information from multiple frames of data has not only improved the quality of the

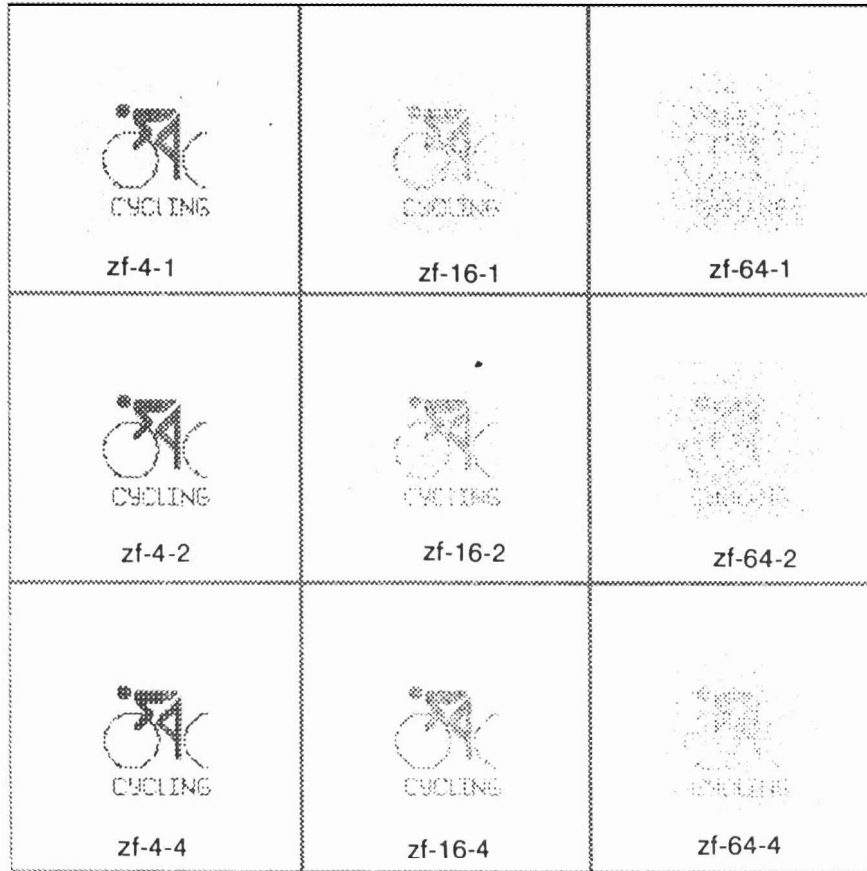


Fig.4.5. Image reconstruction from multiple frames of sparse data using the method of POCS. This figure represents the images reconstructed from multiple frames of sparse data collected at various locations of the receiver and using multiple frequencies.

The label zf-4-2 corresponds to $\kappa = 4$ and data collection at two locations of the receiver array. The number of frequencies used is two in all cases.

incorporate various constraints. It has been shown that images with improved quality can be obtained even when a cycle image (Fig.1.2b), which is more complex image from the reconstruction point of view than the car image (Fig.1.2a), is used to generate sparse data. These algorithms are robust against noise. The results demonstrate that redundant information from multiple frames of data has not only improved the quality of the

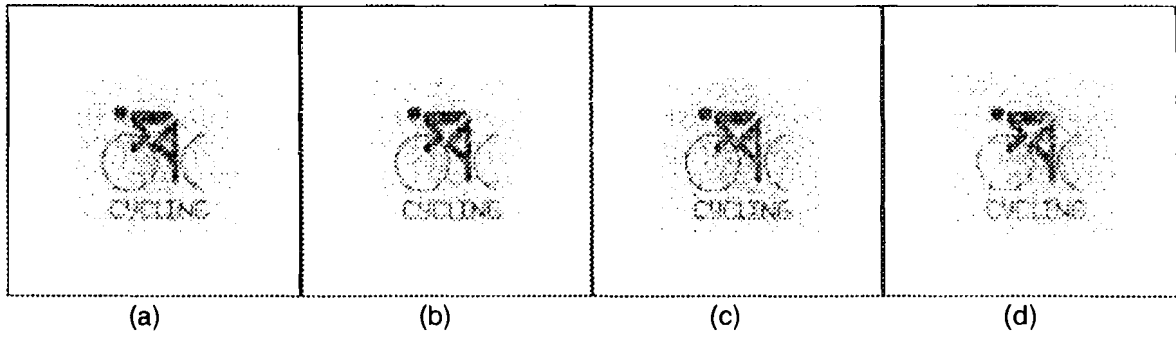


Fig.4.6 Image reconstruction from multiple frames of sparse and noisy data using the method of TKM-POCS. Eight frames of sparse and noisy data ($\kappa = 16$) are used for image reconstruction. This figure shows the images reconstructed when (a) 10dB, (b) 0dB, (c) -5dB, and (d) -10dB sparse and noisy data are used.

reconstructed image but also in reducing the effects of noise in the reconstructed image.

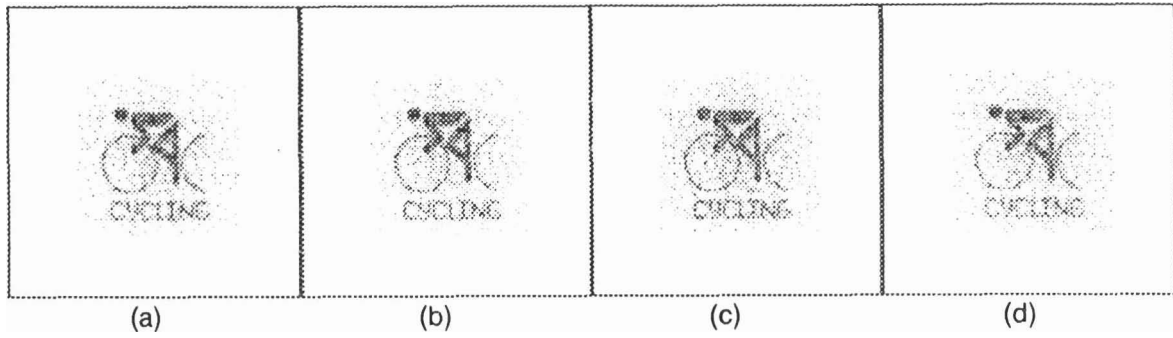


Fig.4.6 Image reconstruction from multiple frames of sparse and noisy data using the method of TKM-POCS. Eight frames of sparse and noisy data ($\kappa = 16$) are used for image reconstruction. This figure shows the images reconstructed when (a) 10dB, (b) 0dB, (c) -5dB, and (d) -10dB sparse and noisy data are used.

reconstructed image but also in reducing the effects of noise in the reconstructed image.

AN ARTIFICIAL NEURAL NETWORK MODEL FOR IMAGE RECONSTRUCTION

We have shown earlier that the ill-posed problem of image reconstruction from sparse data can be solved by incorporating knowledge about the object in the solution and by using redundant information from multiple frames of sparse data. Algorithms based on the methods of POCS and TKM-POCS have been proposed to incorporate knowledge about the object and combine multiple frames of data. These methods require precise knowledge of the constraints about the object, which may not be available always. In this chapter, we propose ANN models for image reconstruction from single and multiple frames of sparse and noisy data. We show that these models do not require precise knowledge of constraints and yet reconstruct images with significantly improved quality.

5.1 Why ANNs for image reconstruction?

Iterative methods for image reconstruction from multiple frames are effective in dealing with sparse data, but they are time consuming. Hence there is a need to speed up the algorithms. To speed up, we have to look for parallelism in the image reconstruction and receiver data generation steps. Apart from speed we are looking for a system which would perform well even under adverse conditions (in terms of low SNR values), and which have a graceful degradation. A good choice to solve such problems would be an ANN model. An ANN model consists of highly interconnected

processing nodes, each of which may be a simple computing element. Besides speed, they are also fault tolerant since computation is performed by distributing it to many processors.

In a neural network, neurons transform an unbounded input activation into a bounded output activation by means of an output signal function $S(x)$. The function is generally known as a logistic function. A simple signal function is given by,

$$S(x) = \frac{1}{1 + e^{-cx}}. \quad (5.1)$$

Fig.5.1 illustrates a differentiable sigmoidal function for various values of c . Nonlinearity of this function increases computational richness of a neural network and facilitates noise suppression [Kosko 92].

Failure of a few receiver elements does not affect the performance of this model. The additional advantage from an **ANN** model is noise suppression.

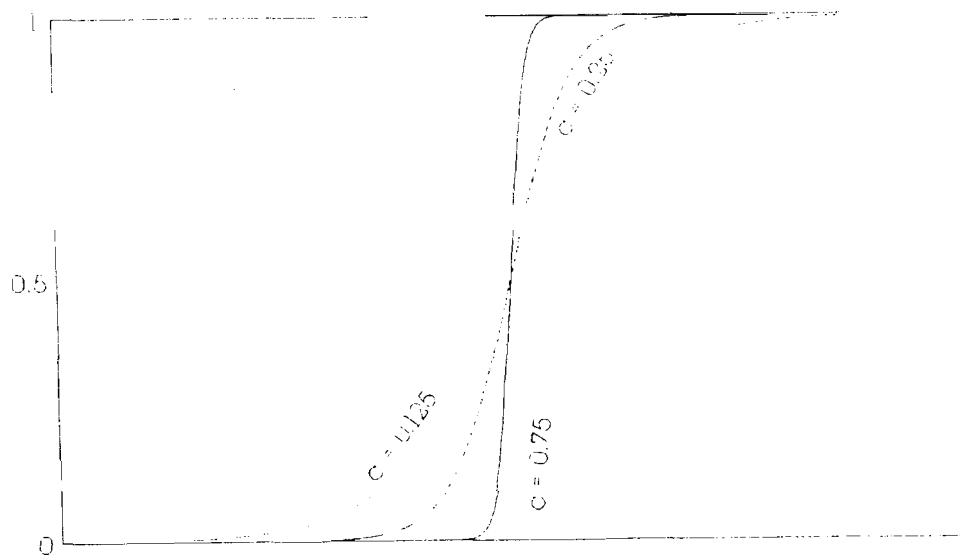


Fig.5.1. A sigmoidal function. The function is plotted for various values of c .

5.2 The proposed neural network model

In the SAI set up shown in Fig.1.1, the receiver array receives a holographic representation of the image of the object. The image formation model of the SAI setup helps us to implement the bidirectional process of data generation and image reconstruction in the form of an ANN model. The proposed neural network model is based on the principles of bidirectional associative memory (BAM) model [Kosko 87].

In the BAM model, information flows in forward and backward directions to produce a two-way search for stored stimulus-response associations. The proposed ANN model consists of two layers of neurons. The first layer consists of M^2 neurons $\{g_1, g_2, g_3, \dots, g_{M^2}\}$. This layer hereafter will be called as data layer. The second layer also consists of M^2 neurons $\{f_1, f_2, f_3, \dots, f_{M^2}\}$ and will be called as the *image* layer. The output values on the neurons $\{f_i, g_i\}$ correspond to the short-term memory. The field of neurons at the data layer is obtained by lexicographically ordering the $M \times M$ receiver data in a row vector form. This is done by stacking the rows of the original receiver data matrix one after the other. Both the data and the image layers are capable of handling complex arithmetic. In order to perform the complex arithmetic, each neuron can be replaced by a pair of neurons dedicating one for the real value and the other for the imaginary value. For the sake of simplicity, we assume that every pair of neurons is replaced by a single complex neuron and we will call this complex neuron as a neuron itself.

The long term memory represented by the connection weight H_{ij} , connects neurons f_i and g_j . It represents the knowledge of the system

through transformation function of the image system model. The matrix mapping $\{\mathbf{H}:\mathbf{f} \rightarrow \mathbf{g}\}$ is a linear associative memory mapping. We call this as the forward mapping, which will be used to create the receiver data \mathbf{g}_s given \mathbf{f} . The forward mapping is fixed and is of size $M^2 \times M^2$. This has a block circulant form. The reverse mapping $\{\mathbf{H}_B:\mathbf{g} \rightarrow \hat{\mathbf{f}}\}$ is not exactly the inverse of the forward mapping but a regularized form (from (3.13)) of \mathbf{H} as shown below:

$$\mathbf{H}_B = (\mathbf{H}^T \mathbf{H} + \rho \mathbf{C}^T \mathbf{C})^{-1} \mathbf{H}^T \quad (5.5)$$

This regularized form enables a smooth reconstruction of the image during the initial stages of the network operation. During the later stages of processing $\mathbf{H}_B \rightarrow \mathbf{H}^{-1}$ as $\rho \rightarrow 0$. This reduces the importance of the smoothness constraint during the later stages of network operation. We have seen in Chapter 3 that regularization blurs the edges of the reconstructed image. The process of reducing the importance of the smoothness constraint will enable the network to reconstruct the edges of the images properly and there will not be any blurring near the edges of the images. Therefore the smoothness operation is used initially to reduce the effects of sparsity and to reconstruct a smooth image. The block diagram of the ANN model for image reconstruction is shown in Fig. 5.2.

5.3 Stability of the proposed neural network model

Stability of the neural network is defined at the equilibrium state of the neural network. At equilibrium, neuronal values do not change with time:

$$\dot{\mathbf{f}} = \frac{d\mathbf{f}}{dt} = 0, \dot{\mathbf{g}} = \frac{d\mathbf{g}}{dt} = 0, \dot{\mathbf{H}} = \frac{d\mathbf{H}}{dt} = 0 \text{ and } \dot{\mathbf{H}}_B = \frac{d\mathbf{H}_B}{dt} = 0. \text{ Here } \mathbf{g} \text{ represents}$$

activation of all the neurons in the data layer. This implies that the pair

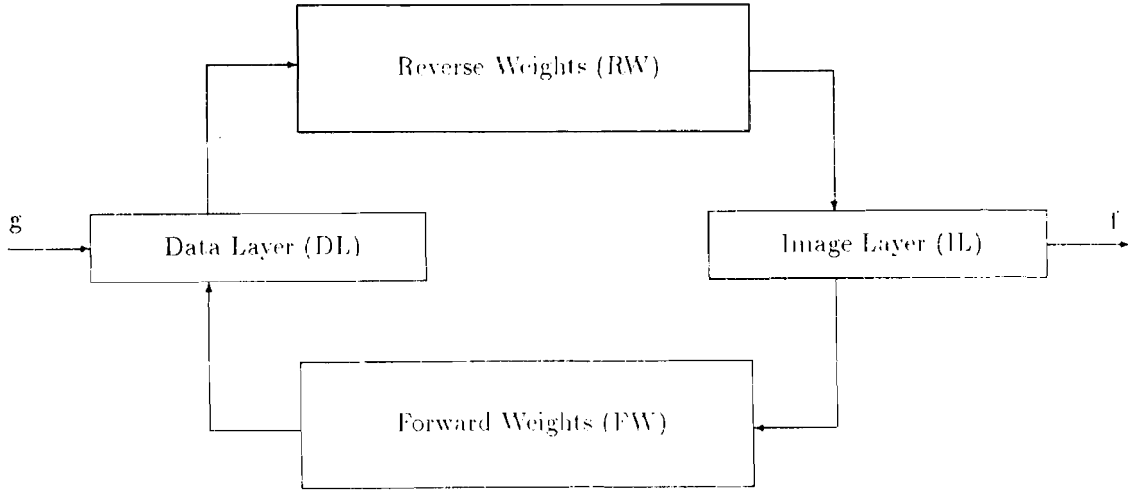


Fig.5.2. Block diagram of the proposed ANN model for image reconstruction from single frame of sparse data.

$\{g, f\}$ is stable. This occurs when the image formation at the image layer stabilizes and the reverse mapping approaches the inverse of the forward mapping, $H_g \rightarrow H^{-1}$. The image reconstruction procedure will stop when stable signals across the image layer make up an image. Like most of the feedback systems, this system is also unstable initially and reaches a stable state when $H_g \rightarrow H^{-1}$. The unstable condition of the neural network during the initial stages of operation is mainly due to the neuronal fluctuations and the reverse synaptic changes. Moreover, the states of the neurons in the data and the image layers change faster than the reverse synaptic weights. Achieving stability requires a delicate balance between stability and convergence [Kosko 90]. Achieving a balance is the central problem in designing a feedback network. The *stability-convergence* dilemma arises due to the neuronal fluctuations and the reverse synaptic changes. Since the reverse synaptic weights vary slowly (due to the variation of p), the neurons in the image layer fluctuate, and thereby produce a change in the values of the neurons at the data layer. Note that the forward mapping H

remains unaltered during the entire operation of the network. The system becomes bidirectionally stable after a few iterations as $\rho \rightarrow 0$ and $\mathbf{H}_B \rightarrow \mathbf{H}^{-1}$.

5.4 Noise suppression

In this model, independent Gaussian noise with zero mean is added to the neurons in the data layer. Noise is independent of the signal processes. Moreover noise is not correlated with the signal. In this model we consider that the neurons in the image layer operate between upper and lower bounds. We assume that the neurons below the lower bound are responsible for noise in the reconstructed image. The noise removal procedure in this ANN model can be viewed as equivalent to contrast enhancement [Grossberg 88]. The signals supported by the data and the smoothing constraint quickly saturate and reach the upper bound and those which have the support only from the data or from the smoothing function remain between the lower and the upper bound. A few neurons qualify to cross the upper threshold during the intermediate stages of the operation. Those of the neurons which do not get support from the data or from the smoothing function fall below the lower bound and are removed every time from further processing.

5.5 An algorithm for image reconstruction from a single frame of sparse data

Initially, the observed sparse and noisy data \mathbf{g}_s is made available at the data layer and rest of the neurons are set to have zero activation or random values. As this model is a holographic memory model, each neuron from the data layer sends its output activation across each of the synaptic

weights H_{Bij} . Each of the neuron f_j at the image layer receives the weighted sum $\sum_i H_{Bij}g_i$. The neuron f_j at the image layer receives the weighted sum independently from all g_i 's and the net activation for the neuron f_j is given by

$$net_j = H_{1j}g_1 + H_{2j}g_2 + \dots + H_{N^2j}g_{M^2}, \quad \text{for } j = 1, 2, \dots, M^2. \quad (5.6)$$

net_j value is processed by the neuron f_j using a nonlinear threshold function and it produces an output f_j^o . Output of every neuron is processed independently. The output of the image layer is the reconstructed image. In order to improve the resolution of the reconstructed image, the column vector at the image layer is fed back through forward weights H . Now a new set of activations is available for the neurons at the data layer. During this feedback process, each neuron at the image layer sends its output across the network through the forward weights to produce a new set of activations g_j 's. The known values of the g_j 's of size Q^2 , $Q^2 < M^2$, are clamped to the input and it is synchronized with the arrival of the output activation from the image layer. This process replaces the calculated values at the data layer. Now all the neurons in the data layers have some activation values and this layer no longer has sparse data. The new set of g_j 's will now be used to obtain a new set of f_j 's. This forward and reverse flow of information continues until the system settles in an equilibrium for the given pair $(\mathbf{g}, \hat{\mathbf{f}})$. The resulting state corresponds to the local minima of the energy of the system. In other words, at this state all the available information is used in the reconstruction process. The algorithm for image reconstruction is given in Algorithm 5.1.

Algorithm 5.1. Image reconstruction from single frame of sparse and noisy data

1. Initialize the forward synaptic weights using the matrix \mathbf{H} and reverse synaptic weights using \mathbf{H}^B . The total number of synaptic weights in the forward and reverse directions is $M^2 \times M^2$. The number of neurons in the image and the data layer is M^2 . The size of the sparse data is Q^2 ($Q^2 < M^2$). Let \mathbf{g} be the measured data. The neurons in the data layer are clamped using these Q^2 values and rest of them are set to have zero activation. $\rho = 0.6$
2. Propagate the data \mathbf{g} through the reverse synaptic weight matrix \mathbf{H}_B .
3. Calculate the net activation at the image layer.
 $\mathbf{net} = \mathbf{H}_B \mathbf{g}$, where $\mathbf{net} = \{net_1, net_2, \dots, net_{M^2}\}$
4. Use the sigmoidal function and obtain the output activation of each neuron at the image layer.

$$\hat{\mathbf{f}}_i = \mathbf{S}(net_i) = \begin{cases} 1 & \text{if } \hat{\mathbf{f}}_i > \theta_1 \\ \hat{\mathbf{f}}_i & \text{if } \theta_2 < \hat{\mathbf{f}}_i \leq \theta_1 \\ 0 & \text{otherwise} \end{cases}$$
5. Send the activation of the neurons through the forward synaptic weights and obtain a new set of \mathbf{g}_i 's. $\mathbf{g}_{new} = \mathbf{H} \hat{\mathbf{f}}$
6. Reduce the value of the regularization parameter ρ . $\rho = \frac{\rho}{2}$.
7. $\mathbf{g} \leftarrow \mathbf{g}_{new}$. Replace Q^2 values of \mathbf{g} with the measured values \mathbf{g}_m .
 $\mathbf{g} \leftarrow \mathbf{g} \downarrow \mathbf{g}_m$, where \downarrow represents the replacement operation.
8. Repeat 2 through 7 until the system settles into an equilibrium state.
9. Form the image ($M \times M$) by taking every M elements of the column vector of $\hat{\mathbf{f}}$ and stacking them one over the other as a row vector to form a two-dimensional image.

5.6 Image reconstruction using sparse and noisy data - Simulation results

The receiver data corresponding to $\kappa = 16$ is simulated. Gaussian noise with zero mean is added to the sparse data. The receiver data corresponding to the initial estimate of the image is computed. In order to improve the accuracy of the estimate, a method similar to the one described in the literature [Mariadassou 90] is used, where the known receiver data samples replace the corresponding estimated receiver data samples repeatedly in each iteration. The results obtained using the inverse filter, the method of POCS, the method of TKM, and the method of TKM-POCS are compared with the results of the ANN model.

The algorithm developed in Section 5.5 is used for image reconstruction from sparse and noisy data. Images in Fig.5.3 show the image reconstruction results from noise free sparse data ($\kappa = 16$) generated using the car image shown in Fig.5.3a. To compare the performance of this ANN model with the other methods of image reconstruction, the images reconstructed using inverse filtering, the method of POCS, the method of TKM and the method of TKM-POCS are presented again. It has been demonstrated already in Chapter 3 that incorporation of constraints improve the quality of the reconstructed image. Fig.5.3f represents the reconstructed image in which very little knowledge about the object is used as constraints in the reconstruction process. This image (Fig.5.3f) is nearly noise free and most of the edges of the original image are preserved.

In order to test the noise suppression property of the proposed model, Gaussian noise with zero mean is added to the sparse data. Sparse data is corrupted with noise to get an $\text{SNR} = 0\text{dB}$, and the reconstructed images from this corrupted data is shown in Fig.5.4. Though very little knowledge

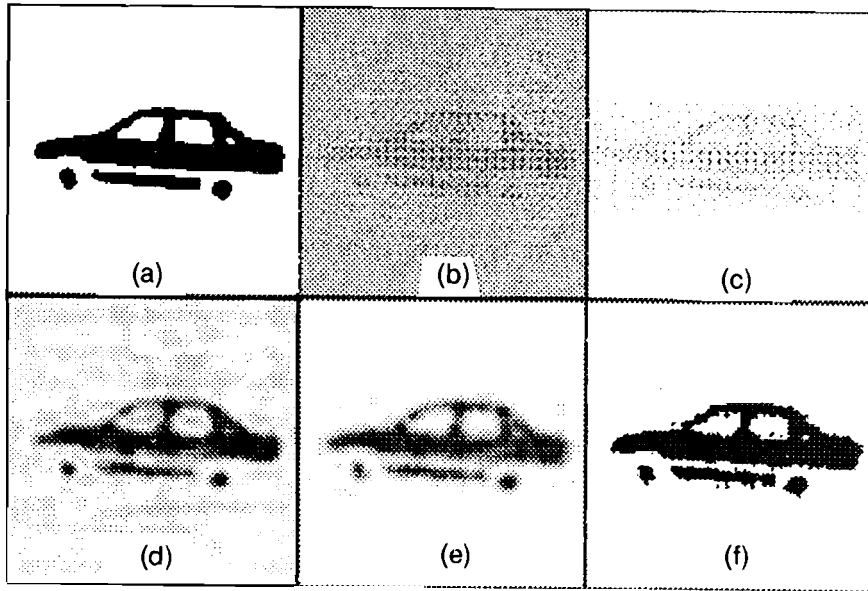


Fig.5.3. Image reconstruction using five different methods. This figure shows (a) the original image, and the images reconstructed using (b) inverse filtering, (c) the method of POCS, (d) the method of TKM-POCS, (e) the method of TKM-POCS and (f) the ANN model. In all the cases, noise free sparse data ($\kappa = 16$) was used.

about the object is used, the image (Fig.5.4d) reconstructed from ANN model is nearly noise free, and the edges are preserved. The noise level in the data is increased further. The sparse data is corrupted to get an SNR = - 10dB, and the images are reconstructed using all the four methods

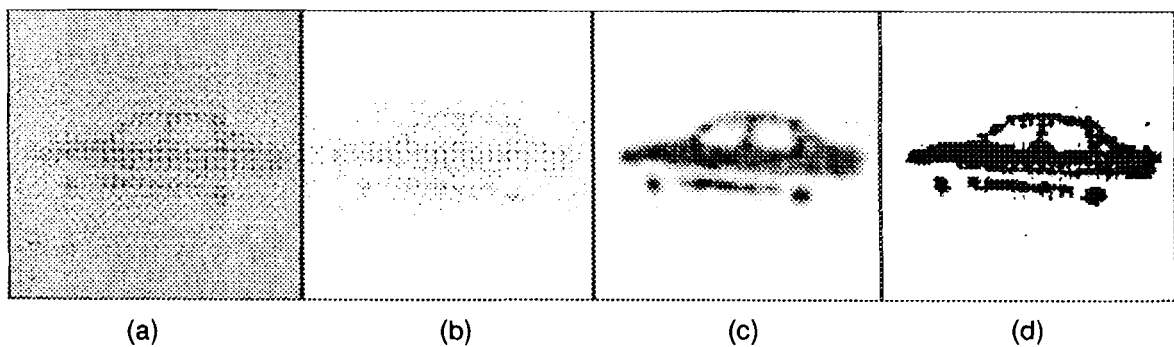


Fig.5.4. Image reconstruction using sparse and noisy data. This figure shows the images reconstructed using (a) inverse filtering, (b) the method of POCS, (c) the method of TKM-POCS, and (d) the ANN model. In all the cases, the noisy sparse data ($\kappa = 16$, SNR = 0dB) was used.

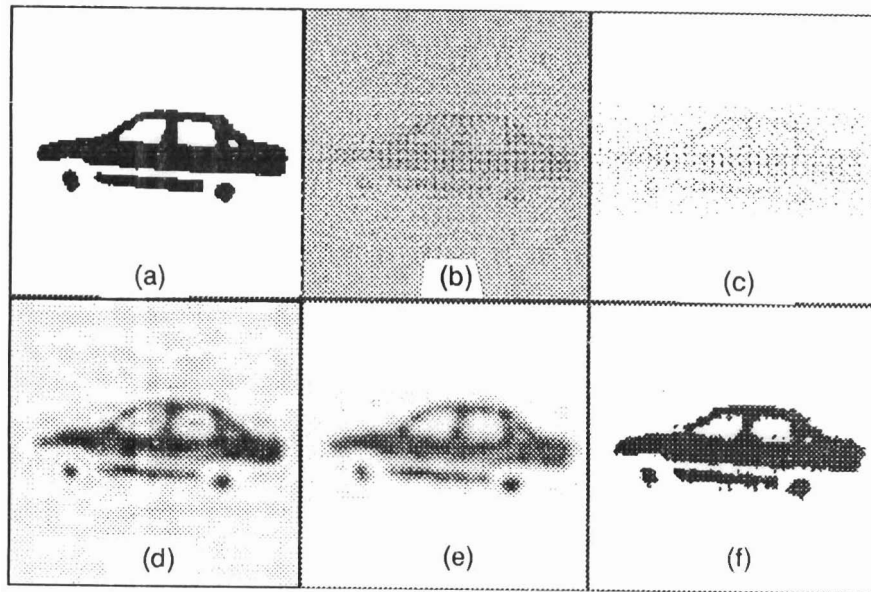


Fig.5.3. Image reconstruction using five different methods. This figure shows (a) the original image, and the images reconstructed using (b) inverse filtering, (c) the method of POCS, (d) the method of TKM-POCS, (e) the method of TKM-POCS and (f) the **ANN** model. In all the cases, noise free sparse data ($\kappa = 16$) was used.

about the object is used, the image (Fig.5.4d) reconstructed from ANN model is nearly noise free, and the edges are preserved. The noise level in the data is increased further. The sparse data is corrupted to get an $\text{SNR} = -10\text{dB}$, and the images are reconstructed using all the four methods

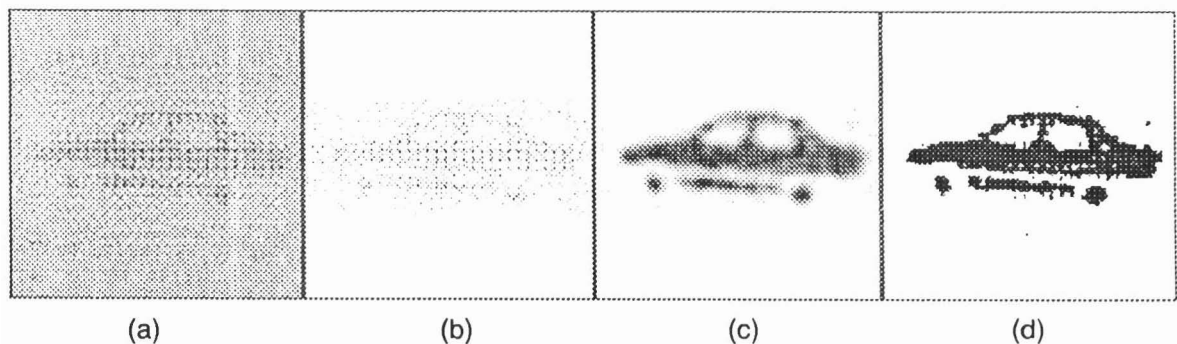


Fig.5.4. Image reconstruction using sparse and noisy data. This figure shows the images reconstructed using (a) inverse filtering, (b) the method of POCS, (c) the method of TKM-POCS, and (d) the **ANN** model. In all the cases, the noisy sparse data ($\kappa = 16$, $\text{SNR} = 0\text{dB}$) was used.

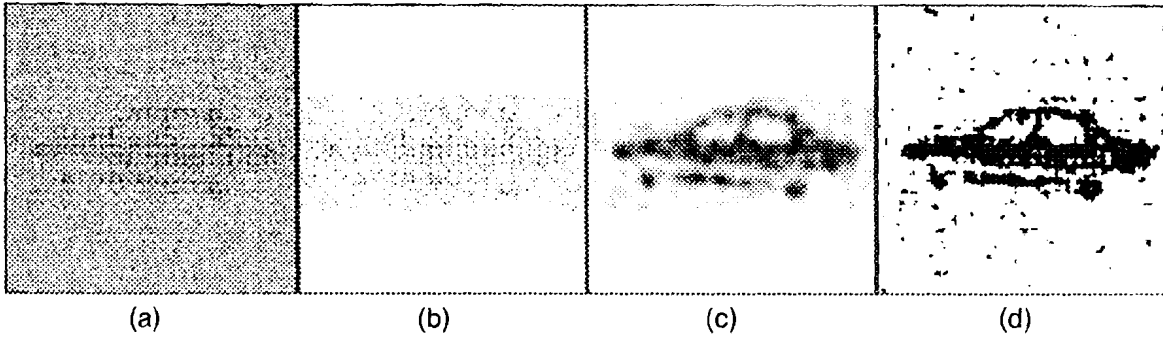


Fig.5.5. Image reconstruction using sparse and noisy data. This figure shows the images reconstructed using (a) inverse filtering, (b) the method of POCS, (c) the method of TKM-POCS, and (d) the ANN model. In all the cases, the noisy sparse data ($\kappa = 16$, SNR = -10dB) was used.

as before. The reconstructed images are shown in Fig.5.5. Though there is noise in the reconstructed image (Fig.5.5d) by ANN model, the image is still clear. Thus the proposed ANN model performs well even when low SNR data is used for image reconstruction. In this case also the performance of the ANN model is better than the performance of the other three methods. The edge preserving property of this model is demonstrated in Fig.5.6. The edge preserving property of ANN model is compared with that the method of TKM-POCS. The images shown in Fig.5.6 are obtained by finding the difference between the original image shown in Fig.5.3a and the reconstructed images. Images in the top row, Figs.5.6a, 5.6b, and 5.6c represent, respectively, the difference images obtained between Fig.5.3a and Fig.5.3e, Fig.5.3a and Fig.5.4c, and Fig.5.3a and Fig.5.5c. Note that the difference images are obtained from the reconstructed images (gray scale images) and not from the dithered images. In this case, all the edges of the original image are blurred. This is indicated by the continuous line along the edges of the car. As the noise level increases (from left to right), error in the reconstructed images also increases. This is indicated by the noise within and outside the region of the car. The second row in Fig.5.6

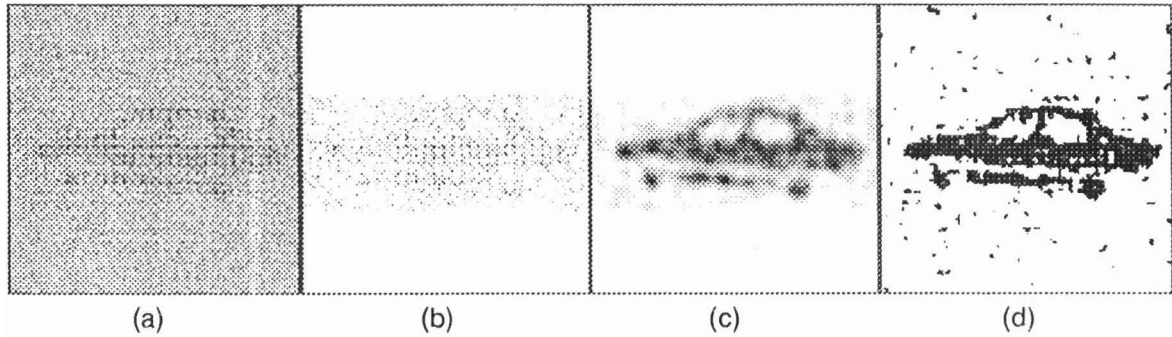


Fig.5.5. Image reconstruction using sparse and noisy data. This figure shows the images reconstructed using (a) inverse filtering, (b) the method of POCS, (c) the method of TKM-POCS, and (d) the ANN model. In all the cases, the noisy sparse data ($a = 16$, $\text{SNR} = -10\text{dB}$) was used.

as before. The reconstructed images are shown in Fig.5.5. Though there is noise in the reconstructed image (Fig.5.5d) by ANN model, the image is still clear. Thus the proposed ANN model performs well even when low SNR data is used for image reconstruction. In this case also the performance of the ANN model is better than the performance of the other three methods. The edge preserving property of this model is demonstrated in Fig.5.6. The edge preserving property of ANN model is compared with that the method of TKM-POCS. The images shown in Fig.5.6 are obtained by finding the difference between the original image shown in Fig.5.3a and the reconstructed images. Images in the top row, Figs.5.6a, 5.6b, and 5.6c represent, respectively, the difference images obtained between Fig.5.3a and Fig.5.3e, Fig.5.3a and Fig.5.4c, and Fig.5.3a and Fig.5.5c. Note that the difference images are obtained from the reconstructed images (gray scale images) and not from the dithered images. In this case, all the edges of the original image are blurred. This is indicated by the continuous line along the edges of the car. As the noise level increases (from left to right), error in the reconstructed images also increases. This is indicated by the noise within and outside the region of the car. The second row in Fig.5.6

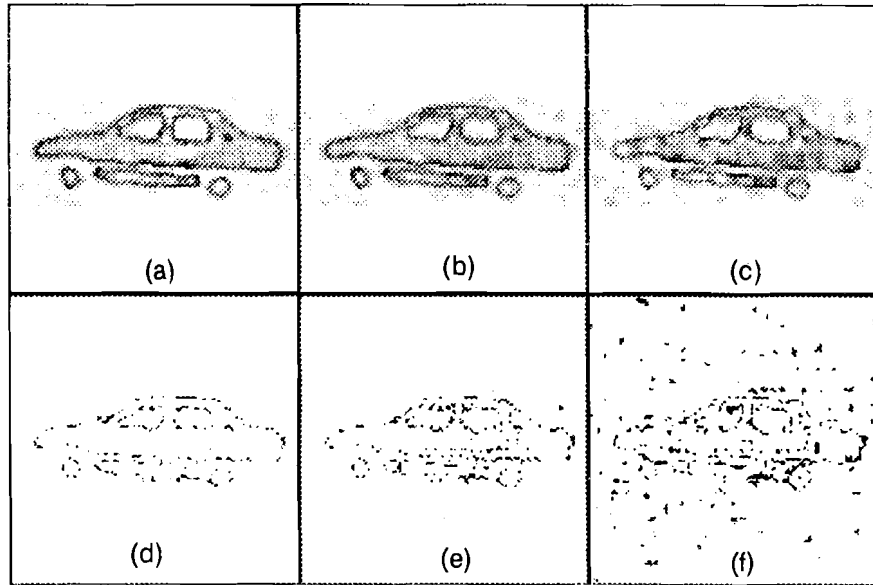


Fig.5.6. Illustration of the image reconstruction accuracy of the proposed method. The images in this figure show the difference images obtained between the original image in Fig.1.2a and the image in (a) Fig.5.3c, (b) Fig.5.4c, (c) Fig.5.5c, (d) Fig.5.3d, (e) Fig.5.4d, (f) Fig.5.5d. The images in the bottom row (reconstructed using the ANN model) have a few errors when compared with the images in the top row (reconstructed using the TKM-POCS method).

represents, respectively, the difference images obtained between Fig.5.3a and Fig.5.3f, Fig.5.3a and Fig.5.4d, and Fig.5.3a and Fig.5.5d. Most of the edges of the original image are preserved. This is indicated by the discontinuous lines near the edges of the image. As the noise level in the data increases, degradation in the reconstructed image increases but the edges are still preserved.

Images in Fig.5.7 show the image reconstruction results from noise free sparse data ($\kappa = 16$) generated using the cycle image shown in Fig.5.7b. The performance of the ANN model is compared with the other methods of image reconstruction. Figs.5.7b, 5.7c, 5.7d, 5.7e and 5.7f represent the images reconstructed using inverse filtering, the method of POCS, the method of TKM, the method of TKM-POCS and the ANN model,

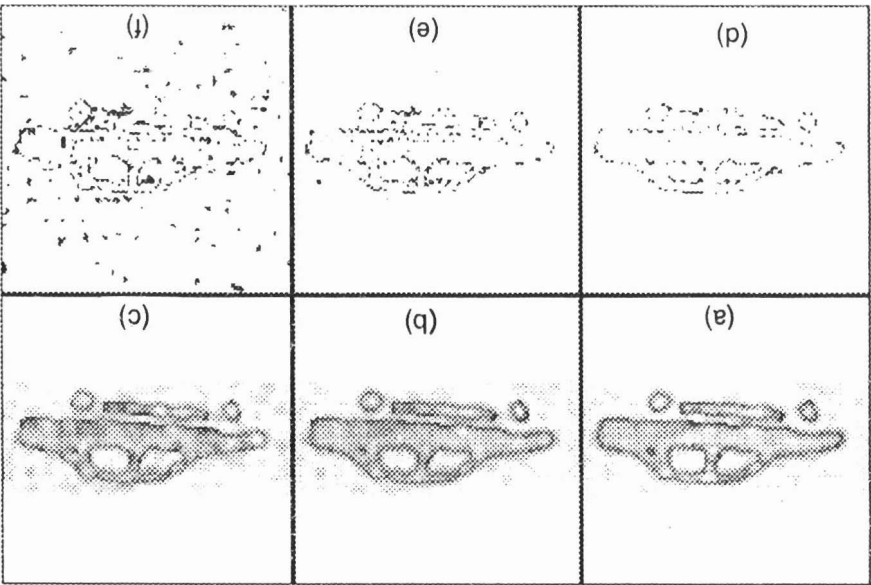


Fig.5.6.

Illustration of the image reconstruction accuracy of the proposed method. The images in this figure show the difference images obtained between the original image in Fig. 1.2a and the image in (a) Fig. 5.3c, (b) Fig. 5.4c, (c) Fig. 5.5c, (d) Fig. 5.3d, (e) Fig. 5.4d, (f) Fig. 5.5d. The images in the bottom row (reconstructed using the ANN model) have a few errors when compared with the images in the top row (reconstructed using the TKM-POCS method).

represents, respectively, the difference images obtained between Fig.5.3a and Fig.5.3t, Fig.5.3a and Fig.5.4d, and Fig.5.3a and Fig.5.5d. Most of the edges of the original image are preserved. This is indicated by the discontinuous lines near the edges of the image. As the noise level in the data increases, degradation in the reconstructed image increases but the edges are still preserved.

Images in Fig.5.7 show the image reconstruction results from noise

free sparse data ($k = 16$) generated using the cycle image shown in Fig.5.7b. The performance of the ANN model is compared with the other methods of image reconstruction. Figs.5.7b, 5.7c, 5.7d, 5.7e and 5.7f represent the images reconstructed using inverse filtering, the method of POCS, the method of TKM, the method of TKM-POCS and the ANN model,

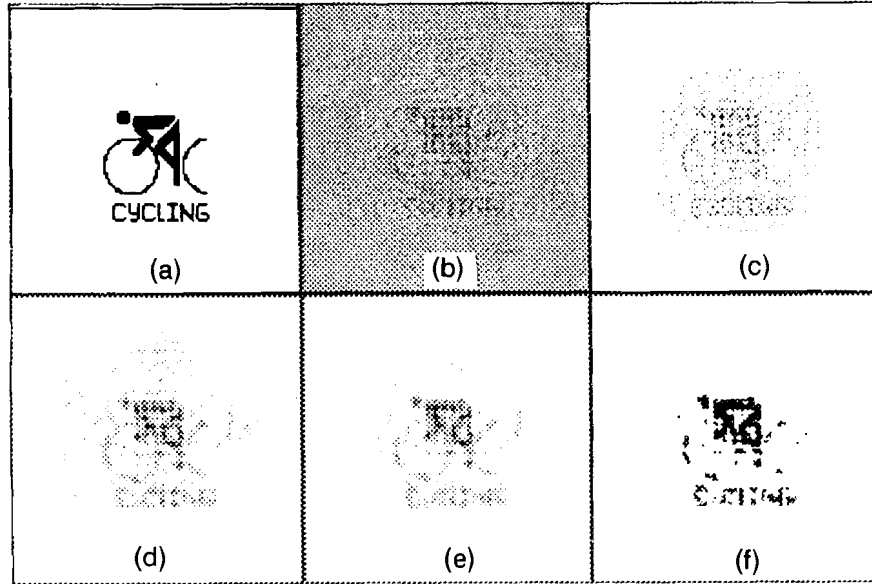


Fig.5.7. Image reconstruction using five different methods. This figure shows (a) the original image and the images reconstructed using (b) inverse filtering, (c) the method of POCS, (d) the method of TKM, (e) the method of TKM-POCS and (f) the ANN model. In all the cases, noise free sparse data ($\kappa = 16$) was used.

respectively. In this case also, the quality of the image reconstructed using the ANN model is better than the quality of the images reconstructed using the other three methods.

It is clear from the simulation studies that the proposed method performs well even under adverse conditions. When the complexity of the problem increases, in terms of noise in the data and complex shape of the object, the performance of the ANN model degrades gracefully. In order to handle the noise, sparsity and complexity of the shape of the object, we propose a cascaded ANN model to reconstruct images from multiple frame data. In the next section, we compare the performance of the reconstruction methods using a new quality measure based on the method of Singular Value Decomposition (SVD).

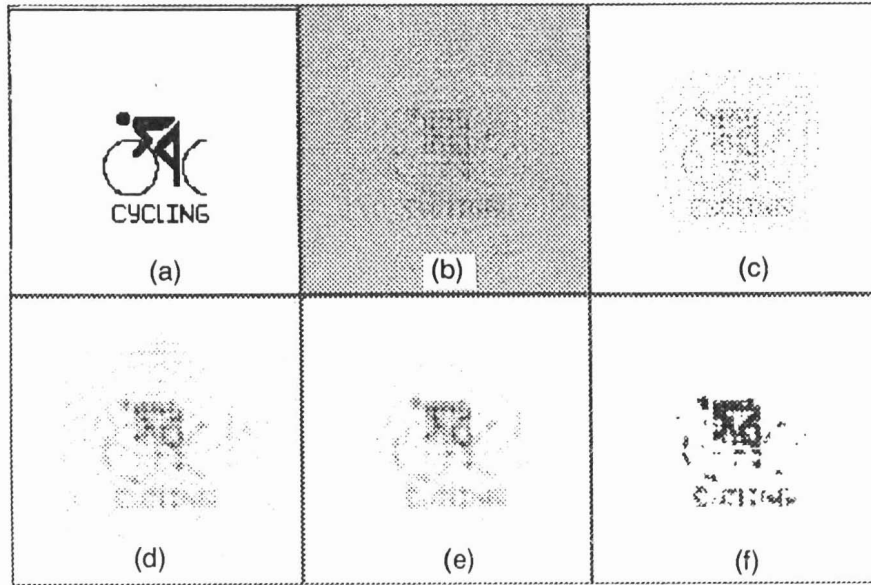


Fig.5.7. Image reconstruction using five different methods. This figure shows (a) the original image and the images reconstructed using (b) inverse filtering, (c) the method of POCS, (d) the method of TKM, (e) the method of TKM-POCS and (f) the ANN model. In all the cases, noise free sparse data ($\kappa = 16$) was used.

respectively. In this case also, the quality of the image reconstructed using the ANN model is better than the quality of the images reconstructed using the other three methods.

It is clear from the simulation studies that the proposed method performs well even under adverse conditions. When the complexity of the problem increases, in terms of noise in the data and complex shape of the object, the performance of the ANN model degrades gracefully. In order to handle the noise, sparsity and complexity of the shape of the object, we propose a cascaded ANN model to reconstruct images from multiple frame data. In the next section, we compare the performance of the reconstruction methods using a new quality measure based on the method of Singular Value Decomposition (SVD).

5.7 Quality measure based on singular value decomposition

If the pixel values of the image are spatially unrelated to one another, the singular values tend to be uniformly distributed in amplitude. The distribution of singular values can be used as a description of the structure in the pixels of the image [Ashjari 82].

We make use of this property to measure the quality of the image. Here the distribution of singular values of an image is compared with that of the original. The distribution of the singular values of the reconstructed image with a better quality will follow closely that of the original image.

In SVD, an $M \times M$ image is treated as an $M \times M$ matrix. The image matrix is decomposed into a sum of a weighted set of unit matrices U and V [Pratt 91].

$$\mathbf{F} = \mathbf{U} \mathbf{\Lambda}^{1/2} \mathbf{V} \quad (5.7)$$

where $\mathbf{\Lambda}^{1/2}$ is the set of singular values. It is also possible to express the matrix decomposition in the form of a series as follows:

$$\mathbf{F} = \sum_{i=1}^r \lambda_i^{1/2} \mathbf{u}_i \mathbf{v}_i^T \quad (5.8)$$

where r is the rank of the \mathbf{F} , \mathbf{u}_i and \mathbf{v}_i are the column vectors of \mathbf{U} and \mathbf{V} , respectively, and $\lambda_i^{1/2}$ is the i th singular value of \mathbf{F} . \mathbf{U} , \mathbf{V} and \mathbf{F} are $M \times M$ matrices. It is assumed that $\lambda_1 > \lambda_2 > \lambda_3 \dots > \lambda_r$, λ_i s are given by

$$\Lambda^{\vee_2} = \left[\begin{array}{ccccc|c} \lambda_1^{\vee_2} & 0 & 0 & \cdot & \cdot & \mathbf{0} \\ 0 & \lambda_2^{\vee_2} & 0 & \cdot & \cdot & \\ 0 & 0 & \lambda_3^{\vee_2} & \cdot & \cdot & \\ \cdot & \cdot & \cdot & \cdot & \cdot & \\ \cdot & \cdot & \cdot & \cdot & \lambda_r^{\vee_2} & \\ \hline & & & & & \mathbf{0} \\ & & & & & \mathbf{0} \end{array} \right] \quad (5.9)$$

If the same image is corrupted with noise, then the number of singular values will be more than r .

The plot in Fig.5.8 gives the logarithm of the singular values ($\log \lambda_i$) of the images shown in Fig.5.3. Singular value distribution of the original image is shown as the thick line in the plot. As the image reconstructed using the inverse filtering is noisy, the singular values are nearly uniformly distributed in amplitude. When the finite support is applied to the reconstructed image, the distribution of the singular values is different from the earlier case. When the finite support and positivity constraints are incorporated into the reconstruction algorithm using the method of POCS, the distribution of the

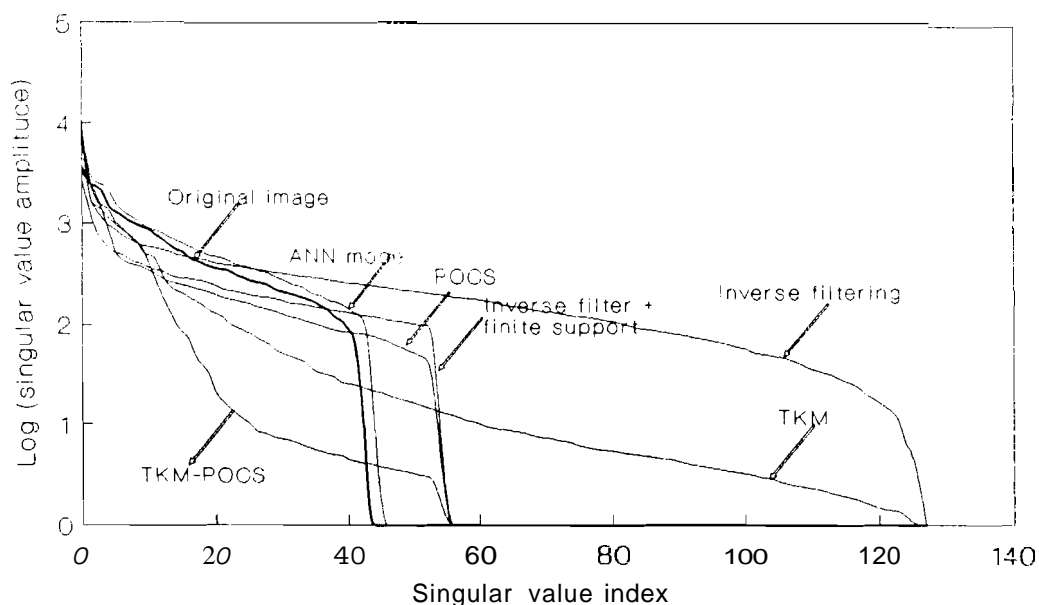


Fig.5.8 Comparison of performance of four methods of image reconstruction using SVD for the car image.

singular values is nearly the same as the earlier case. It is clear from these two cases that the number of singular values depends on the finite support. For the image reconstructed using the method of TKM, the distribution of the singular values is quite different from that of the inverse filtered case, as smoothing constraint was used in the reconstruction process. In the case of the image reconstructed using the method of TKM-POCS also, the distribution of the singular values does not quite follow the original due to the incorporation of the smoothness constraint along with the finite support and the positivity constraints. The smoothness constraint forces unnatural correlation among the pixels of the image which is undesirable. The singular values obtained from the image reconstructed from the ANN model closely follow that of the original even though the reconstruction process did not use the finite support constraint, and the smoothness constraint was used only during the initial stages of the network operation.

The singular values for the images shown in Fig.5.7 are plotted on a logarithmic scale in Fig.5.9. The distribution of the singular values for the original image is shown as a thick line in the plot. As the reconstructed image using the inverse filtering is noisy, the distribution of the singular values is nearly uniform. The distribution of the singular values for the image reconstructed using the method of POCS is nearly the same as that of the inverse filtered case. For the image reconstructed using the method of TKM, the distribution of the singular values is quite different from that of the inverse filtered case, as smoothing constraint was used in the reconstruction process. The distribution of the singular values obtained from the image reconstructed using the method of TKM-POCS did not deviate much from that of the image reconstructed using the method of POCS. This small deviation reflects the fact that smoothing effect was negligible in the

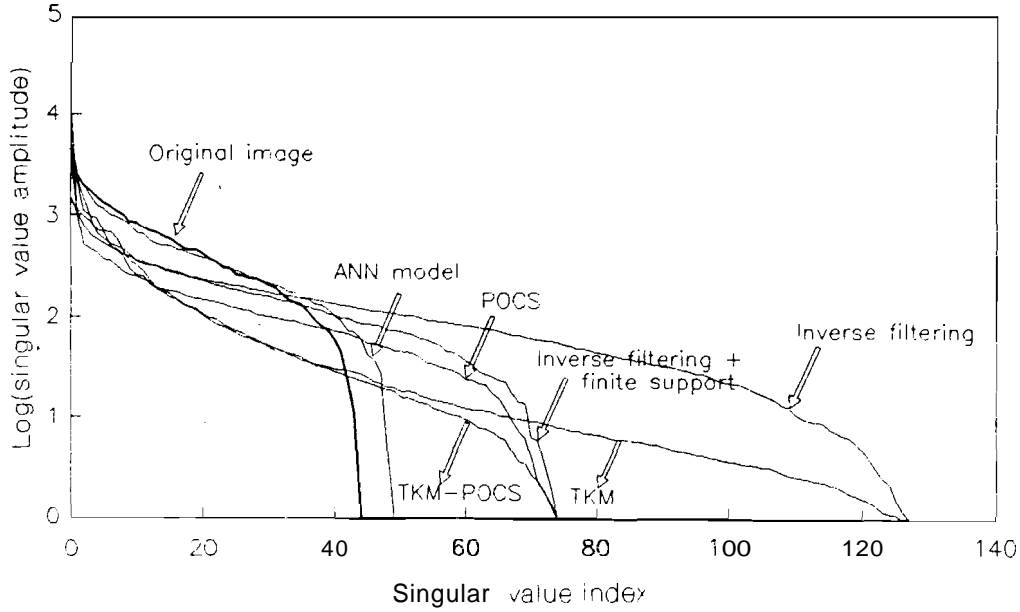


Fig.5.9 Comparison of performance of four methods of image reconstruction using SVD for the cycle image.

reconstruction process. The singular values obtained from the image reconstructed from the ANN model closely follow that of the original, even though the reconstruction process did not use the finite support constraint and the smoothness constraint was used only during the initial stages of the network operation. This quality measure based on the distribution of the singular values demonstrates clearly that the images reconstructed using the ANN model have significantly improved quality.

5.8 Algorithm for image reconstruction from multiframe data

In this section, we develop an algorithm to reconstruct high resolution image from multiple frames of data. Let $\{\mathbf{g}_{s1}, \mathbf{g}_{s2}, \mathbf{g}_{s3}, \dots, \mathbf{p},\}$ be K frames of data collected by using the multifrequency method [Mariadossou 90] or using the multiframe method discussed in [Yegnanarayana 89]. We follow the approach [Yegnanarayana 89] to collect multiple frames of sparse data. The architecture of this model consists of a cascade of the ANNs described

in Section 5.2. The block diagram of this model is shown in Fig.5.10. This block diagram represents a cascaded model where four frames of sparse data can be combined. This can be extended to any number of frames by cascading the single frame ANN model one below the other. Since the sparse data depends on the object-receiver distance (\mathbf{z}) and the impulse response is a function of \mathbf{z} , the forward and the reverse synaptic weights connecting the data and image layers have to be initialized appropriately. The output of each block is connected to the input of the next block through appropriate forward synaptic weights. If we assume K frames of sparse

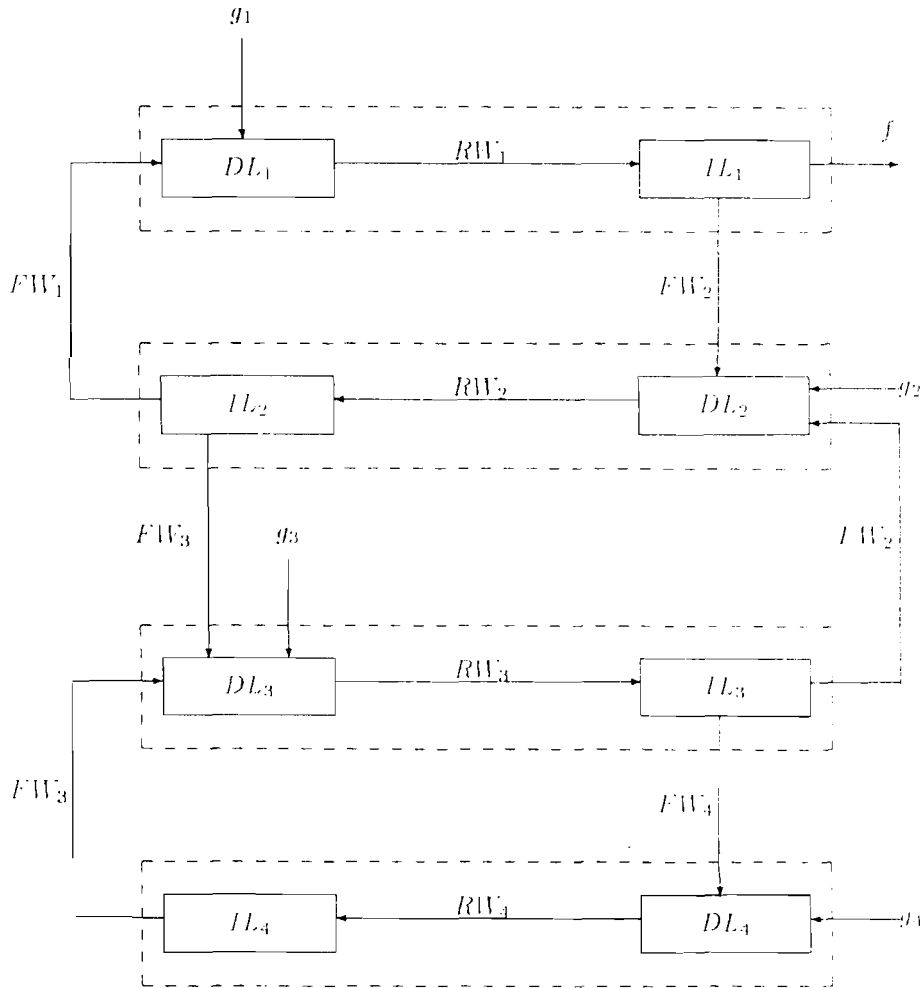


Fig.5.10 Block diagram of a cascaded ANN model for multiframe image reconstruction.

data, then K such blocks are required. Then there will be K forward $\{\mathbf{H}_1, \mathbf{H}_2, \mathbf{H}_3, \dots, \mathbf{H}_K\}$ and K reverse $\{\mathbf{H}_{B1}, \mathbf{H}_{B2}, \mathbf{H}_{B3}, \dots, \mathbf{H}_{BK}\}$ synaptic weights. The output of the K th block is fed back to the $(K - 1)$ th block. This model can be simplified by considering only a single block with appropriate change of weights during every cycle of the network operation. The sparse data at each data layer has to be synchronized with the incoming signals which arrive at the data layer through the forward synaptic weights from the previous block.

5.8.1 *Stability of the cascaded ANN model*

This cascaded network was found to be stable even though the forward and the reverse weights change during every cycle due to the change of image formation model parameter z . Due to the redundant information that is made available through the multiple frames of sparse data, the reconstructed image settles quickly and becomes consistent with all the available data. Moreover, the value of p is kept very low, and $p \rightarrow 0$ quickly and to obtain $\mathbf{H}_B \rightarrow \mathbf{H}^{-1}$. Therefore the neuronal activation at the image and data layer settle quickly and the network becomes stable. The stability of this network is also attributed to the fact that the synaptic weights are not random weights but represent the reconstruction and data generation process.

5.8.2 *Operation of the cascaded ANN model*

The operation of this network is similar to the one described in Section 5.2. The reverse weights are initialized using the transformation function \mathbf{H}_{B1} , where \mathbf{H}_{B1} refers to the reverse synaptic weights for the first frame. The net activation at the image layer is calculated as before. In order to incorporate

the next frame data, the column vector at the image layer is fed to the next block through forward weights \mathbf{H}_2 , which is the corresponding matrix of synaptic weights for the second frame. In other words, feeding the output of the neurons in the image layer through the synaptic weights \mathbf{H}_2 simulate the receiver data for the second frame. This output is fed to the neurons in the data layer of the second block. A new set of activations are available for the neurons at the data layer. The measured sparse data values of the second frame clamp the values of the corresponding neurons in the data layer. Neurons in this data layer not only contain the measured value but also have some additional information obtained from the first frame. Now all the neurons in the data layer have some activation values and the data in this layer is no longer a sparse data. The new set of values for the neurons in the data layer is used to produce a new set of values in the image layer through the reverse synaptic weights \mathbf{H}_1 . The sequential flow of information through all the blocks is continued. The output of the last block is fed back to the $(K - 1)th$ block through the forward synaptic weights \mathbf{H}_{K-1} . This forward flow of information and the cyclic feedback are continued until the system settles in an equilibrium for the given pair $(\mathbf{g}, ?)$. This state corresponds to the local minima of the energy of the system. In other words, all the available information from multiple frames of sparse data is used in the reconstruction process. This cascaded model reaches the equilibrium in a short time due to the redundant information that is made available. Stable images are formed at each image layer very quickly, and they are consistent with the available sparse data. The algorithm for image reconstruction is given in Algorithm 5.2.

Algorithm 5.2. Image reconstruction from multiple frames of sparse and noisy data

1. Number of frames = K . Let $i = 1$. Let $\{\mathbf{g}_{s1}, \mathbf{g}_{s2}, \mathbf{g}_{s3}, \dots, \mathbf{g}_{sK}\}$ be the measured sparse data. Initialize all the connections between the data and the image layers appropriately using the forward synaptic weights and reverse synaptic weights. The total number of synaptic weights in the forward/reverse direction: is $M^2 \times M^2$. Number of neurons in each of the image and in the data layer is M^2 . The size of the sparse data is Q^2 ($Q^2 < M^2$). Let \mathbf{g}_{si} represent the measured data of the i th frame. The neurons in the first data layer are clamped using Q^2 values and rest of them are initialized to zero activation. $p = 0.6$.
2. Propagate the data \mathbf{g}_i through the reverse synaptic weight matrix \mathbf{H}_{Bi} .
3. Calculate the net activation at the image layer. $\text{out} = \mathbf{H}_{Bi}\mathbf{g}_i$.
4. Use the sigmoidal function and obtain the output activation of each neuron at the image layer.
$$\hat{f}_j = \mathbf{S}(\text{out}_j) = \begin{cases} 1 & \text{if } \hat{f}_j > \theta_1 \\ \hat{f}_j & \text{if } \theta_2 < \hat{f}_j \leq \theta_1 \\ 0 & \text{otherwise} \end{cases}$$
5. Send the activation of the neurons through the forward synaptic weights and obtain a new set of \mathbf{g}_{si} 's.
$$\mathbf{g}_{\text{new}} = \mathbf{H}_{ki} \hat{\mathbf{f}}, \text{ where } \mathbf{H}_{ki} \text{ is appropriately selected based on the direction of the reconstruction cycle}$$
6. Reduce the value of the regularization parameter p . $p = p/2$.
7. $i = i + 1$
8. $\mathbf{g}_i \leftarrow \mathbf{g}_{\text{new}}$. Replace Q^2 values of \mathbf{g}_i with the measured values \mathbf{g}_{si} .
 $\mathbf{g}_i \leftarrow \mathbf{g}_i \downarrow \mathbf{g}_{si}$
9. Repeat 2 through 8 until the system settles into an equilibrium state.
10. Form the image by taking every M elements of the column vector of $\hat{\mathbf{f}}$ stacking them one over the other as a row vector.

5.8.3 Simulation results

In this simulation study, four frames of sparse data corresponding to $\kappa = 16$ are generated. In order to test the performance of the cascaded **ANN** model, we have chosen the image given in Fig.1.2b. The algorithm developed in the last section was used for image reconstruction from multiple frames of sparse and noisy data. Figs.5.11a, 5.11b and 5.11c represent the reconstructed images using the method of POCS, the method of TKM-POCS, and the cascaded **ANN** model, respectively. The first row of Fig.5.11 represents the images reconstructed using four frames of noise free data. The image reconstructed (Fig.5.11) using the cascaded **ANN** model is significantly better in quality even though very little knowledge about the object is used as constraints in the reconstruction process. It is noise free and close to the original image.

In order to test the noise suppression property of the proposed model, additive noise (Gaussian noise with zero mean) is added to all the frames of data. The same noise level is added to all the frames of sparse data. Images are reconstructed using the method of POCS, the method of TKM-POCS, and the cascaded **ANN** model. The first, second, and the third column represent, respectively, the images reconstructed using the method of POCS, the method of TKM-POCS and the cascaded **ANN** model from four frames of sparse and noisy data. The results of the simulation study are shown in Figs.5.11d to 5.11l. The second, third, and the fourth row, respectively, represent images reconstructed from four frames of sparse data with noise levels of 0dB, -10dB and -20dB. It is evident from this figure that as the noise level increases in the sparse data, there is a degradation in the quality of the reconstructed images (column- wise). The images in the last column, reconstructed using the cascaded **ANN** model, are

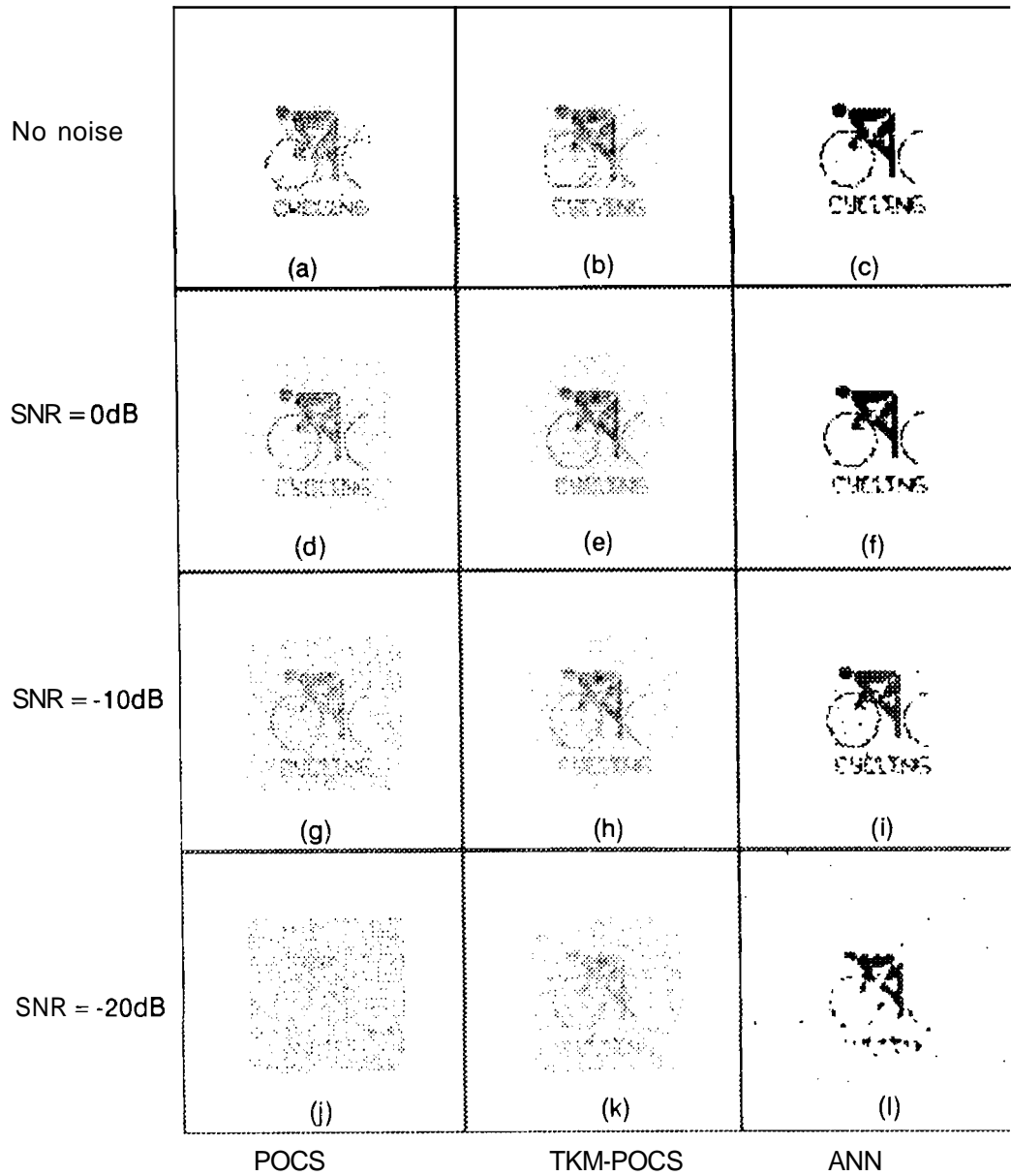


Fig.5.11. Image reconstruction using the cascaded ANN model from multiple frames of sparse data. This figure shows the images reconstructed using the methods of POCS, TKM-POCS and cascaded ANN model. The first row refers images reconstructed using noise free sparse data. The second, third and the fourth rows represent, respectively, the images reconstructed from sparse data ($\kappa = 16$) with noise levels of 0dB, -10dB and -20dB. The first, second and third columns refer to the images reconstructed using the method of POCS, the method of TKM-POCS and the cascaded ANN model, respectively.

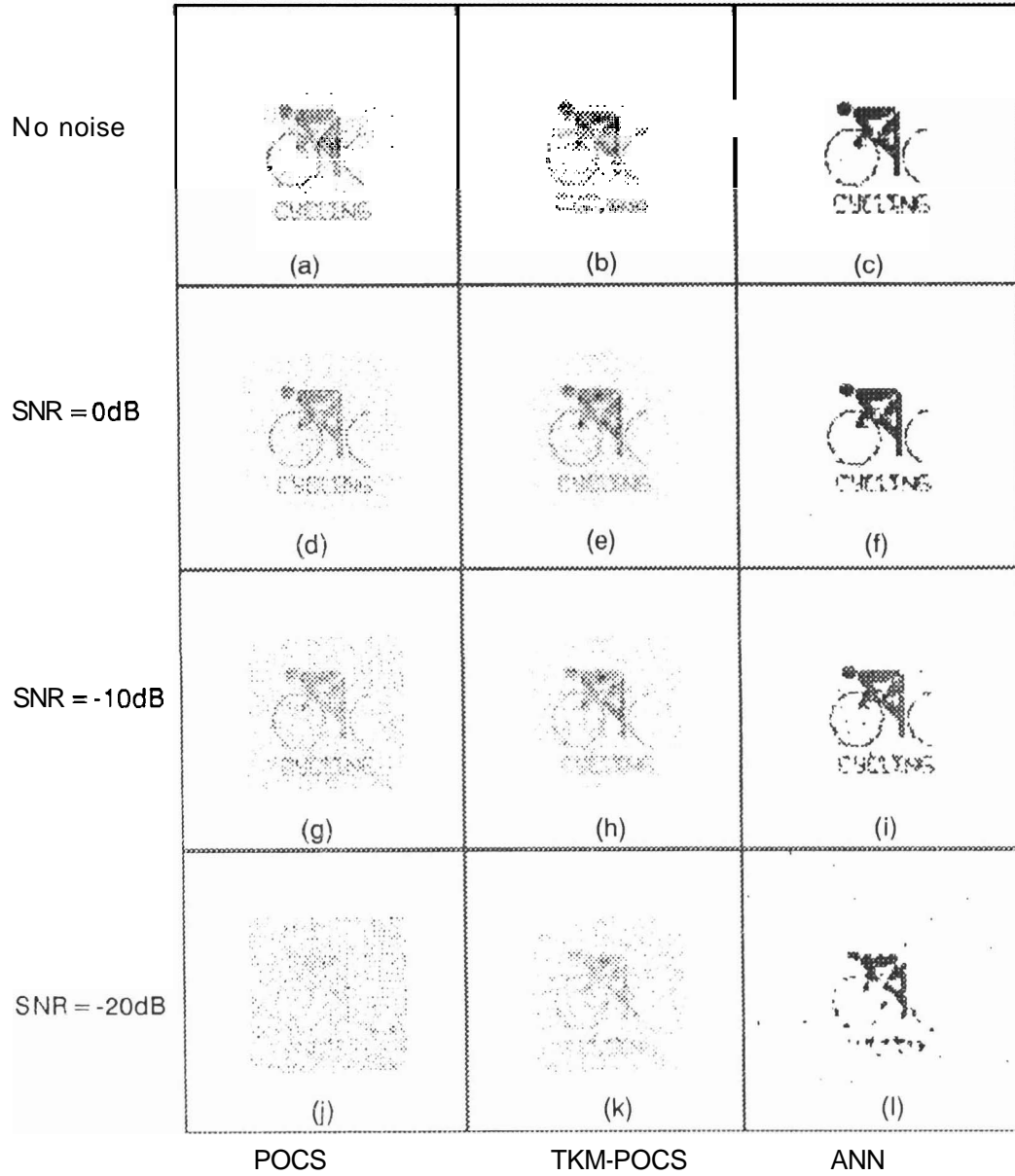


Fig.5.11. image reconstruction using the cascaded ANN model from multiple frames of sparse data. This figure shows the images reconstructed using the methods of POCS, TKM-POCS and cascaded ANN model. The first row refers images reconstructed using noise free sparse data. The second, third and the fourth rows represent, respectively, the images reconstructed from sparse data ($\kappa = 16$) with noise levels of 0dB, -10dB and -20dB. The first, second and third columns refer to the images reconstructed using the method of POCS, the method of TKM-POCS and the cascaded ANN model, respectively.

significantly better in quality even though very little knowledge about the object is used as constraints in the reconstruction process. This shows that the cascaded **ANN** model performs well even when the complexity of the problem increases in terms of noise and the object shape.

5.9 Summary

We have proposed two **ANN** models for image reconstruction from sparse and noisy data. The holographic image formation model helped us to propose an implementation of the bidirectional process of data simulation and image reconstruction. The synaptic weights are directly encoded using the transformation function of the image formation model. The neurons in the data layers represent the hologram, and the neurons in the image layer represent the reconstructed image. Unlike the other methods, these **ANN** models make very little assumptions about the image. The results from these studies show that images with significantly better quality are obtained even when very little knowledge of the constraints about the object is used in the reconstruction process. The edge preserving property of this model is also demonstrated. It is clear from the simulation studies that the proposed **ANN** models handle effectively the difficult situations such as sparsity, noise and complex shapes of objects. A new quality measure based on the method of SVD is suggested.

IMAGE RECONSTRUCTION IN A DYNAMIC SCENE SITUATION

In Chapters 4 and 5, we have considered a static imaging situation to collect multiple frames of sparse data and proposed algorithms to combine them. In many situations, multiple frames of sensor array data may be available as a sequence of frames as in a dynamic scene situation. In this case, each frame of data may contain information about the image but with an unknown motion information superimposed in each frame. In this chapter we propose methods for three situations: (a) known motion parameters, (b) unknown motion parameters, but the object motion restricted to small region in successive frames, and (c) general case of unknown parameters.

6.1 Dynamic scene analysis

Dynamic scene analysis is concerned with the processing of sequence of images. The aim of this analysis is to assimilate information from a sequence as a whole. Most of the literature related to dynamic image analysis deal with the problem of determining the motion of the object from a sequence of images. The motion estimation methods can be classified into four categories: (a) cross-correlation methods, (b) pixel-based methods, (c) feature-based methods, and (d) region-based methods.

The cross-correlation between two images can be used to estimate the motion parameters [Pratt 91]. In this method, shift is associated with the maximum of the correlation function.

In pixel-based methods [Brown 92, Horn 81, Huang 81, Schalkoff 89], the motion parameters for each pixel is estimated based on the assumption that the gray level structure of the image remain the same before and after motion. The motion is estimated based on the relationship between time and spatial differences between two consecutive frames. For each pixel, a displacement vector is found. The field of such vectors constitute the optical flow.

In feature-based methods [Aggarwal 75, Chow 89, Martin 79], correspondence of the extracted features between two consecutive frames is established using rigid body motion constraint to estimate motion parameters.

In region-based methods, central projection of the moving object is used as a feature [Kalivas 91]. Feature extraction is performed by an object boundary estimation algorithm. The motion parameters are estimated by relating an energy function with that of the mismatched region of the consecutive frames. Motion parameters are estimated iteratively by minimizing the area of the mismatched region.

These methods, especially, cross-correlation, pixel-based, and feature-based methods, perform well in the absence of noise. For low SNR images, cross-correlation method is not expected to estimate the motion parameters accurately. Pixel-based methods are very sensitive to noise as they require calculation of derivatives. They assume small motion and

smooth motion. In feature-based methods, noise will affect the extraction of features which in turn affect the establishment of correspondence of features in the consecutive frames.

Region-based methods depend on the segmentation of the object in the image and is shown to perform better than the other methods under noisy situations. It is difficult to segment objects from the images reconstructed from sensor array data and hence this method is also not suited for images reconstructed from sensor array data.

In a SAI setup, only a sequence of frames of sparse data is available. The images in the sequence have to be reconstructed from every frame of sparse data. It has been shown earlier that an image reconstructed from a single frame of sensor array data has a low resolution. Hence from a sequence of noisy and low resolution reconstructed images, it is difficult to estimate motion parameters using any of the known methods.

In a dynamic SAI situation, the aim is to improve the quality of the reconstructed images by combining a sequence of multiple frames of sparse data. In order to combine a sequence of frames, the motion parameters are needed to compensate for motion. In order to estimate motion parameters, high resolution image sequence is required and in order to reconstruct high resolution images, exact motion parameters are required. It is evident from the earlier studies that it is not possible to have either of the requirements satisfied. Therefore we have a dual problem of motion estimation and image reconstruction.

In the next section, we consider a situation where the motion parameters are assumed to be known and propose an algorithm to combine sequence of sensor array data.

6.2 Image reconstruction - known motion parameters

In a dynamic SAI setup one would obtain multiple frames of data naturally when, (i) the object is moving while the sensor array is stationary, (ii) the sensor array is moving while the object is stationary and (iii) both the object and the sensor array are moving.

In our approach, the data is collected for the case of a moving object, while the sensor array remains stationary. We also assume the following: moving object remains within the image, and only one object is moving.

Let $f(x,y)$ be the image, and let $f_i(x,y)$, $i = 1,2,3,..M$, be the spatially shifted versions of $f(x,y)$. Then

$$f_i(x,y) = f(x+\delta x_i, y+\delta y_i), \quad (6.1)$$

where δx_i and δy_i are known shifts of $f(x,y)$ along x and y coordinates, respectively. In this study, we consider an image sequence shown in Fig.6.1 for generating multiple frames of sparse data. Fig.6.1 is used as the reference image. Each image in the sequence is obtained by shifting the image in Fig.6.1a with a known shift value. For each image in the sequence in Fig.6.1, the shift values with respect to the previous frame is given in Table 6.1. Each pair of shift values in the Table 6.1 represents motion parameters.

Table 6.1. Shift values used in the image reconstruction algorithm.

Frame number	Shift with respect to the previous frame
1	(Reference frame) 0,0
2	1,1
3	1,0
4	1,1
5	1,1
6	1,0
7	1,2
8	1,2
9	1,0
10	0,1

When the motion between frames can be compensated exactly, the reconstruction process is same as for the multiple frames of data discussed in Chapters 4 and 5. A sequence of multiple frames are generated for data corresponding to sparse and noisy data ($\kappa = 16$ and $\text{SNR} = -10\text{dB}$) for all the images shown in Fig.6.1. The sequence of multiple frames of data are combined using the method of POCS [Ramaseshan 93] or using the cascaded ANN model discussed in Chapter 5. Here, an image is reconstructed using the first frame of sparse and noisy data. Using the shift values given in Table 6.1, the second image in the sequence is obtained. In order to combine the sparse data of the second frame, the receiver data from the image just obtained is generated, and then the known values of the second frame data replace the calculated values. This in turn is used to reconstruct the image. The process of receiver data generation, shifting, image reconstruction continues until all the frames of data are combined

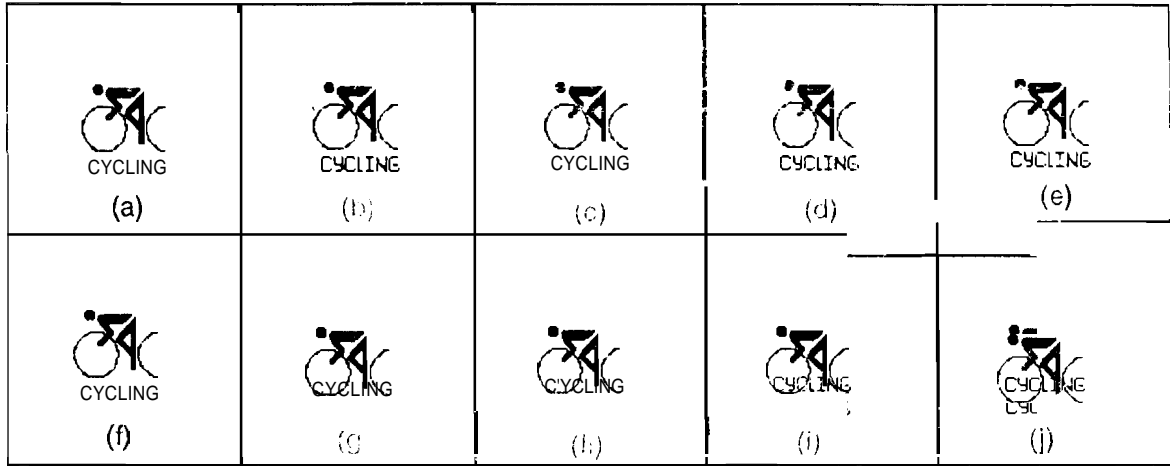


Fig.6.1. Simulated sequence of images (128x128 points) obtained from a dynamic scene situation. Fig.6.1a is used as the reference image. The images in Figs.6.1b-6.1j are obtained using the shift values given in Table 6.1.

and an acceptable image is reconstructed. Algorithms based on the method of POCS, method of TKM-POCS or ANN model can be modified to combine a sequence of multiple frames of sparse and noisy data. We demonstrate that images with improved quality can be obtained using the cascaded ANN model. Fig.6.2 shows the images reconstructed using the cascaded ANN model. Figs.6.2a, 6.2b, 6.2c, and 6.2d represent the images reconstructed

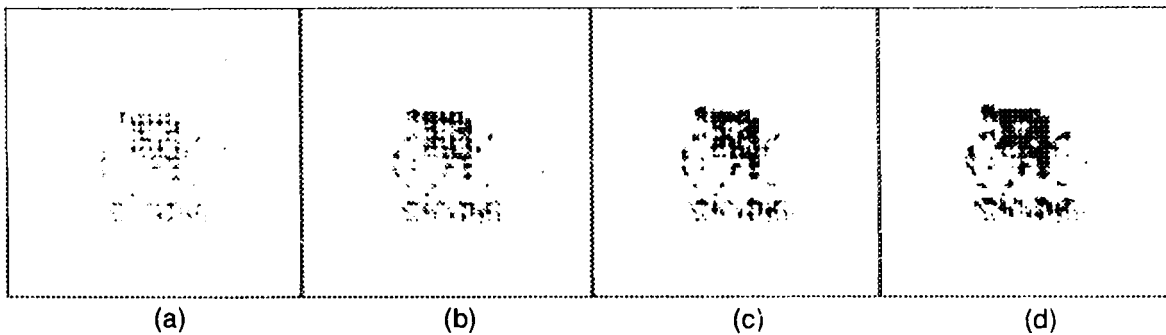


Fig.6.2 Images reconstruction using multiple frames of sparse and data ($\kappa = 16$, $\text{SNR} = -10\text{dB}$) obtained from a simulated dynamic scene situation using the cascaded ANN model. Multiple frames of data are collected for every image shown in Fig.6.1. This figure shows the image reconstructed by combining (a) the first and the second frames of data, (b) the first four frames of data, (c) the first eight frames of data, and (d) all the ten frames of data.

using two, four, eight, and ten frames of sparse and noisy data, respectively. The results show that the quality of the reconstructed image improves as more and more frames of data in the sequence are used for reconstruction.

6.3 Image reconstruction with unknown but restricted motion parameters

In the last section we have combined multiple frames of sparse data obtained from a sequence assuming that the shift information is available *a priori*. A more realistic situation however is one where the motion parameters are not known *a priori*. Since reconstruction from any single frame of sparse data is only a poor quality image, it is difficult to estimate the motion parameters from a sequence of reconstructed images. We now propose a method based on TKM-POCS to reconstruct images with unknown motion parameters but motion restricted to within a region of a few pixels. The reconstruction algorithm given in Section 3.3.4 is used for combining a sequence of ten frames of sparse data. Sequence of multiple frames of data are combined as if the object remained static during the imaging process. In other words motion is not compensated. Figs.6.3a-6.3d

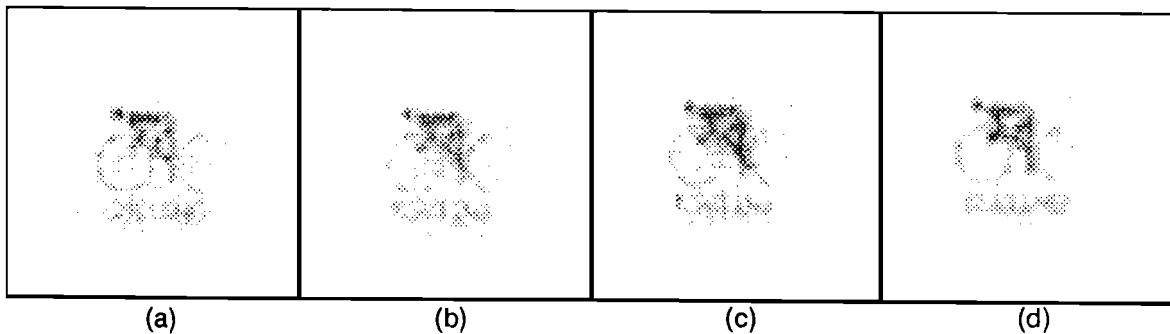


Fig.6.3. Image reconstruction from multiple frames of data with $dx = 0$ and $dy = 0$ for all the frames. Multiple frames of sparse data ($k = 16$) are collected for every image shown in Fig.6.1. Gaussian noise with zero mean is added to every frame of data. The method of TKM-POCS is used for image reconstruction. This figure shows the image reconstructed by combining (a) the first and the second frames of data, (b) the first four frames of data, (c) the first eight frames of data, and (d) all the ten frames of data.

using two, four, eight, and ten frames of sparse and noisy data, respectively. The results show that the quality of the reconstructed image improves as more and more frames of data in the sequence are used for reconstruction.

6.3 Image reconstruction with unknown but restricted motion parameters

In the last section we have combined multiple frames of sparse data obtained from a sequence assuming that the shift information is available *a priori*. A more realistic situation however is one where the motion parameters are not known *a priori*. Since reconstruction from any single frame of sparse data is only a poor quality image, it is difficult to estimate the motion parameters from a sequence of reconstructed images. We now propose a method based on TKM-POCS to reconstruct images with unknown motion parameters but motion restricted to within a region of a few pixels. The reconstruction algorithm given in Section 3.3.4 is used for combining a sequence of ten frames of sparse data. Sequence of multiple frames of data are combined as if the object remained static during the imaging process. In other words motion is not compensated. Figs.6.3a-6.3d

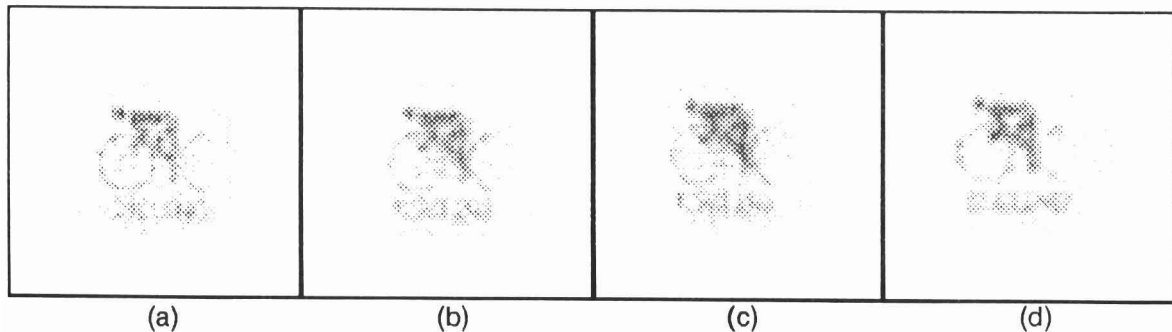


Fig.6.3. Image reconstruction from multiple frames of data with $\delta x = 0$ and $\delta y = 0$ for all the frames. Multiple frames of sparse data ($\kappa = 16$) are collected for every image shown in Fig.6.1. Gaussian noise with zero mean is added to every frame of data. The method of TKM-POCS is used for image reconstruction. This figure shows the image reconstructed by combining (a) the first and the second frames of data, (b) the first four frames of data, (c) the first eight frames of data, and (d) all the ten frames of data.

represent reconstructed images using two, four, eight, and ten frames of sparse and noisy data ($\kappa = 16$ and $\text{SNR} = -10\text{dB}$), respectively. From the images in Fig.6.3, it is clear from this study that images with improved quality can be obtained when the motion between any two consecutive frames is within 1 or 2 pixels. Note in this figure that all the images are blurred.

6.4 Image reconstruction for a general dynamic scene situation

In the last two sections, we have discussed methods to reconstruct images from a sequence of multiple frames of data obtained from a restricted dynamic scene situation. But in a more realistic case, the motion parameters are not known and the motion is not restricted to a few pixels only. The method of TKM-POCS is not useful in such cases. In this section, we consider a general situation where the motion is not restricted, but only translatory motion is considered.

We discuss a method where motion parameters are estimated first from the reconstructed images and later multiple frames of data are combined using the estimated motion parameters. Motion parameters are estimated using the cross-correlation method. It is a similarity measure which gives a measure of similarity between an image and its template.

Given a template f_T and the image f , where f_T is small compared to f . The normalized cross-correlation between two images are given by,

$$C(i,j) = \frac{\sum_x \sum_y f_T(x,y)f(x-i,y-j)}{\sqrt{\sum_x \sum_y f^2(x-i,y-j)}} \quad (6.2)$$

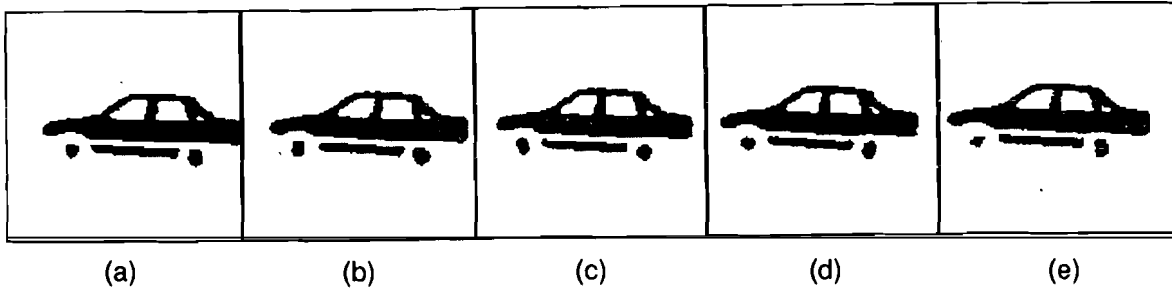


Fig.6.4. Another sequence of images obtained from a dynamic scene situation.

Cross-correlation is calculated for all possible translations. If the template matches exactly a translation $(\delta x, \delta y)$, the cross-correlation will have its peak at $C(\delta x, \delta y)$.

We consider a sequence of images shown in Fig.6.4 for generating sparse data. This shift values between the images are not known. In this image sequence, each image is arbitrarily shifted by a sparse and noisy data ($\kappa = 64$ and $SNR = 0dB$) is generated for each frame. ANN model discussed in Chapter 5 is used to reconstruct images. Shift values are estimated using the cross-correlation method. As each image in the reconstructed image sequence is noisy, the motion estimation is only an approximation of the original one. Using this shift information, multiple frames were combined. Fig.6.5a, 6.5b, 6.5c, 6.5d and 6.5e represent the images reconstructed using one, two, three, four and five frames of sparse

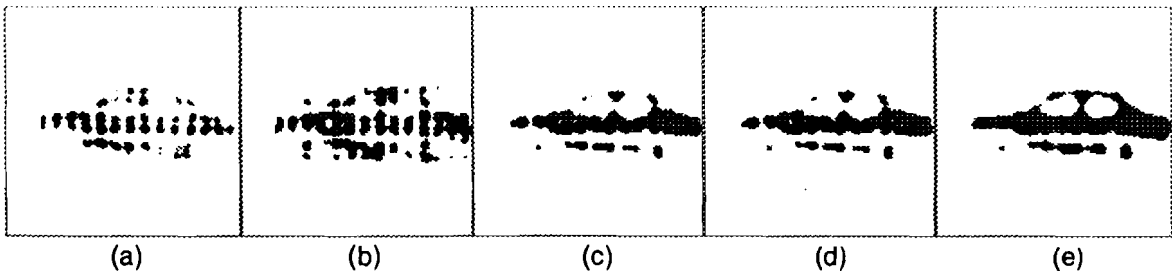


Fig.6.5 Image reconstruction from multiple frames of sparse and noisy data from a dynamic scene situation. ANN model is used for image reconstruction. This figure shows the image reconstructed by combining (a) the first, (b) the first and the second frames of data, (c) the first three frames of data, (d) the first four frames of data, and (e) all the five frames of data.

and noisy data, respectively. As the number of frames included in the reconstruction process is increased, the resolution increases.

This method is suited for situation where there is only a translation of a rigid object. As the complexity of the problem increases in terms of sparsity, noise or complex shape of the object, motion estimation using cross-correlation will be poor. In such cases, some knowledge in the form of constraints on the motion is needed to reconstruct images from sparse and noisy data.

In this chapter, we have proposed methods to combine a sequence of frames of sparse data obtained from a dynamic scene situation. It has been shown that it is possible to reconstruct images with improved quality when a sequence of sparse sensor array data is combined. We have shown that images can be reconstructed when the motion is compensated. We have also shown that the method of TKM-POCS reconstructs images with improved quality where the motion information is not available. A correlation based method was suggested to estimate the motion information for use in the general situation.

SUMMARY AND CONCLUSIONS

In this thesis, we have addressed the problem of image reconstruction from sparse data obtained from SAI situations. The data is sparse and noisy, and hence the quality of the reconstructed images is poor. This is an ill-posed problem, as there is no unique solution. Problems of this kind can be solved using the knowledge about the solution. In this thesis, we have explored the possibility of incorporating knowledge about the object in the reconstruction algorithm and the possibility of combining multiple frames of sparse data obtained from (a) a static situation and (b) a dynamic scene situation. We have proposed methods to reconstruct images from sparse data with acceptable quality for the following cases:

- (i) single frame of data (Chapter 3 and 5)
- (ii) multiple frames of data collected in a static imaging situation
(Chapter 4 and 5)
- (iii) multiple frames of data collected in a dynamic scene situation
(Chapter 6)

7.1 Image reconstruction from single frame of data

We present here the results obtained by incorporating known constraints into the solution to extract maximum information from a single frame of data. Knowledge about the extent of the object (finite support constraint),

knowledge about the intensity of the image (positivity constraint) have been incorporated in the algorithm (ALGORITHM 3.1) to reconstruct an improved quality image. An algorithm (ALGORITHM 3.3) based on the method of TKM-POCS has been developed to include the knowledge about the smoothness of the object together with the knowledge about the extent of the object and the knowledge about the intensity of the image. We have shown in Chapter 3 that incorporation of knowledge about the object using the methods of POCS and TKM-POCS has improved the quality of the reconstructed images. We have also used neural network based classification accuracy as a measure of quality of the reconstructed images.

In many situations, where the type of the object being imaged is unknown. It is also not possible to know the extent of the object in the image or the smoothness of the object. It is shown that images reconstructed using very little knowledge about the object is similar to reconstructing images using inverse filtering. In Chapter 5, we have proposed a method based on an ANN model to handle a situation where only approximate knowledge is available. In this model, knowledge about the smoothness of the object is used only during the initial stages of the network operation. Knowledge about the extent of the object in the image is not used in the reconstruction process. Reconstructed images using the ANN model have been found to be better in quality than the images reconstructed using the methods of POCS and TKM-POCS, even though very little knowledge about the object is used in the reconstruction process.

7.2 Image reconstruction from multiple frames of data - static situation

As the complexity of the problem increases in terms of noise, sparsity, and complex shape of the object, single frame methods fail to provide acceptable results in terms of the quality of the reconstructed image. Moreover, there is no guarantee that the single frame measurements are error-free. In order to handle these situations and improve the quality of the reconstructed image, we have proposed methods to combine multiple frames of sparse data in Chapters 4, 5, and 6.

Algorithms have been developed to combine (a) a set of multiple frames of data obtained from a static situation (Chapters 4 and 5) and (b) a sequence of multiple frames of data obtained from a dynamic scene situation (Chapter 6). In Chapters 4, we have developed algorithms to combine multiple frames of data based on the methods of POCS and TKM-POCS. In Chapter 5, we have proposed a cascaded ANN model to combine multiple frames of data. The quality of the reconstructed images have improved significantly when multiple frames of data are combined. In this situation too, the quality of the images reconstructed using the cascaded ANN model was found to be better.

7.3 Image reconstruction from multiple frames of data dynamic scene situation

When the motion between frames can be compensated exactly, the reconstruction process is same as the one discussed for a static imaging situation. The results show that the quality of the images improved by combining a sequence of multiple frames of data. We have also considered a situation where the motion parameters are unknown but restricted to

within a region of a few pixels. The method of TKM-POCS was used to combine multiple frames of sparse and noisy data. The general case of unknown motion parameter has been discussed and a method to reconstruct images has also been discussed.

In this thesis we have explored the possibility of using the redundancy in the image of an object for reconstruction from sparse data. We have exploited this redundancy using neural network models to reconstruct high resolution images. However, it is a challenging problem to exploit the redundant information across a sequence of frames in a dynamic scene situation without explicitly deriving the motion information. It appears that models based on neural networks may help in overcoming this problem of image reconstruction from a sequence of frames of sparse data in such situations.

APPENDIX

In this Appendix we describe some of the tools used in the image reconstruction, such as lexicographic ordering, block-circulant matrices, and block-Toeplitz matrices.

A.1 Lexicographic ordering

Let $f(i,j)$, ($1 \leq i \leq M$ and $1 \leq j \leq M$) be a 2-D array of pixels representing an image f . This image of size $M \times M$ can be converted into a vector \mathbf{f} of size $M^2 \times 1$ as follows:

$$\mathbf{f} = \begin{bmatrix} f(1,1) \\ f(1,2) \\ f(1,3) \\ \dots \\ \dots \\ \dots \\ f(M,M) \end{bmatrix} \quad (\text{A.1})$$

The ordering of the image f in the vector form as shown in (A.1) is known as lexicographic ordering.

A.2 Block-Toeplitz and block-circulant matrices

If we lexicographically order the matrices $f(i,j)$, $g(i,j)$, and $n(i,j)$ as \mathbf{f} , \mathbf{g} , and \mathbf{n} , then the matrix H in (3.1) will be of size $M \times M$. In order to perform the linear convolution operation, the matrix H would require a block-Toeplitz structure. The matrix H will have M^2 partitions and each partition will be of size $M \times M$. Each partition will have Toeplitz structure.

$$\mathbf{H} = \begin{bmatrix} \mathbf{H}_1 & \mathbf{H}_M & \mathbf{H}_{M-1} & \dots & \mathbf{0} \\ \mathbf{H}_2 & \mathbf{H}_1 & \mathbf{H}_M & \dots & \mathbf{H}_3 \\ \mathbf{H}_3 & \mathbf{H}_2 & \mathbf{H}_1 & \dots & \mathbf{H}_4 \\ \dots & \dots & \dots & \dots & \dots \\ \dots & \dots & \dots & \dots & \dots \\ \mathbf{0} & \mathbf{H}_{M-1} & \mathbf{H}_{M-2} & \dots & \mathbf{H}_1 \end{bmatrix} \quad (\text{A.2})$$

where \mathbf{H}_j

$$\mathbf{H}_j = \begin{bmatrix} h(j,1) & h(j,M) & h(j,M-1) & \dots & 0 \\ h(j,2) & h(j,1) & h(j,M) & \dots & h(j,3) \\ h(j,3) & h(j,2) & h(j,1) & \dots & h(j,4) \\ \dots & \dots & \dots & \dots & \dots \\ \dots & \dots & \dots & \dots & \dots \\ 0 & h(j,M-1) & h(j,M-2) & \dots & h(j,1) \end{bmatrix} \quad (\text{A.3})$$

In order to handle the huge matrix multiplication in (3.1), one has to find a short-cut. A (block-)Toeplitz matrix can be approximately written as a (block-) circulant matrix. These two matrices are closely related in structure. Operations involving (block-)circulant matrices can be evaluated using FT. The block- circulant approximation of (A.2) is given below:

$$\mathbf{H} = \begin{bmatrix} \mathbf{H}_1 & \mathbf{H}_M & \mathbf{H}_{M-1} & \dots & \mathbf{H}_2 \\ \mathbf{H}_2 & \mathbf{H}_1 & \mathbf{H}_M & \dots & \mathbf{H}_3 \\ \mathbf{H}_3 & \mathbf{H}_2 & \mathbf{H}_1 & \dots & \mathbf{H}_4 \\ \dots & \dots & \dots & \dots & \dots \\ \dots & \dots & \dots & \dots & \dots \\ \mathbf{H}_M & \mathbf{H}_{M-1} & \mathbf{H}_{M-2} & \dots & \mathbf{H}_1 \end{bmatrix} \quad (\text{A.4})$$

The circulant approximation of the matrix \mathbf{H}_j is given by:

$$\mathbf{H}_j = \begin{bmatrix} h(j,1) & h(j,M) & h(j,M-1) & \dots & h(j,2) \\ h(j,2) & h(j,1) & h(j,M) & \dots & h(j,3) \\ h(j,3) & h(j,2) & h(j,1) & \dots & h(j,4) \\ \dots & \dots & \dots & \dots & \dots \\ \dots & \dots & \dots & \dots & \dots \\ h(j,M) & h(j,M-1) & h(j,M-2) & \dots & h(j,1) \end{bmatrix} \quad (\text{A.5})$$

The introduction of terms at the end of the diagonal introduces error near the edges of the image. Conversion of (block-)Toeplitz matrix to (block-)circulant matrix makes the convolution a circular one.

REFERENCES

- [Abiss 91] J.B.Abyss, B.J.Brames, and M.A.Fiddy, "Superresolution algorithm for a modified hopfield network," IEEE Trans. SP, vol.39, no.7, pp.1512-1523, 1991.
2. [Aggarwal 75] J.K.Aggarwal and R.O.Duda, "Computer analysis of moving polygonal images," IEEE Trans. Comput., vol.24, pp.966-976, 1975.
 3. [Anderson 76] G.L.Anderson and A.N.Netravali, "Image restoration based on a subjective criterion," IEEE Trans. SMC, vol.6, pp.845-853, 1976.
 4. [Andrews 76] H.Andrews and C.Patterson, "Outer product expansions and their uses in digital image processing," IEEE Trans. Computers, vol.25, pp.140-148, 1976.
 5. [Angel 78] E.S.Angel and A.K.Jain, "Restoration of images degraded by spatially varying point spread function by conjugate gradient method," Applied Optics, vol.17, pp.2186- 2190, 1978.
 6. [Ashjari 82] B.Ashjari, "Singular value decomposition texture measurement for image classification," Ph.D. dissertation, Department of Electrical Engineering, University of California, 1982.
 7. [Siemond 90] J.Biemond, R.Lagendijk, and R.M.Mersereau, "Iterative methods in image deblurring," Proc. of IEEE, vol.78, no.5, pp.856-883, 1990.
 8. [Bertero 88] M.Bertero, T.A.Poggio, and V.Torre, "Ill-posed problems in early vision," Proc. IEEE, vol.76, no.8, pp.917-935, 1988.
 9. [Brown 92] L.G.Brown, "A survey of image registration techniques," ACM Computing Surveys, vol.24, no.4, pp.325-376, 1992.
 10. [Burl 93] J.B.Burl, "A reduced order extended Kalman filter for sequential images containing a moving object," IEEE Trans. IP, vol.2, no.3, 1993.
 11. [Chow 77] W.K.Chow and J.K.Aggarwal, "Computer analysis of planar curvilinear moving images," IEEE Trans. Comput., vol.26, pp.179-185, 1977.
 12. [Combettes 93] P.L.Combettes, "The foundations of set theoretic estimation," Proc. IEEE, vol.81, no.2, pp.182-208, 1993.

13. [Demoment 89] D.Demoment, "Image reconstruction and restoration: overview of common estimation structures and problems," *IEEE Trans. ASSP*, vol.37, no.12, pp.2024-2036, 1989.
14. [Dines 77] K.A.Dines and A.C.Kak, "Constrained least square filtering," *IEEE Trans. ASSP*, vol.25, no.4, pp.346-350, 1977.
15. [Dinten 91] J.M.Dinten, X.Guyon, and J.F.Yao, "On the choice of the regularization parameter: the case of binary images in the Bayesian restoration framework," in *Spatial statistics and imaging*. A.Possolo, ed., California: Institute of Mathematical Statistics, 1991.
16. [Farhat 89] N.H.Farhat and B.Bai, "Echo inversion and target shape estimation by neuromorphic processing," *Neural Networks*, vol.2, pp.117-125, 1989.
17. [Galatsanos 89] N.P.Galatsanos and R.T.Chin, "Digital restoration of multichannel images," *IEEE Trans. ASSP*, vol.37, no.3, 1989.
18. [Galatsanos 91] N.P.Galatsanos and R.T.Chin, "Restoration of color images by multichannel kalman filtering," *IEEE Trans. SP*, vol.39, no.10, pp.2237-2252, 1991.
19. [Galatsanos 92] N.P.Galatsanos and A.K.Katsaggelos, "Methods for choosing the regularisation parameter and estimating the noise variance in image restoration and their relation," *IEEE Trans. IP*, vol.1, no.3, 1992.
20. [Galatsanos 91] N.P.Galatsanos, A.K.Katsaggelos, R.T.Chin, and A.D.Hillery "Least squares restoration of multichannel images" *IEEE Trans. SP*, vol.39, no.10, pp.2222-2236, 1991.
21. [Gerchberg 75] R.Gerchberg, "Super-resolution through error energy reduction," *Optica acta*, vol.21, pp.709-720, 1975.
22. [Giordano 85] A.A.Giordano and F.M.Hsu, *Least squares estimation with applications to digital signal processing*, New York: John-Wiley and Sons, 1985.
23. [Gonzalez 87] R.C.Gonzalez and P.Wintz, *Digital Image Processing*, Reading: Addison-Wesley, 1987.
24. [Goutsias 87] J.I.Goutsias and J.M.Mendel, "Inverse problems in two-dimensional acoustic media: a linear imaging model," *JASA*, vol.81, no.5, 1987.
25. [Grossberg 88] S.Grossberg, "Nonlinear neural networks principles, mechanisms and architectures," *Neural Networks*, vol.1, no.1, pp.17-81, 1988.
26. [Horn 81] B.K.P.Horn and B.G.Schunck, "Determining optical flow," *Artificial Intelligence*, vol.17, pp.506-624, 1981.

27. [Huang 81] T.S.Huang, Image sequence analysis, Berlin: Springer-Verlag, 1981.
28. [Huang 75a] T.S.Huang, D.A.Barker, and S.P.Berger, "Iterative image restoration," Applied Optics, vol.14, no.9, pp.1165-1168, 1975a.
29. [Huang 75b] T.S.Huang and P.M.Narendra, "Image restoration by singular value decomposition," Applied Optics, vol.14, no.9, pp.2213-2216, 1975b.
30. [Hunt 73] B.R.Hunt, "The application of constrained least squares estimation to image restoration by digital computers," IEEE Trans. ASSP, vol.22, no.9, pp.805- 812, 1973.
31. [Hunt 84] B.R.Hunt and O.Kubler, "Karhunen-Loeve multispectral image restoration, Part-I: theory," IEEE Trans. ASSP, vol.32, no.3, pp.592-599, 1984.
32. [Hurlbert 88] A.C.Hurlbert and T.A.Poggio, "Synthesizing a color algorithm from examples," Science, vol.239, pp.482-489, 1988.
33. [Hurlbert 92] A.C.Hurlbert, "Neural network approaches to color vision," in Neural Networks for Perception, vol.1, pp.265- 283, H.Wechsler, ed., San Diego: Academic, 1992.
34. [Irani 91] M.Irani and S.Peleg, "Improving resolution by image registration," CVGIP: Graphical Models and Image Processing, vol.53, no.3, pp.231-239, 1991.
35. [Kalivas 91] D.S.Kalivas and A.A.Sawchuk, "A region matching motion estimation algorithm", CVGIP: Image Understanding, vol.54, no.2, pp.275-288, 1991.
36. [Karayiannis 90] N.B.Karayiannis and A.N.Venetsanaopoulos, "Regularization theory in image restoration - the stabilizing functional approach," IEEE Trans. ASSP, vol.38, no.7, pp.1155- 1178, 1990.
37. [Katsaggelos 87] A.K.Katsaggelos, "Multiple input adaptive iterative image restoration algorithms," Proc. ICASSP, pp.1179-1182, 1987.
38. [Katsaggelos 88] A.K.Katsaggelos and J.K.Paik, "Iterative color restoration algorithms," Proc. ICASSP, pp.1028- 1031, 1988.
39. [Katsaggelos 90] A.K.Katsaggelos and S.N.Efstratiadis, "A class of iterative signal restoration algorithms," IEEE Trans. ASSP, vol.38, no.5, pp.778-786, 1990.
40. [Katsaggelos 91] A.K.Katsaggelos, J.Biémont, R.W.Schafer, and R.M. Mersereau, "A regularized iterative image restoration algorithm," IEEE Trans. SP, vol.39, no.4, pp.914-929, 1991.

41. [Kawata 80a] S.Kawata and Y.Ichioka, "Iterative image restoration for linearly degraded images. I-Basis," *JOSA*, vol.70, no.7, pp.762-768, 1980.
42. [Kawata 80b] S.Kawata and Y.Ichioka, "Iterative image restoration for linearly degraded images. I.Reblurring Procedure," *JOSA*, vol.70, no.7, pp.768-772, 1980.
43. [Kay 91] J.W.Kay, "A comparison of smoothing parameters choices in image restoration," in *Spatial statistics and imaging*, A.Possolo, ed., California: Institute of Mathematical statistics, 1991.
44. [Keating 79] P.N.Keating, T.Sawatari, and G.Zilinskas, "Signal processing in acoustic imaging," *Proc. IEEE*, vol.67, no.4, pp.496-525, 1979.
45. [Kim 90] S.P.Kim, S.K.Bose, and H.M.Valenzuela, "Recursive reconstruction of high resolution image from noisy undersampled multiframe," *IEEE Trans. ASSP*, vol.38, no.6, 1990.
46. [Kosko 87] B.Kosko, "Adaptive bidirectional associative memories," *Applied Optics*, vol.26, no.23, 1987.
47. [Kosko 90] B.Kosko, "Unsupervised learning in noise," *IEEE Trans. Neural Networks*, vol.1, no.1, 1990.
48. [Kosko 92] B.Kosko, *Neural Networks and Fuzzy Systems*, New Jersey: Prentice Hall, 1992.
49. [Kulkarni 91] A.D.Kulkarni, "Solving ill-posed problems with artificial neural networks," *Neural Networks*, vol.4, pp.477-484, 1991.
50. [Kung 92] S.Y.Kung, *Digital neural networks*, New Jersey: Prentice Hall, 1992.
51. [Lagendijk 88] R.L.Lagendijk, J.Biemon, and J.E.Boeke, "Regularized iterative image restoration with ringing reduction," *IEEE Trans. ASSP*, vol.36, no.12, pp.1874-1888, 1988.
52. [Lagendijk 91] R.L.Lagendijk and J.Biemon, *Iterative Identification and Restoration of Images*. Boston: Kluwer Academic, 1991.
53. [Lippmann 87] R.P.Lippmann, "An introduction to computing with artificial neural networks," *IEEE ASSP Magazine*, vol.2, pp.4-22, 1987.
54. [Mariadassou 90] C.P.Mariadassou, "Solutions to some ill- posed problems in sensor array imaging," *Ph.D Dissertation*, Dept. of Computer Science and Engineering, Indian Institute of Technology, Madras, 1990.
55. [Marroquin 87] J.Marroquin, S.Mitter, and T.Poggio, "Probabilistic solution of ill-posed problems in computational vision," *J. Amer. Stat. Assoc.*, vol.82, no.397, pp.76-89, 1987.

56. [Martin 79] W.N.Martin and J.K.Aggarwal, "Computer analysis of dynamic scenes containing curvilinear figures," *Pattern recognition*, vol.2, pp.169-178, 1979.
57. [Miller 70] K.M.Miller, "Least squares methods for ill-posed problems with a prescribed bound," *SIAM J. Math. Anal.*, vol.1, no.1, pp.52-74, 1970.
58. [Nashed 81] M.Z.Nashed, "Operator theoretic and computational approaches to ill-posed problems with application to antenna theory," *IEEE Trans. Antennas Prop.*, vol.29, no.2, pp.220-231, 1981.
59. [Ozkan 92] M.K.Ozkan, A.T.Erdem, M.I.Sezan, and A.M.Tekalp, "Efficient multiframe wiener restoration of blurred and noisy image sequences," *IEEE Trans. IP*, vol.1, no.4, pp.453-476, 1992.
60. [Paik 92] J.K.Paik and A.K.Katsaggelos, "Image Restoration using a Modified Hopfield Network," *IEEE Trans. IP*, vol.1, no.1, pp. 49-63, Jan. 1992.
61. [Phillips 62] D.L.Phillips, "A Technique for the numerical solution of certain integral equations of the first kind by inversion of the linear system produced by quadrature," *JACM*, vol.9, pp.84-97, 1962.
62. [Podilchuk 90] C.I.Podilchuk and R.J.Mammone, "Image recovery by convex projections using a least-squares constraint," *JOSA*, vol.7, no.3, pp.517-521, 1990.
63. [Poggio 90] T.Poggio, and F.Girosi, "Networks for approximation and learning," *Proc. IEEE*, vol.78, no.9, pp.1481-1497, 1990.
64. [Pratt 91] W.K.Pratt, *Digital Image Processing*, New York: John Wiley, 1991.
65. [Press 92] W.H.Press, S.A.Teuklosky, W.T.Vetterling, and B.P.Flannery, *Numerical recipes in C the art of scientific computing*, Cambridge University Press, 1992.
66. [Ramaseshan 93] R.Ramaseshan, and B.Yegnanarayana, "Image reconstruction from multiple frames of sparse data," *Multidimensional Systems and Signal Processing*, vol.4, no.2, pp.167-179, 1993.
67. [Reeves 90] S.J.Reeves and R.M.Mersereau, "Optimal estimation of the regularisation parameters and stabilizing functional for the regularized image restoration," *Opt. Engg.*, vol.29, pp.446-454, 1990.
68. [Sarkar 81] T.K.Sarkar, D.D.Weiner, and V.K.Jain, "Some mathematical considerations in dealing with inverse problems," *IEEE Trans. Antennas Prop.*, vol.29, no.2, pp.373-379, 1981.

69. [Schaffer 81] R.W.Schaffer, R.M.Mersereau, and M.A.Richards, "Constrained iterative restoration algorithms," Proc. IEEE, vol.69, no.4, pp.432-450, 1981.
70. [Schalkoff 89] R.J.Schalkoff, Digital image processing, New York: Wiley, 1989.
71. [Sezan 87] M.I.Sezan and H.Stark, Image recovery: theory and application, H.Stark, ed., Orlando: Academic, 1987.
72. [Sezan 89] M.I.Sezan and H.J.Russel, "Use of a priori knowledge in multispectral image restoration," Proc. ICASSP, pp.1429-1432, 1983.
73. [Sezan 90] M.I.Sezan, and A.M.Tekalp, "Adaptive image restoration with artifact suppression using the theory of convex projections," *IEEE Trans. ASSP*, vol.38, no.1, 1990.
74. [Shim 81] Y.S.Shim and Z.H.Cho, "SVD pseudoinversion image reconstruction," *IEEE Trans. ASSP*, vol.29, no.4, 1981.
75. [Sutton 79] J.L.Sutton, "Underwater acoustic imaging," Proc. IEEE, vol.67, no.4, pp.554-565, 1979.
76. [Tekalp 91] A.M.Tekalp and H.J.Trussel, "Comparative study of some statistical and set-theoretic methods for image restoration," *CVGIP: Graphical Models and Image Processing*, vol.53, no.2, pp.108-120, 1991.
77. [Toet 89] A.Toet, L.J.van Ruyven, and J.M.Valeton "Merging thermal and visual images by a contrast pyramid," *Optical Engineering*, vol.28, no.7, 1989.
78. [Tikhonov 77] A.N.Tikhonov and V.Y.Arsenin, Solutions to Ill-posed Problems, New York: John Wiley, 1977.
79. [Tikhonov 87] A.N.Tikhonov and A.V.Goncharsky, Applications of Ill-posed problems in Natural Sciences, Moscow: Mir, 1987.
80. [Titterington 91] D.M.Titterington, "Choosing the regularization parameter in image reconstruction," in *Spatial statistics and imaging*, A.Possolo, ed., California: Institute of Mathematical statistics, 1991.
81. [Tom 81] V.T.Tom, T.F.Quartieri, M.H.Hayes, and J.H.McClellan, "Convergence of iterative nonexpansive signal reconstruction algorithms," *IEEE Trans. ASSP*, vol.29, pp.1052-1058, 1981.
82. [Trussel 83a] H.J.Trussel, "Convergence criteria for iterative restoration methods," *IEEE Trans. ASSP*, vol.31, pp.129-136, 1983.
83. [Trussel 83b] H.J.Trussel and M.R.Civanlar, "The initial estimate in constrained iterative restoration," Proc. ICASSP, pp.643-646, 1983.

84. [Trussel 84] H.J.Trussel, and M.R.Civanlar, "The feasible solution in signal restoration," IEEE Trans. ASSP, vol.32, pp.201-212, 1984.
85. [Twomey 63] S.Twomey, "On the numerical solution of Fredholm integral equations of the first kind by inversion of linear systems produced by quadrature," JACM, vol.10, pp.97-101, 1963.
86. [Wahl 87] F.M.Wahl, Digital Image Signal Processing, Boston: Artech House, 1987.
87. [Wolberg 90] G.Wolberg, Digital Image Warping, Los Alamitos: IEEE Computer Society, 1993.
88. [Yegnanarayana 89] B.Yegnanarayana, R.Ramaseshan, and A.Ravichandran, "Image reconstruction from multiple frames of data," in Indo-US workshop: Spectrum Analysis in One and Two Dimensions, pp. 367-382, 1989.
89. [Yegnanarayana 90a] B.Yegnanarayana, C.P.Mariadassou, and P.Saini, "Signal reconstruction from partial data for sensor array imaging applications," Signal Processing, vol.19, no.2, 1990a.
90. [Yegnanarayana 90b] B.Yegnanarayana, R.Ramaseshan, and A.Ravichandran, "An algorithm for thinning noisy images," Proc. ICASSP, pp.2217-2220, 1990b.
91. [Yegnanarayana 91] B.Yegnanarayana, R.Ramaseshan, and A.Ravichandran, "Improving resolution of sensor array using multiple frames of data," in 19th International symposium: Acoustical Imaging, 1991.
92. [Yegnanarayana 93] B.Yegnanarayana and R.Ramaseshan, "An artificial neural network model for image reconstruction from multiple frames of noisy sparse data," in Indo-US workshop: Parallel and distributed Signal and Image Integration, 1993.
93. [Youla 82] D.C.Youla and H.Webb, "Image restoration by the method of convex projections: part 1 - theory," IEEE Trans. Medical Imaging, vol.1, no.2, pp.81-94, 1982.
94. [Youla 87] D.C.Youla, "Mathematical theory of image restoration by the method of convex projections", in Image Recovery: Theory and Application, H.Stark, ed., Orlando: Academic, 1987.
95. [Zhou 88] Y.T.Zhou, Rama Chellappa, A.Vaid, and B.K.Jenkins, "Image restoration using neural networks," IEEE Trans. ASSP, vol.36, no.7, pp.1141-1151, 1988.

LIST OF PUBLICATIONS

In Journal:

1. R. Ramaseshan and B. Yegnanarayana, "Image reconstruction from multiple frames of sparse data," *Multidimensional Systems and Signal Processing*, vol. 4, no. 2, pp.167-179, 1993.

In Conferences:

1. B.Yegnanarayana and R. Ramaseshan, "An artificial neural network model for image reconstruction from multiple frames of noisy sparse data," in *Indo-US workshop: Parallel and distributed signal and image integration*, 1993.
2. B.Yegnanarayana, R.Ramaseshan, and A. Ravichandran, "Improving resolution of sensor array using multiple frames of data," in *19th International symposium: acoustical imaging*, 1991.
3. B.Yegnanarayana. R.Ramaseshan, and A.Ravichandran, "An algorithm for thinning noisy images," *Proc. ICASSP*, pp.2217-2220, 1990.
4. B.Yegnanarayana, R.Ramaseshan, and A. Ravichandran, "Image reconstruction from multiple frames of data," in *Indo-US workshop on Spectrum analysis in one and two dimensions*, pp. 367-382, 1989.

In Technical Reports:

1. B.Yegnanarayana. R.Ramaseshan, and A.Ravichandran, Studies in sensor array imaging, Speech and vision lab., Indian Institute of Technology, Madras, 1991.
2. B.Yegnanarayana. R.Ramaseshan, and A.Ravichandran, "An algorithm for image reconstruction from dynamic scene situation," Technical report, no.11, Speech and vision lab., Indian Institute of Technology, Madras, 1991.
3. B.Yegnanarayana. R.Ramaseshan, and A.Ravichandran, "Image reconstruction from multiple frames of data obtained from a sensor array imaging setup," Technical report, no.8, Speech and vision lab., Indian Institute of Technology, Madras, 1990.

4. B.Yegnanarayana. R.Ramaseshan, and A.Ravichandran, "Implementation of image reconstruction algorithms using parallel and distributed processing models," Technical report, no.10, .Speech and vision lab., Indian Institute of Technology, Madras, 1990.